UNIVERSITY OF CALIFORNIA SAN DIEGO

Fundamental Understanding and Atomic-Scale Design of Novel Catalysts for Efficient Electrochemical Reactions

A dissertation submitted in partial satisfaction of the
requirements for the degree Doctor of Philosophy

in

Chemical Engineering

by

Qiaowan Chang

Committee in Charge:

Professor Zheng Chen, Chair
Professor David Fenning
Professor Ping Liu
Professor Zhaowei Liu
Professor Wei Xiong

2021

The dissertation of Qiaowan Chang is approved, and it is acceptable in quality and form for publication on microfilm and electronically.

University of California San Diego

2021

DEDICATION

This dissertation is dedicated to my supervisors, friends, husband and parents.

EPIGRAPH

Patience is a virtue.

-Piers Plowman, 1360

TABLE OF CONTENTS

LIST OF FIGURES

LIST OF TABLES

ACKNOWLEDGEMENTS

Above all, I would like to express my deep sense of gratitude to my advisor, Professor Zheng Chen. I am grateful for his continuous and generous support for my any interested idea and project, even for the seemly infeasible one that requiring plenty of time to learn the totally new and different technique only due to my own interest. I am deeply impressed with his patience and valuable guidance, helping me through my writing and entire research. I appreciate his any suggestions and plans for my better future and career. I'm also grateful for the help and support from other collaborate advisors: Prof. Jingguang Chen and Prof. Choi Sang-Il. Prof. Jingguang Chen always provides any guidance and help when I need. I'm truly grateful for any instructions and opportunities from him. In addition, I sincerely acknowledge the committee members: Professor Ping Liu, Professor David Fenning, Professor Wei Xiong, and Professor Zhaowei Liu, for their valuable time, encouragement and suggestions.

Secondly, I would like to thank my labmates, Mingyu Yu, Pu Zhang, Mingqian Li, Hongpeng Gao, Panpan Xu and Guorui Cai, for the happiness and meaningful time with them during the PhD study. I acknowledge the contribution of other group members in the Columbic University and Brookhaven National Laboratory (BNL) for their invaluable help throughout the projects: Dr. Shyam Kattel, Dr. Ji Hoon Lee, Dr. Zhixiu Liang, and Dr. Liang Song. In addition, I'm also grateful for all the help about administrative issues from Ms. Dana Jimenez.

Finally, I would like to express my special thanks to my husband and parents, for their forever support and love.

Chapter 2.2, in full, is a reprint of the material “Enhancing C-C Bond Scission for Efficient Ethanol Oxidation using PtIr Nanocube Electrocatalysts” as it appears in ACS Catalysis, Qiaowan Chang, Shyam Kattel, Xing Li, Zhixiu Liang, Brian M. Tackett, Steven R. Denny, Pu Zhang, Dong Su, Jingguang G. Chen, Zheng Chen, 2019, 9, 7618-7625. The dissertation author was the first author of this paper and conducted all the essential research work.

Chapter 2.3, in part is currently being prepared for submission for publication of the material. Qiaowan Chang, Youngmin Hong, Hye Jin Lee, Zhixiu Liang, Ji Hoon Lee, Ji-Eun Lim, Liang Song, Shyam Kattel, Jingguang G Chen, Zheng Chen, Sang-Il Choi. Single atomic Rh decorated Pt nanocubes promoting complete electrooxidation of ethanol. The dissertation author was the primary investigator and author of this material.

Chapter 3.2, in full, is a reprint of the material “Promoting H2O2 Production via 2-Electron Oxygen Reduction by Coordinating Partially Oxidized Pd with Defect Carbon” as it appears in Nature Communications, Qiaowan Chang, Pu Zhang, Amir Hassan Bagherzadeh Mostaghimi, Xueru Zhao, Steven R. Denny, Ji Hoon Lee, Hongpeng Gao, Ying Zhang, Huolin Xin, Samira Siahrostami, Jingguang G. Chen, Zheng Chen, 2020, 11, 2178-2187. The dissertation author was the first author of this paper and conducted all the essential research work.

Chapter 4.2, in full, is a reprint of the material "Boosting Activity and Selectivity of CO_2 Electroreduction by Pre-hydridizing Pd Nanocubes" as it appears in Small, Qiaowan Chang, Jeonghyeon Kim, Ji Hoon Lee, Shyam Kattel, Jingguang G. Chen, Sang-Il Choi, Zheng Chen, 2020, 16, 2005305. The dissertation author was the first author of this paper and conducted all the essential research work.

I would like to acknowledge the financial support from the ACS Petroleum Research Fund and Jacob School of Engineering at UC San Diego.

VITA

2014	B.S., Chemical Engineering, Tianjin University, Tianjin, China
2016	M.Ph., Chemical Engineering, Hong Kong University of Science and Technology, Clear Water Bay, Hong Kong
2021	Ph.D., Chemical Engineering, University of California San Diego, La Jolla, CA

PUBLICATIONS

1. Wu, S. H., Wu, J. L., Jia, S. Y., **Chang, Q. W.**, Ren, H. T., & Liu, Y., 2013. Cobalt (II) phthalocyanine-sensitized hollow Fe_3O_4@ SiO_2@ TiO_2 hierarchical nanostructures: Fabrication and enhanced photocatalytic properties. Applied Surface Science, 287, pp. 389-396.

2. Hachimi, A., Merzougui, B., Hakeem, A., Laoui, T., Swain, G.M., **Chang, Q. W.**, Shao, M. H. and Atieh, M.A., 2015, Synthesis of nitrogen-doped carbon nanotubes using injection-vertical chemical vapor deposition: effects of synthesis parameters on the nitrogen content. Journal of Nanomaterials, 2015, p.453725

3. Akinpelu, A., Merzougui, B., Bukola, S., Azad, A.M., Basheer, R.A., Swain, G.M., **Chang, Q. W.** and Shao, M. H., 2015. A Pt-free electrocatalyst based on pyrolized vinazene-carbon composite for oxygen reduction reaction. Electrochimica Acta, 161, pp.305-311.

4. Shao, M. H., **Chang, Q. W.**, Dodelet, J.P. and Chenitz, R., 2016. Recent advances in electrocatalysts for oxygen reduction reaction. Chemical Reviews, 116(6), pp.3594-3657.

5. Zhang, L. L., Zhu, S. Q., **Chang, Q. W.**, Su, D., Yue, J., Du, Z. and Shao, M. H., 2016. Palladium–platinum core–shell electrocatalysts for oxygen reduction reaction prepared with the assistance of citric acid. ACS Catalysis, 6(6), pp.3428-3432.

6. Chen, H. M., Xing, Z. L., Zhu, S. Q., Zhang, L. L., **Chang, Q. W.**, Huang, J., Cai, W.B., Kang, N., Zhong, C.J. and Shao, M. H., 2016. Palladium modified gold nanoparticles as electrocatalysts for ethanol electrooxidation. Journal of Power Sources, 321, pp.264-269.

7. Zhang, L. L., **Chang, Q. W.**, Chen, H. M. and Shao, M. H., 2016. Recent advances in palladium-based electrocatalysts for fuel cell reactions and hydrogen evolution reaction. Nano Energy, 29, pp.198-219.

8. **Chang, Q. W.**, Xiao, F., Xu, Y. and Shao, M. H., 2017. Core-Shell Electrocatalysts for Oxygen Reduction Reaction. Acta Physico-Chimica Sinica, 33(1), pp.9-17.

9. **Chang, Q. W.**, Xu, Y., Duan, Z., Xiao, F., Fu, F., Hong, Y., Kim, J., Choi, S.I., Su, D. and Shao, M. H., 2017. Structural Evolution of Sub-10 nm Octahedral Platinum–Nickel Bimetallic Nanocrystals. Nano Letters, 17(6), pp.3926-3931.

10. Sulaiman, J. E., Zhu, S. Q., Xing, Z. L., **Chang, Q. W.** and Shao, M. H., 2017. Pt–Ni octahedra as electrocatalysts for the ethanol electro-oxidation reaction. ACS Catalysis, 7(8), pp.5134-5141.

11. **Chang, Q. W.**, Xu, Y., Zhu, S. Q., Xiao, F. and Shao, M. H., 2017. Pt-Ni nanourchins as electrocatalysts for oxygen reduction reaction. Frontiers in Energy, 11(3), pp.254-259.

12. **Chang, Q. W.**, Kattel, S., Li, X., Liang, Z., Tackett, B.M., Denny, S.R., Zhang, P., Su, D., Chen, J.G. and Chen, Z., 2019. Enhancing C–C Bond Scission for Efficient Ethanol Oxidation using PtIr Nanocube Electrocatalysts. ACS Catalysis, 9(9), pp.7618-7625.

13. Xiao, F., Qin, X., Xu, M., Zhu, S. Q., Zhang, L. L., Hong, Y., Choi, S.I., **Chang, Q. W.**, Xu, Y., Pan, X. and Shao, M. H., 2019. Impact of Heat Treatment on the Electrochemical Properties of Carbon-Supported Octahedral Pt–Ni Nanoparticles. ACS Catalysis, 9(12), pp.11189-11198.

14. **Chang, Q. W.**, Zhang, P., Mostaghimi, A.H.B., Zhao, X., Denny, S.R., Lee, J.H., Gao, H., Zhang, Y., Xin, H.L., Siahrostami, S. and Chen, J.G., 2020. Promoting H_2O_2 production via 2-electron oxygen reduction by coordinating partially oxidized Pd with defect carbon. Nature communications, 11(1), pp.2178-2187.

15. **Chang, Q. W**., Kim, J., Lee, J. H., Kattel, S., Chen, J.G., Choi, S.I. and Chen, Z., 2020. Boosting Activity and Selectivity of CO_2 Electroreduction by Pre-Hydridizing Pd Nanocubes. Small, 16(49), p.2005305.

16. **Chang, Q. W.**, Hong, Y., Lee, H. J., Liang, Z. X., Lee, J. H., Lim J., Song L., Kattel S., Chen, J.G., Chen, Z., Choi, S.I., 2021. Single atomic Rh decorated Pt nanocubes promoting complete electrooxidation of ethanol. In preparation.

ABSTRACT OF THE DISSERTATION

Fundamental Understanding and Atomic-Scale Design of Novel Catalysts for Efficient Electrochemical Reactions

by

Qiaowan Chang

Doctor of Philosophy in Chemical Engineering

University of California San Diego, 2021

Professor Zheng Chen, Chair

The availability of renewable energy sources (solar and wind) provides opportunities to replace many traditional chemical reactions by the electrochemical processes to achieve industrial upgrading, including direct ethanol fuel cells (DEFCs), hydrogen peroxide (H_2O_2) production, and carbon dioxide (CO_2) conversion. However, the rates of many important reactions involved in electrochemical processes are too slow

and the selectivity of targeted products also needs to be improved. The key to solve these challenges is to design better electrocatalysts.

In this thesis, some strategies to design advanced electrocatalysts are investigated. The first strategy is to control the morphology and surface composition of the Platinum (Pt) nanocube-based electrocatalyst in DEFCs to selectively cleave the C-C bond in ethanol to improve its energy utilization. The (100)-exposed $Pt_{38}Ir$ nanocubes with one-atom-thick Ir-rich skin exhibited unprecedented EOR activity, high CO_2 selectivity and long-term stability, due to the promotion of C-C bond cleavage and CO desorption from the catalyst surface. Furthermore, we show that the complete oxidization of ethanol to CO_2 was achieved by the Rh single atom on the Pt(100) surface, demonstrating the great potential of the decoration of single atom catalysts on the metallic surface in electrochemical reactions.

The second example is to tune the local chemical coordination between atomic catalyst clusters (metal) and their support materials (defect carbons) using a composite approach to achieve the synergistic effect in H_2O_2 electrochemical production. A catalyst composed of oxidized carbon nanotubes and clusters of three to four partially oxidized palladium (Pd) atoms was prepared, forming a special coordination (Pd-O-C) between carbon material and partially oxidized Pd atoms. This coordination can significantly enhance its H_2O_2 production rate with > 90% selectivity and shorten the production time.

The third strategy is to control the intermediate state of catalyst to promote CO_2 reduction. In previous studies, Pd was found to transform into palladium hydride (PdH) during the reaction and the latter was believed to be beneficial for syngas production. Based on this finding, the electrocatalyst was directly designed to partially hydridize Pd nanocubes. In comparison with pure metallic Pd, partial hydridization of Pd structure ($PdH_{0.40}$) showed an earlier transformation to the key intermediate, leading to enhanced syngas production. As a result, the suitable operation potential range can be extended, resulting in a more flexible working condition for potential industrial applications.

Overall, the above three strategies for designing electrocatalysts are explored in this thesis work. The results will provide fundamental understanding and guidance for rational design of highly efficient electrocatalysts for crucial electrochemical reactions, getting one step closer to the industrial applications related to sustainable and green chemical engineering.

Chapter 1. Introduction

1.1. Background

Current world is on the brink of energy crisis, an escalation energy demands on the limited natural resources (fossil fuels), owing to the global population swelling and industrialization on the rise in developing nations.[1] The Department of Economic and Social Affairs in United Nations projected that the world's population would be increased by 2 billion persons in the next 30 years.[2] And the International Energy Agency reported that energy demand was projected to grow by 12% between 2019 and 2030.[3] Besides, excessive burning of fossil fuels is also resulting in a steady increase of carbon dioxide emissions, leading to the global warming and ocean acidification. The energy crisis highlights the need to study a holistic and innovative approach of green chemical engineering to sustainable development.

The holistic green chemical engineering approach to reduce energy crisis includes the industrial upgrading from the source, process and the end treatment. Specifically, the current fossil fuel can be transited to renewable energy sources, such as wind, solar, water, bioenergy and nuclear. Another promising candidate is fuel cells, converting the chemical energy in hydrogen or liquid fuels (methanol, ethanol) and oxygen into electrical energy. The energy saving, emission reduction and quality improvement process of chemical production is a necessary to reduce energy crisis. For example, today's industrial energy-intensive and pollution-extensive H_2O_2 production method can be replaced by a green and

user-friendly electrochemical H_2O_2 synthesis only involving hydrogen and oxygen. The capture, utilization and storage of CO_2 at the end will effectively decrease atmospheric CO_2 level. Electrochemical technology based on CO_2 reduction reaction could reutilize and convert CO_2 to other important chemicals to mitigate the climate change and ocean acidification.

In short, electrochemical technology can play a key role in escalating the current chemical engineering to prevent and solve energy crisis. The development of electrocatalyst is a "bottleneck" to wider applications of electrochemical technology including fuel cells, H_2O_2 electrochemical synthesis, CO_2 electrochemical reduction, etc.

1.2. Electrocatalysts: performance assessment and design

The electrocatalysts performance is evaluated from activity, selectivity, durability. The activity of electrocatalysts can be represented by the onset potential, overpotential, peak potential, current density, etc. The onset potential is the lowest (for the anodic reactions) or the highest (for the cathodic reactions) potentials at which the reaction occurs in the experimental conditions.[4] The experimental thermodynamic overpotential is the difference between equilibrium potential and onset potential. The peak potential is the potential at which the highest current density in the reaction. Usually, the less overpotential or the less difference between equilibrium potential and peak potential, the better thermodynamics presented for the electrocatalysts. The current density can be

compared by the highest current density during the reaction or current density at a specified potential/through designated calculations. The current densities of electrocatalysts need to be normalized by its electrochemical surface area (ECSA) or mass when comparing with benchmark or other catalysts.

In most of electrochemical reactions, different reaction products will be generated. The selectivity can be described by the ratio of the amount (or faradic efficiency) of targeted product to all the products. The stability is an important parameter for electrocatalysts, since any commercial electrocatalysts must maintain stable during the operation.[5] The stability can be reported by the activity and selectivity changes after cyclic voltammetry (CV) cycling or chronoamperometry (CA) at a specified potential of the working electrode. The cost of the electrocatalysts cannot bet neglected for the further commercial application of electrochemical systems.

Various kinds of electrocatalysts have been designed to enhance its catalytic performance and decrease its production cost during the past decades, including noble metal-based alloys, shape-controlled alloys, core-shell nanostructures, single atom catalysts, metal nitrides/carbides, etc. By alloying noble metal with transition metals, the d-band center and metal-metal distances will be modified to tune the adsorption of intermediates on catalyst's surface. The catalytic performance of electrocatalysts also depends on its exposed surface due to the different binding energies of intermediates on it. For example, the activity of oxygen reduction reaction in a weakly adsorbed electrolyte

follows the order of Pt(100) ≪ Pt(111)≈Pt(110).[6] Since only surface atoms expose to the electrolyte and participate in the electrochemical reactions, core-shell nanostructures (depositing a thin noble-metal shell on the less expensive core) and single atom catalysts are proposed to improve the utilization of noble metal atoms and decrease the commercial cost of electrocatalysts.

1.3. Grand challenges in electrocatalysts development

Despite great effort to enhance the electrochemical performance of electrocatalyst, it's still a long way to achieve the industrial electrochemical applications. The current catalytic performance of catalysts is undesired. For example, the fuel utilization of ethanol in direct ethanol fuel cells is only 5-10% due to the low selectivity toward CO_2;[7] the activity and cost of the electrocatalyst in H_2O_2 electrochemical production needs to be improved, given the best electrocatalyst (Pt-Hg alloys) studied previously;[8] more studies needs to be focused on the preferred product distribution and the corresponding current density in CO_2 reduction reaction for forwarding the actual application of CO_2 electrochemical reutilization.

1.4. Motivation and Outline of the Thesis

As discussed above, the key to solve the energy crisis is to design effective and efficient electrocatalyst. This thesis explores novel strategies to design electrocatalysts at

atomic scale through fundamental understanding of their elementary processes in several key reactions. The aim is to achieve enhanced efficiency, selectivity and stability with minimum byproducts. Different catalyst design strategies will be demonstrated using important reaction processes including direct liquid fuel cells, de-centralized hydrogen peroxide (H_2O_2) production, and carbon dioxide (CO_2) conversion.

Chapter 2 discusses the morphology control and composition optimization strategy for the electrocatalysts design in ethanol oxidation reaction in direct liquid fuel cells. **Chapter 3** shows the composite approach to tune the local chemical coordination between atomic catalyst clusters and their support materials to achieve synergic effect in two-electron oxygen reduction reaction for de-centralized H_2O_2 production. **Chapter 4** explores strategy to artificially control the intermediate state of catalyst to promote CO_2 reduction to syngas.

Chapter 2. Ethanol oxidation reaction

Direct liquid fuel cells (DLFCs) are attracting growing attention as portable power sources for transportation due to their advantages over gaseous hydrogen fuel cells (HFCs) such as lower infrastructure and operation cost and higher mass-energy density.[9-10] Ethanol is of particular interest as a liquid fuel since it can be produced at low cost and in large scale from agriculture feedstocks, making it a green and sustainable fuel.[9, 11] In addition, ethanol is safer and offers higher energy density than methanol (8.3 vs. 6.1 kWh/kg), the state-of-the-art liquid fuel for DLFCs.[9, 11]

2.1. Introduction

2.1.1. Reaction mechanisms

The anode reaction in DFECs is ethanol oxidation reaction, in which ethanol is oxidized by oxygen to generate water and CO_2 as the complete oxidization product via 12-electron transfer. Due to the difficulty in breaking C-C bond in ethanol, it is more easily to be partially oxidized to acetaldehyde (CH_3CHO) and acetic acid (CH_3COOH) via 2 and 4-eletron transfer, respectively.

Lai et al.[12] showed that ethanol adsorption site on the electrocatalysts determines the reaction pathways. The production of CH_3CHO and CH_3COOH is preferred when the ethanol's hydroxyl (-OH) site is adsorbed on the catalyst surface and undergoes the

cleavage of O-H bond. For forming CO_2, the C_1 or $C_{2\pi}$ adsorption sites are needed to generate π bond activation intermediate on the catalyst to assist C-C bond cleavage.

2.1.2. Literature review of electrocatalysts

Platinum-based materials represent the most effective electrocatalysts for the electrochemical ethanol oxidation reaction (EOR).[13-16] However, common carbon-supported platinum (Pt/C) catalysts often possess limited active sites for C-C bond cleavage and are easily poisoned by strongly adsorbed C_1 intermediates, (*e.g.*, *CO, *CH_3, * denotes an adsorption site on the catalyst surface).[17-18] Creating bimetallic Pt-M (M=Ru, Sn, Ni, *etc*.) electrocatalysts can improve the mass activity compared with pure Pt due to the introduction of oxygen-containing groups (M-OH or M-O), which promotes the removal of *CO from the active Pt sites and leads to enhanced EOR activity.[13, 19-21] Unfortunately, ethanol often undergoes partial oxidation to form acetic acid (CH_3COOH) through a 4-electron (e^-) reaction instead of forming CO_2 (12 e^-) as the complete oxidization product [22-24], possibly due to an increased energy barrier for C-C bond cleavage when the surface is covered by adsorbed hydroxide (*OH).[25-26] As a result, fuel utilization efficiency for such Pt-M/C catalysts is generally very low (3%-20%),[22, 27-28] which hinders the commercialization of direct ethanol fuel cell (DEFC).

Surface engineering represents an effective strategy to tune the EOR selectivity. Density functional theory (DFT) calculations show that the Pt(100) facet presents the

lowest activation barrier for C-C bond breaking (0.65 eV) compared with Pt(111) (1.36 eV), and the bond cleavage occurs through strongly chemisorbed precursors, such as CH_2CO or CHCO, only at low-coordinated surface sites.[29] Moreover, alloying Pt with Ir or Rh can facilitate the C-C bond splitting by moderating the intermediate adsorption through changing the Pt coordination environment.[30-35] Using *in-situ* infrared reflection absorption spectroscopy (IRRAS), Adzic *et al* demonstrated that the $PtIr_x/SnO_2/C$ catalyst with high Ir loading (x=1) shows a reduced onset potential of CO_2 generation (0.5 V vs. 0.55 V for Pt/C versus reversible hydrogen electrode or RHE) and improved CO_2 selectivity.[30] With pinhole on-line electrochemical mass spectrometry, Rao *et al* identified that the EOR selectivity of Pt_1Ir_3/C toward CO_2 is much higher than that of the Pt_3Ir_1/C electrocatalyst due to higher Ir loading.[34] Similar bimetallic effect has been observed on PtRh electrocatalysts that the CO_2 selectivity can be significantly improved compared with Pt/C.[36-37] . Strasser *et al.*[32] investigated the suitable Rh content in PtNiRh octahedra for enhancing CO_2 selectivity in the alkaline electrolyte, revealing that the lower the Rh content in the PtNiRh octahedra, the higher CO_2 selectivity. So far the best EOR electrocatalysts can achieve the 12-e^- reaction in the narrow potential range close to the onset potential, but their CO_2 selectivity at high potential and the mass activity remain low.[30, 33] In addition, the even higher cost of Ir and Rh (2 and 3 times that of Pt, respectively)[38] will prevent the widespread adoption of electrocatalysts with high Ir or Rh loadings.

Table 2.1 Summary of the representative reports ECSA-normalized activity and selectivity toward CO_2 at Pt-Ir and Pt-Rh alloys for the EOR.

Electrocatalysts	Specific activity (mA cm^{-2})	CO_2 onset potential (vs. RHE)	CO_2 selectivity at 0.75 V vs. RHE	Measured method	Ref.
$PtIrSnO_2/C$	1.0[a]	0.55	17%	*in situ* FTIR	[30]
$PtIr_{1/2}SnO_2/C$	0.75[a]	0.45	6%[b]	*in situ* FTIR	[30]
$PtIr_{1/4}SnO_2/C$	0.8[a]	0.52	4%[b]	*in situ* FTIR	[30]
Pt_3Ir/C	-	-	11.4%[c]	DEMS	[34]
$PtIr_3/C$	-	-	12.1%[c]	DEMS	[34]
$Pt_1Rh_{0.8}/C$	0.14[d]	0.65	-	*in situ* FTIR	[39]
$Pt_1Rh_{0.58}(SnO_2)_{0.35}/C$	0.11[d]	0.55	1-fold enhanced CO_2 current density	*in situ* FTIR	[39]
$Pt\text{-}Rh\text{-}SnO_2/C$	15[e]	0.36	-	*in situ* FTIR	[36]
$Pt_{39}Pd_{33}Rh_{28}/C$	0.38[f]	0.35[g]	-	*in situ* FTIR	[40]
$Pt_{37}Rh_{20}\text{-}O_{21}\text{-}(SnO_2)_{43}/C$	0.3[d]	-	17%[h]	CO_2 micro-electrode	[41]
$Pt_{28}Rh_{72}/C$	0.008[i]	0.55	-	*in situ* FTIR	[42]
Pt_9Rh_1 cube/graphene	1.3	0.2 vs. Ag/AgCl	-	*in situ* FTIR	[43]
$Pt_{65}Rh_{10}/SnO_2/C$	1.6[j]	-	10%	HPLC	[44]

[a] based on mass specific activity; [b] measured at 0.8 V vs. RHE; [c] measured at 0.7 V vs. RHE;[d] based on mass activity; [e] Electrocatalysts contain 30 nmol Pt, 8 nmol Rh and 60 nmol SiO_2; [f] scan rate of 1 mV/s; [g] 0.35V vs. NHE; [h] measured at 0.35V vs Ag/AgCl; [i] scan rate of 5 mV/s; [j] 1M C_2H_5OH+0.1M $HClO_4$ with scan rate of 20 mV/s

2.2. Atom-Thick Ir-rich Skin on PtIr Nanocube

2.2.1. Experimental

2.2.1.1. Electrocatalysts synthesis

Pt nanocubes (NCs) were prepared by a solution method. In a typical synthesis, 20 mg of $Pt(acac)_2$ (Chem-Impex, 98%) was dissolved in a mixed solution containing 7 ml of benzyl ether (Sigma-Aldrich, 98%), 1 ml of oleic acid (Sigma-Aldrich, 90%), and 2 ml of oleylamine (Sigma-Aldrich, 70%). The solution was heated to 130 °C under Ar protection and then $W(CO)_6$ (Sigma-Aldrich, 97%) was added during the heating process. Pt NCs were obtained after heating the solution to 235 °C for 40 min. Then the resulted colloidal products were centrifuged and washed using 5 ml of toluene and 10 ml of ethanol. After centrifugation, the Pt NCs were mixed with 12 mg of Ketjen black (C) and then dispersed in 10 ml of toluene for 3 h by ultrasonication. After dispersion, the Pt NCs/C were collected and dried at 60 °C for 3 h. PtIr NCs/C were prepared in the same way with adding $Ir(acac)_3$ (Sigma-Aldrich, 97%) into the precursor solution. For PtIr NCs/C, 10 and 20 mg of $Ir(acac)_3$ was used for the synthesis of $Pt_{38}Ir$ NCs/C and $Pt_{17}Ir$ NCs/C, respectively. For the preparation of $Pt_{12}Ir$ NCs/C, 12 mg of $Pt(acac)_2$ and 18 mg of $Ir(acac)_3$ were used.

2.2.1.2. Characterization

The size and morphology of the NC samples were characterized by transmission electron microscopy (TEM, JEOL JEM2100F). High-angle annular dark-field scanning TEM (HAADF-STEM) images were acquired by Hitachi HD 2700C and energy

dispersive X-ray spectroscopy (EDS) analyses were performed using a FEI Talos F200X. X-ray diffraction (XRD) patterns were obtained by an X-ray diffractometer equipped with a Cu Kα radiation source (λ=1.5406 Å) at 40 kV and 20 mA (Bruker AXS). The bulk compositions of PtIr alloys were determined by inductively coupled plasma mass spectrometry (ICP-Mass, iCAP Qc, Thermo Fisher Scientific). PtIr NCs/C were dissolved by a mixture of HF and HNO_3 (volume ratio of 3:1). The solution was heated to 90 °C for 72 h. After cooling down to room temperature, the solution was mixed with HF and HNO_3 (volume ratio of 3:1) again and heated to 60 °C for 24h. The surface composition of PtIr NCs was determined by a commercial SPECS Ambient-pressure X-ray photoelectron spectrum (AP-XPS) chamber equipped with a PHOIBOS 150 EP MCD-9 analyzer and the result was checked by repeating XPS test for 3 times. Equation 2.1, adapted from reference,[45] was used for XPS analysis. The equation describes the XPS signal intensity ratio for a thin overlayer of one material on top of an infinitely thick substrate.

$$\frac{I_A/S_A}{I_B/S_B} = \frac{1 - \exp\left[-\frac{d}{\lambda^A_{IMFP}(E_A)\cos\theta}\right]}{\exp\left[-\frac{d}{\lambda^A_{IMFP}(E_B)\cos\theta}\right]} \quad \textbf{(Eq. 2.1)}$$

In the equation, *A* refers to the overlayer material (Ir), and *B* refers to the substrate material (Pt). *I* is XPS signal intensity, quantified by peak areas. *S* is atomic sensitivity factor. λ is inelastic mean free path of a photoelectron traveling through the overlayer

material with energy, E. Due to the similarity in Pt *4f* and Ir *4f* electron binding energies, a single value of λ = 1.684 nm was used in both the numerator and denominator. θ is the photoemission angle relative to the surface normal, considered to be zero for these calculations. d is the thickness of the overlayer.

2.2.1.3. Electrochemical measurements

A three-electrode system was used in electrochemical measurements, where a Pt wire and Ag/AgCl (3M Cl^-) were used as the counter and reference electrode, respectively. All the potentials were calibrated to a reversible hydrogen electrode (RHE). For the ink preparation, 2.5 mg of Pt/C or PtIr/C electrocatalysts were homogenously dispersed in a mixture solution containing 2.0 ml of Milli-Q water, 0.5 ml of isopropanol and 10 µl of Nafion (5%). 10 µl of each catalyst ink was deposited on a pre-cleaned glassy carbon (GC) electrode. In the CV measurement, electrocatalysts were first cleaned in Ar-saturated 0.1 M $HClO_4$ solution with a scanning rate of 100 mV s^{-1} in the voltage range of 0.05~1.20 V (vs. RHE) for 20 cycles. Then stabilized CV curves were obtained with a scanning rate of 50 mV s^{-1}. For EOR measurements, CV curves were recorded in Ar-saturated 0.1 M $HClO_4$ solution containing 0.2 M of C_2H_5OH with a scanning rate of 50 mV s^{-1}. CA curves in terms of steady-state activity for EOR were measured at 0.45 V vs. RHE. Stability test was performed by holding potential at 0.45 V vs. RHE for every 10000 s followed by CV cleaning using a scanning rate of 100 mV s^{-1} in the voltage range of 0.05~1.20 V (vs. RHE)

for 20 cycles. During the stability test, 3 cycles of 10000 s was examined. In CO stripping experiments, the potential of pre-cleaned electrode was held at 0.05 V for 10 min in a CO-saturated 0.1 M $HClO_4$ solution for CO adsorption. After purging Ar for 30 min to clear excess CO in the cell, CO stripping curves were taken with a scanning rate of 50 mV s^{-1}.

2.2.1.4. In-situ infrared reflection-absorption spectroscopy (IRRAS)

Nicolet IS50 spectrometer equipped with a mercuric cadmium telluride (MCT) detector was used in IRRAS measurements. The homemade electrochemical cell is consisted of a ZnSe hemisphere window and three electrodes, including an Au working electrode, a Ag/AgCl reference electrode and a Pt mesh counter electrode.[46] To avoid possible signal interference, the chamber was purged with compressed air (CO_2 and H_2O-free) to remove water moisture and CO_2 before collecting FTIR spectra. To get the product distribution during CV measurement, spectra were recorded from 0.05 to 1.05 V (vs. RHE) by every 0.1 V. The resolution was 4 cm^{-1} and 127 interferograms were together added to each spectrum. The final FTIR spectra were acquired by subtracting the first spectrum as the reference. Table 2.2 shows the FTIR peak assignments. To obtain the exact generation time of CO_2, spectra was collected by holding the potential at 0.45 V vs. RHE for 600 s. The electrolytes in this experiment were 0.1 M $HClO_4$ solution containing 0.2 M of C_2H_5OH.

Table 2.2 In-s*itu* FTIR spectra bands assignments[18, 47-50].

Wave number(cm^{-1})	Mode
2341	CO_2 asymmetric stretching in solution
2041	Absorbed CO linearly bonded
1715	C=O stretching in CH_3CHO and CH_3COOH in solution
~1635	H-O-H bending of H_2O
1620-1635	C=O stretching of absorbed acetaldehyde and acetyl
1550	O-C-O asymmetric stretching of acetate in solution
1438	CH_3 bending in acetic acid
1415	O-C-O symmetric stretching of acetate
1355/1368	CH_3 symmetric deformation in CH_3CHO
~1350	Bicarbonate anions signals/O-C-O symmetric stretching
~1348/1383	CH in-plane bending mode of absorbed acetate/acetate in solution
1280	C-O stretching in CH_3COOH
1274	Associated to an intermediate $CH_3CH(OH)O$-Pt to acetate
1257	The C-O stretch of a species containing a COH group, indicating Pt_2-CH_3CHO
1108	C-H wagging in CH_3CHO
1044	C-O stretching of CH_3CH_2OH
933	C-C-O asymmetric stretching of CH_3CHO

2.2.1.5. DFT calculations

DFT calculations were performed using Vienna Ab-Initio Simulation Package (VASP) code. [51-52] Projector augmented wave potentials were used to describe the core electrons with the generalized gradient approximation (GGA), using PW91 functionals.[53] The Kohn-Sham one-electron wave functions were expanded by using a plane wave basis set with a kinetic energy cutoff of 400 eV. The Brillouin zone was sampled using a 3 × 3 × 1 k-point grid in the Monkhorst-Pack scheme.[54]

The Pt(100) surface was modeled using a four layer 3 × 3 surface slab. The Ir_4Pt_5(100) surface was modeled by replacing four of the surface Pt atoms with Ir atoms, and Ir-ML-Pt(100) surface was obtained by replacing all surface Pt with Ir. A 14 Å thick vacuum was added along the direction perpendicular to the surface in the initial slab model to avoid the artificial interactions between the slab and its periodic images. During geometry optimization, the atoms in the bottom two layers were fixed while all other atoms including adsorbates were allowed to relax until Hellman-Feynman force on each ion was smaller than 0.02 eV/Å. The binding energy (*B.E.*) of an adsorbate is calculated as:

$$B.E. = E(\text{slab+adsorbate}) - E(\text{slab}) - E(\text{adsorbate})$$

where *E*(slab+adsorbate), *E*(slab) and *E*(adsorbate) are total energies of optimized slab+adsorbate, slab and adsorbate configurations, respectively.

2.2.2. Results and discussions

Both the Pt and PtIr alloy core-shell NCs display uniform cubic morphology with an average particle size of ~10 nm (**Figure 2.1, 2.2 and 2.3**). The PtIr NCs show preferential exposure of the (100) facets (**Figure 2.2 and 2.3**). ICP-MS results show that PtIr alloy NCs with different overall compositions (e.g., $Pt_{38}Ir$, $Pt_{17}Ir$) can be obtained using different amounts of $Ir(acac)_3$ (10 and 20 mg, respectively) in the precursor solution. The lattice distance of preferentially exposed facets for individual $Pt_{38}Ir$ and $Pt_{17}Ir$ NCs

are ~2.04 Å and ~2.05 Å, respectively, which is close to the interplanar distance of (100) planes of pure Pt. This suggests that the growth of PtIr alloy NCs follows the structural orientation of predominant (100) facets.[55] High-resolution transmission electron microscopic imaging and energy dispersive X-ray spectrometry mapping (**Figure 2.4A-L**) clearly reveal the desired core-shell structures with distinct element distributions through individual NCs. As shown in **Figure 2.4D and I**, the $Pt_{38}Ir$ alloy NCs are composed of uniform Pt-rich cores and Ir-rich shells with a thickness of ~0.2 nm (corresponding to one atomic layer, **Figure 2.4J**). Similar core-shell structures with Pt-rich cores and Ir-rich shells are also observed for $Pt_{17}Ir$ NCs (**Figure 2.4H and K**), with the thickness of the Ir-rich shell on $Pt_{17}Ir$ NCs being increased to 0.4 nm (corresponding to two atomic layers, **Figure 2.4L**). These structure characteristics of PtIr alloy NCs suggest that in the solution reaction Pt^{2+} is reduced first and faster, while Ir^{3+} reduction occurs after the formation of a Pt core.

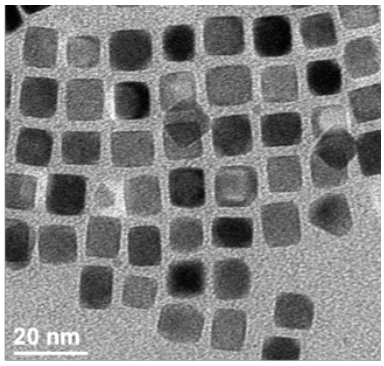

Figure 2.1 Low-magnification TEM image of as-synthesized Pt NCs.

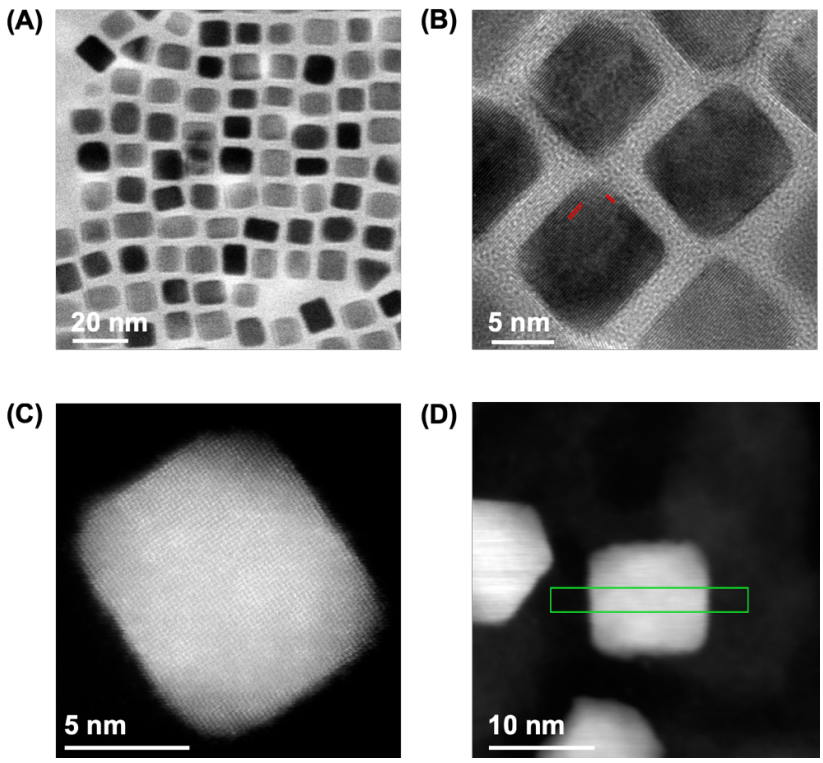

Figure 2.2 Low-magnification TEM image (A), HRTEM image (B) of as-obtained $Pt_{38}Ir$ NCs. Atomic resolution HAADF-STEM image along the <100> zone axis (C) and ADF-STEM image (D) of a single $Pt_{38}Ir$ NC. The highlighted area (green region in D) corresponds to the detailed EDS cross-sectional element mapping shown in Figure 2.4I of a single $Pt_{38}Ir$ NC.

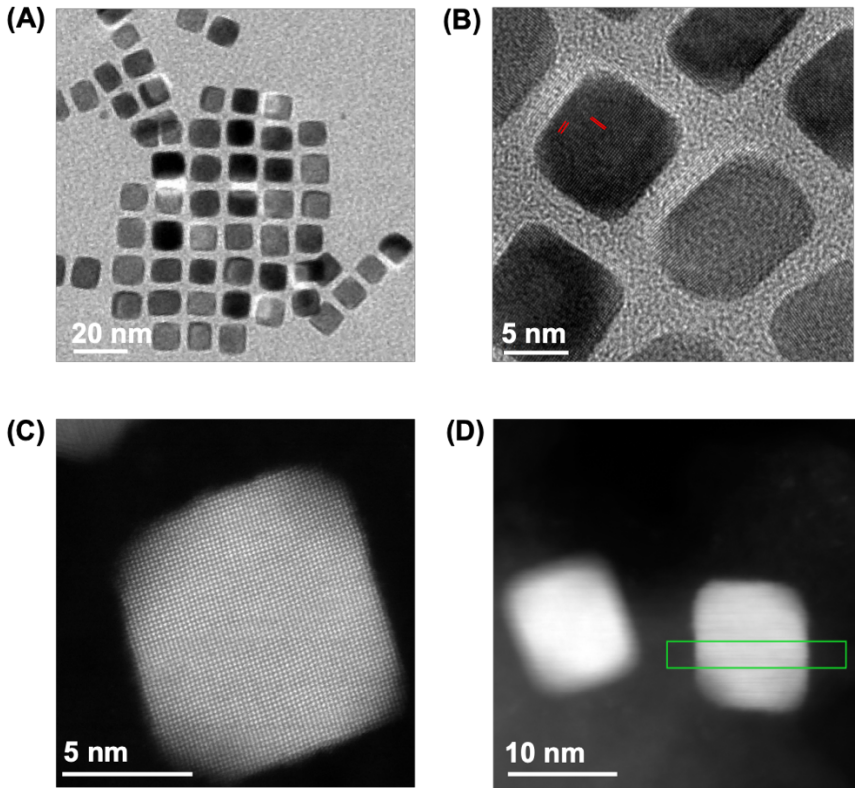

Figure 2.3 Low-magnification TEM image (A), HRTEM image (B) of as-obtained $Pt_{17}Ir$ NCs. Atomic resolution HAADF-STEM image along the <100> zone axis (C) and ADF-STEM image (D) of a single $Pt_{17}Ir$ NC. The highlighted area (green region in D) corresponds to the detailed EDS cross-sectional element mapping shown in Figure 2.4K of a single $Pt_{17}Ir$ NC.

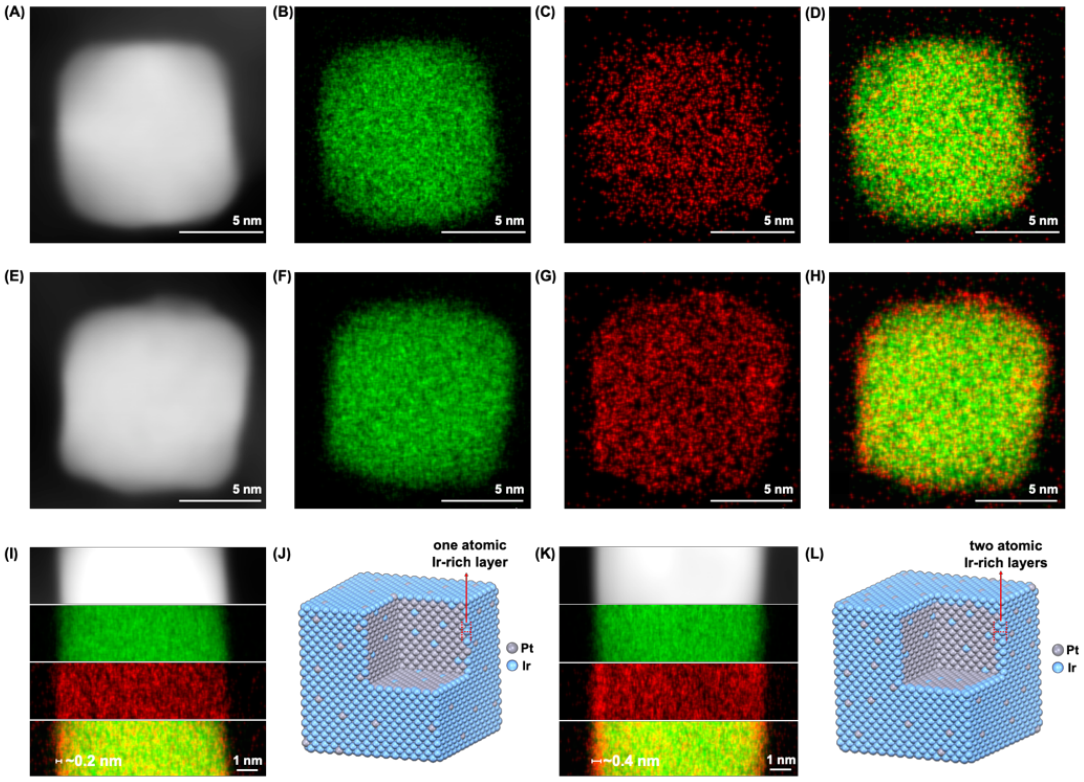

Figure 2.4 Structure and composition characterization of PtIr alloy core-shell NCs. ADF- STEM image (A) and EDS element mapping (B, C, D) of a representative single $Pt_{38}Ir$ NC present the distribution of Pt (green) and Ir (red). ADF-STEM image (E) and EDS element mapping (F, G, H) of a representative single $Pt_{17}Ir$ NC. EDS cross-sectional element mapping (I) of a single $Pt_{38}Ir$ NC (Figure 2.2) clearly show it Pt-rich core and Ir-rich shell structure with the shell thickness of ~0.2 nm. (J) A schematic 3D representation of a $Pt_{38}Ir$ core-shell NC with an ultrathin Ir-rich shell corresponding to the thickness of only one atomic layer of Ir-rich skin. EDS cross-sectional element mapping (K) of a single $Pt_{17}Ir$ NC (Figure 2.3) clearly show it Pt-rich core and Ir-rich shell structure with the shell thickness of ~0.4 nm. (L) A schematic 3D representation of a $Pt_{17}Ir$ core-shell NC with an ultrathin Ir-rich shell corresponding to the thickness of two atomic layer of Ir-rich skin.

The surface compositions of the PtIr alloy core-shell NCs were characterized by XPS. The Ir 4f peaks are nearly negligible for $Pt_{38}Ir$ samples synthesized at 170 and 200 °C (**Figure 2.5A**) and become visible only after the formation of the core-shell structure at

235 ℃ (**Figure 2.5B**), consistent with the surface enrichment of Ir. The Pt 4f peak is a characteristic of metallic Pt (Pt^0). The Pt and Ir peak positions remain the same in the $Pt_{38}Ir$ and $Pt_{17}Ir$ bimetallic catalysts, indicating that the oxidation state of Pt and Ir remains the same in all the samples. Furthermore, by assuming an atomic layer of Ir on an infinitely thick Pt substrate and using an atomic thickness of Ir at 0.225 nm and an inelastic mean free path (IMFP) value of 1.684 nm for the Ir and Pt 4f features, the XPS ratio of Ir/Pt is calculated to be 0.143, very close the experimental value of 0.15 for the $Pt_{38}Ir$ sample. **Figure 2.5C** also reveals that the XPS Ir/Pt ratio further increases for the $Pt_{17}Ir$ core-shell structure due to the higher surface concentration of Ir. Powder XRD patterns (**Figure 2.6**) of $Pt_{38}Ir$ and $Pt_{17}Ir$ NCs/C show nearly identical features to that of Pt(100) NCs, with the same peak positions to commercial Pt/C, further suggesting the formation of core-shell PtIr NCs.

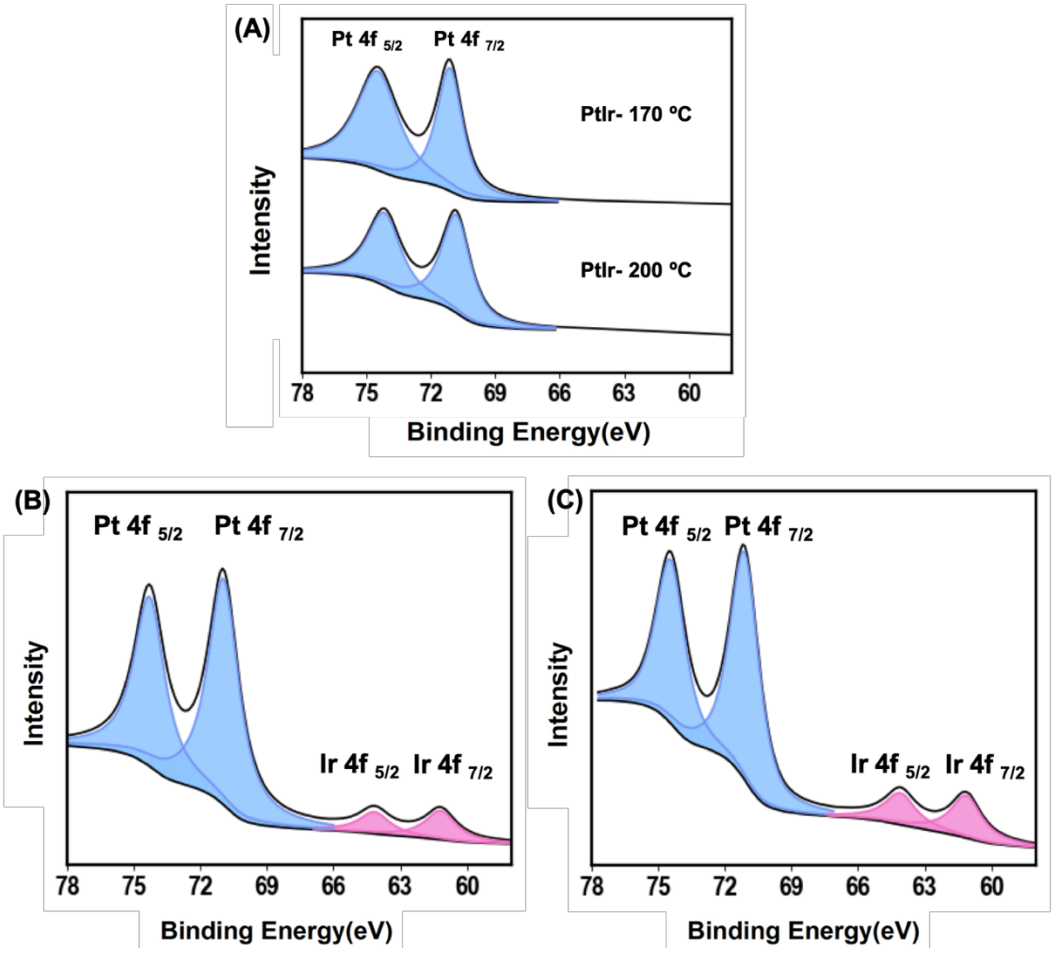

Figure 2.5 (A) XPS spectra of PtIr intermediates formed at 170 and 200 ºC during the synthesis of $Pt_{38}Ir$ NCs. The composition of the precursor solution was maintained the same except for the different reaction temperature. XPS spectra of as-obtained $Pt_{38}Ir$ NCs and $Pt_{17}Ir$ NCs (B, C).

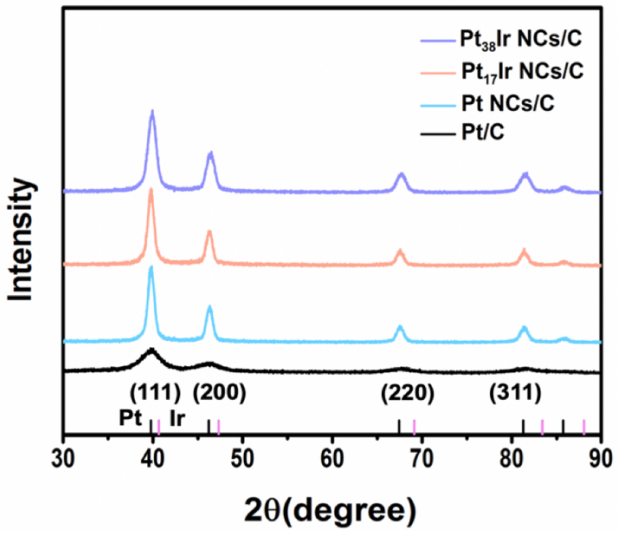

Figure 2.6 Powder XRD patterns of prepared Pt NCs/C, $Pt_{38}Ir$ NCs/C and $Pt_{17}Ir$ NCs/C electrocatalysts. A commercial Pt/C (E-TEK, 20% Pt/C) was also examined as a reference material.

To gain more insights into the NCs growth kinetics, PtIr intermediates were examined. With the synthesis temperature increases from 140 to 235 ℃, the color of the reactant solution changed from yellow to brown, with the precipitation of colloidal particles starting from 180 ℃ (**Figure 2.7**). In an attempt to synthesize Ir NCs using the same method, the color of the precursor solution remained unchanged and no precipitation was formed at the end of the reaction (**Figure 2.8**), suggesting the failure of making pure Ir NCs. Considering that the Ir^{3+} concentration in the precursor solution (e.g., 1:1 for Pt: Ir in $Pt_{17}Ir$) is much higher than the overall Ir ratio in the PtIr NCs, while the reduction potential of Pt^{2+} (1.188V) is close to Ir^{3+} (1.156V), it can be concluded that Ir^{3+} reduction is a kinetically-limited step in the reaction.[56] The successful formation of core-shell NCs

in the Pt^{2+}/Ir^{3+} co-reduction process can be ascribed to the smaller energy barrier for heterogeneous nucleation (reduction of Ir^{3+} on Pt-rich core) compared to that of homogeneous one (reduction of Ir^{3+} on Ir atoms), thus making the reduction of Ir on Pt-rich core easier (**Figure 2.9**).[57-58]

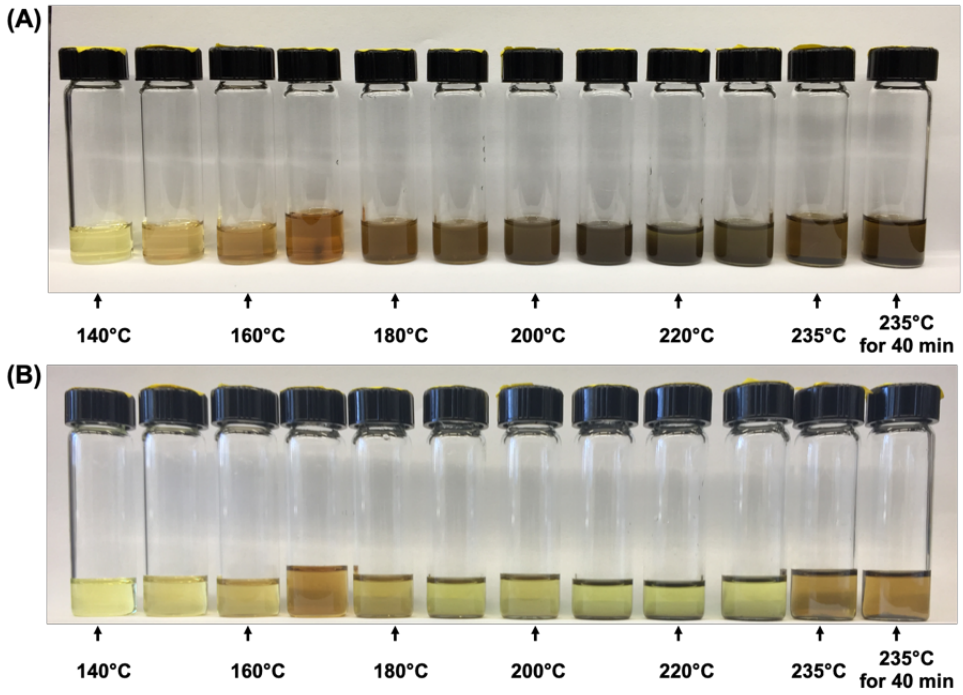

Figure 2.7 Representative solutions taken from the reaction flask right after reaction (A) and after particle precipitation (B) from reaction temperature in the range of 140 to 235 °C. The last vial on the right side shows the solution sample obtained after holding the reaction temperature at 235°C for 40 min, and the rest samples are obtained without holding at the respective reaction temperature. As indicated by the color of each solutions, NC particles begin to form starting from a temperature of 180 °C.

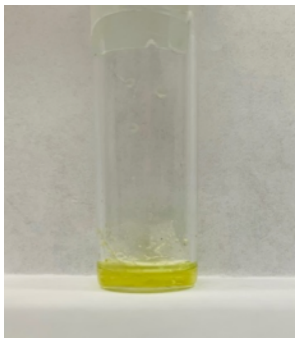

Figure 2.8 Representative Ir-reaction solution obtained from the reaction flask. In the attempt to synthesize Ir NCs, 20 mg of $Ir(acac)_3$ (Sigma-Aldrich, 97%) was dissolved in a mixed solution containing 7 ml of benzyl ether (Sigma–Aldrich, 98%), 1 ml of oleic acid (Sigma-Aldrich, 90%), and 2 ml of oleylamine (Sigma-Aldrich, 70%). The solution was heated to 130 °C under Ar protection and then $W(CO)_6$ (Sigma-Aldrich, 97%) was added during the heating process. The solution sample was taken after holding the reaction temperature at 235 °C for 40 min. As indicated by the color of the solution (no change during the heating process), no Ir NC particles can be produced.

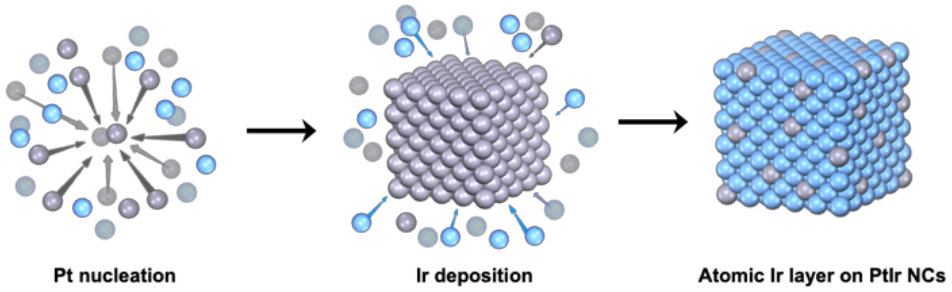

Figure 2.9 Illustration of PtIr NCs formation through a heterogenous nucleation process.

CV test was performed to assess the electrochemical properties all the electrocatalysts (**Figure 2.10A** and Table 2.3). The CV curves of Pt NCs/C exhibit typical features of single crystal Pt(100) for H adsorption/desorption, indicating the well-controlled cubic morphology with preferentially exposed (100) facets.[59] After alloying with Ir, the peaks associated with H adsorption/desorption shift toward positive potentials.

Such a shift is associated with the modification of the electronic structure of Pt, which is responsible for stronger bonding of H on the surface of PtIr NCs.[60] It is noted that as the Ir ratio increases in the PtIr core-shell NCs, the oxidation current also rises above the hydrogen underpotential deposition region (0.02-0.35V) due to the formation of IrOH and IrO.[61]

The EOR activities of all the electrocatalysts were evaluated by CV (**Figure 2.10B**). Compared with the commercial Pt/C catalyst, the Pt NCs/C catalyst with predominant Pt(100) surface facets is more active towards EOR, as suggested by its 1.9-fold peak current density than the former, indicating the beneficial role of exposing the (100) facet. The activity of $Pt_{38}Ir$ NCs/C is even higher than Pt NCs/C, reaching 4.5 times of the peak current of commercial Pt/C. Interestingly, with two times of Ir loading, the activity of $Pt_{17}Ir$ NCs/C decreases noticeably, approaching only 2.7 times of the peak current of commercial Pt/C. This trend is further confirmed by CA test, for which the current density increases in the order of Pt/C < Pt NCs/C< $Pt_{17}Ir$ NCs/C < $Pt_{38}Ir$ NCs/C at 0.45 V (**Figure 2.10C**). Such a trend suggests that only a small amount (one atomic layer) of Ir is more beneficial for high EOR activity, which opposes to previous results in PtIr alloys that higher Ir ratios in PtIr alloys lead to the enhanced EOR performance[30]. In our case, due to the formation of an Ir-rich shell, the higher oxophilicity of the Ir surface atoms decreases the ethanol adsorption at high potential, resulting in a lower EOR activity.[62] Moreover, compared to the Pt/C catalyst, the EOR onset potential and main peak potential

of $Pt_{38}Ir$ NCs/C exhibit a negative shift of 320 and 45 mV, respectively. Both $Pt_{17}Ir$ NCs/C and Pt NCs/C show a negative shift of the EOR main peak by 65 mV, while their onset potential for CO_2 formation present a negative shift of ~320 mV and ~100 mV compared to Pt/C, respectively, indicating a critical role of the thin Ir skin. Therefore, the significantly enhanced EOR activity on $Pt_{38}Ir$ NCs/C can be attributed to the combination of the predominant (100) facet and an atomic layer thickness Ir-rich shell on the NCs.

Table 2.3 Electrochemical surface area of different electrocatalysts.

Electrocatalysts	$ECSA_H$ ($m^2\ g^{-1}$)	$ECSA_{CO}$($m^2\ g^{-1}$)	Specific peak current density (mA cm^{-2})
Pt/C	85.5	80.7	0.40
Pt NCs/C	39.6	45.1	0.76
$Pt_{17}Ir$ NCs/C	37.2	42.4	1.08
$Pt_{38}Ir$ NCs/C	31.5	35.1	1.80

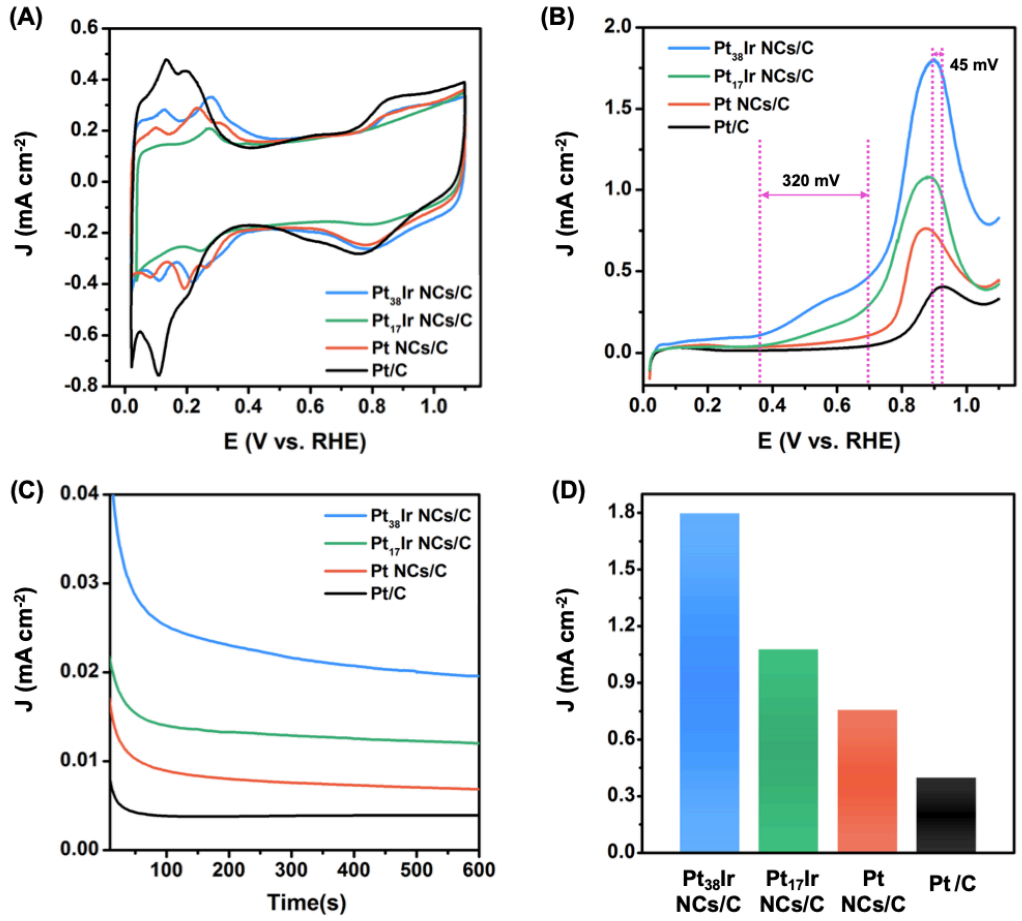

Figure 2.10 (A) CV curves of different electrocatalysts show distinct H adsorption/desorption characteristics at a scan rate of 50 mV s^{-1}. The electrolyte was Ar-saturated 0.1 M $HClO_4$ solution. (B) Anodic polarization curves for EOR of different electrocatalysts at a scan rate of 50 mV s^{-1} in Ar-saturated 0.1 M $HClO_4$ solution with 0.2 M ethanol solution. (C) CA test of all catalysts at 0.45 V (versus RHE). (D) Specific activity (SA) measured at peak potential of electrocatalysts. All the experiments were performed at 25 ^oC. The current densities are normalized to the electrochemical surface area.

In situ IRRAS experiments were carried out to identify the intermediates and products of EOR on different electrocatalysts (**Figure 2.11A-D**). Amongst all the main products, CO_2 is the complete oxidation product corresponding to the highest faradic

efficiency (FE), while acetaldehyde (CH_3CHO) and CH_3COOH are generated from partial ethanol oxidation without C-C bond cleavage. The signature peak at 2341 cm^{-1} represents the asymmetric stretch vibration of CO_2. The characteristic peak for CH_3CHO and CH_3COOH is located at 933 and 1280 cm^{-1}, respectively. Depletion of ethanol can be identified by the peak at 1044 cm^{-1}, the C-O stretching mode of ethanol. The onset potential for generating CO_2 is an indicator for the activity and selectivity of the electrocatalyst to break the C-C bond. From these IRRAS spectra, the onset potential for CO_2 is identified to be 0.45 V, 0.55 V, 0.55 V and 0.65 V for $Pt_{38}Ir$ NCs/C, $Pt_{17}Ir$ NCs/C, Pt NCs/C and commercial Pt/C, respectively. To our best knowledge, the 0.45V onset potential achieved by $Pt_{38}Ir$ core-shell NCs/C represents the lowest value for PtIr alloys.[30, 34-35] To further understand the onset stage of CO_2 formation, CA test was combined with *in situ* IRRAS (**Figure 2.11E, F**). For the $Pt_{38}Ir$ NCs/C catalyst, CO_2 starts to form after 200 s at 0.45 V, while no CO_2 can be detected on Pt NCs/C even after 600 s.

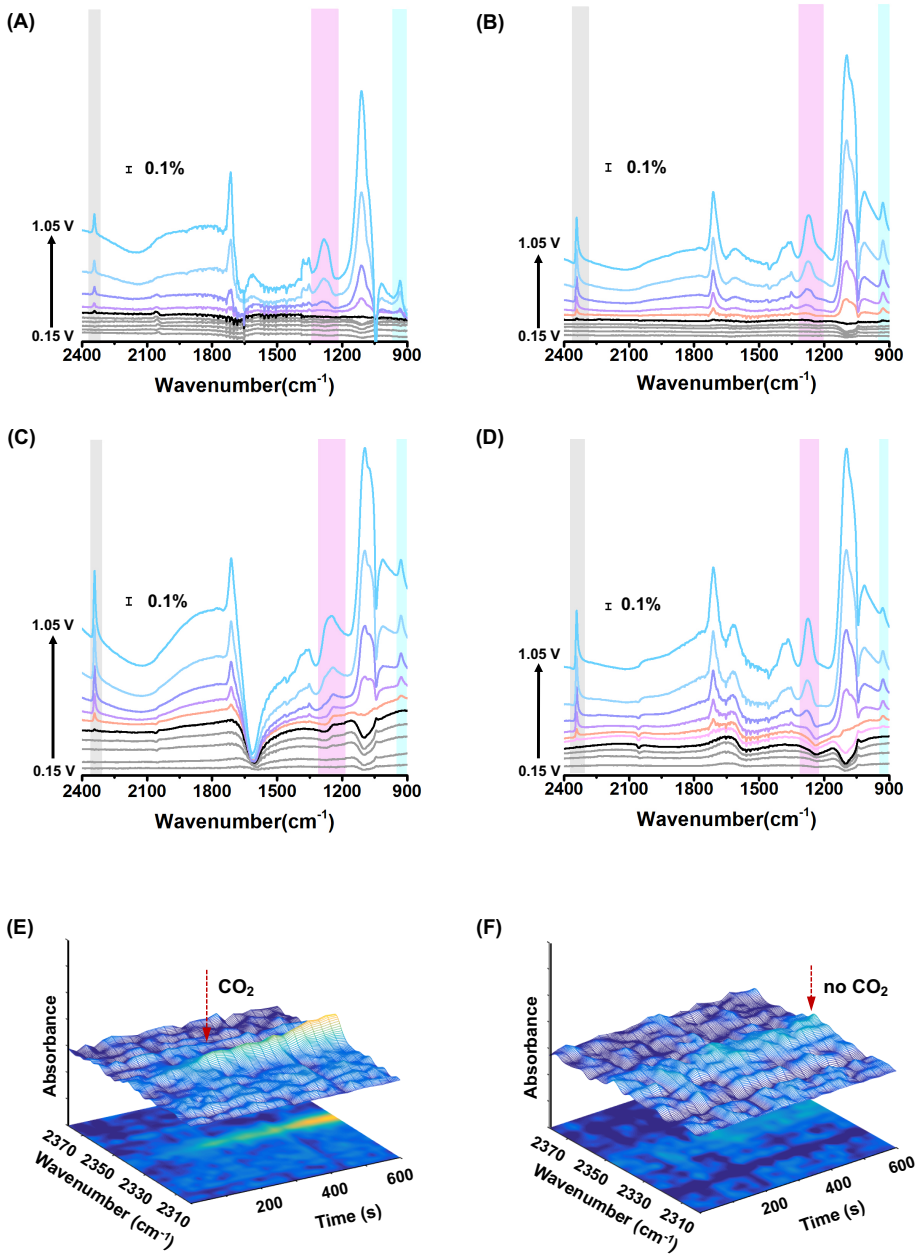

Figure 2.11 *In situ* IRRAS spectra recorded during CV test from 0.15 to 1.05 V (versus RHE) for EOR on (A) commercial Pt/C, (B) Pt NCs/C, (C) $Pt_{17}Ir$ NCs/C, and (D) $Pt_{38}Ir$ NCs/C. The data recording interval was 0.1 V. The peaks under the shaded area with grey, pink and blue color represents CO_2, CH_3COOH and CH_3CHO. The black curve in each spectrum shows the onset of CO_2 production. *In situ* IRRAS spectra recorded during CA test at 0.45 V (vs. RHE) for EOR on (E) $Pt_{38}Ir$ NCs/C and (F) Pt NCs/C. The electrolyte was Ar-saturated 0.1 M $HClO_4$ with 0.2 M ethanol. All the experiments were performed at 25 ^oC.

The selectivity toward different EOR products from 0.45 V to 1.05 V is calculated using the peak integration method developed by Weaver *et al*.[63] All the catalysts show high CO_2 selectivity on their on-set stages, but their total current density differs significantly following the order of Pt/C < Pt NCs/C < $Pt_{17}Ir$ NCs/C < $Pt_{38}Ir$ NCs/C (**Figure 2.12**). Starting from 0.85 V, the main product of commercial Pt/C is CH_3COOH and its CO_2 selectivity is only 4% (**Figure 2.13A**). For Pt NCs/C, the main products are CH_3CHO from 0.65 to 0.95 V with CH_3COOH as the dominating product at 1.05 V (**Figure 2.13B**). The highest CO_2 selectivity after the onset is only 7% (at 0.85V). These findings conclude that Pt itself favors the formation of CH_3CHO and CH_3COOH, consistent with previous reports.[34, 64] Once Ir is introduced on Pt NCs/C, both the CO_2 selectivity and overall activity dramatically improve in the potential range between 0.65 and 1.05 V. The $Pt_{38}Ir$ NCs/C catalyst exhibits CO_2 selectivity of 35%, 24% and 21% at 0.55, 0.65 and 0.75 V, respectively. Even at 0.85 V, the selectivity still reaches 18% (**Figure 2.13C**). With a higher ratio of Ir, however, the $Pt_{17}Ir$ NCs/C catalyst shows decreased CO_2 selectivity and overall current density at potentials > 0.55 V (**Figure 2.13D**). The CO_2 current densities of all the catalysts are calculated and summarized in **Figure 2.14**. The $Pt_{38}Ir$ NCs/C catalyst shows the highest CO_2 current from 0.75 to 1.05 V. For example, at 0.85 V, it shows 2.5-, 5-, and 14-fold higher current than that of $Pt_{17}Ir$ NCs/C, Pt NCs/C and commercial Pt/C, respectively. In contrast to previous reports,[30, 34]

results from the current study indicate that a lower Ir content leads to a higher CO_2 selectivity and activity. Such a conclusion is also supported by further decreased EOR activity and selectivity on $Pt_{12}Ir$ NC catalyst **(Figure 2.15).**

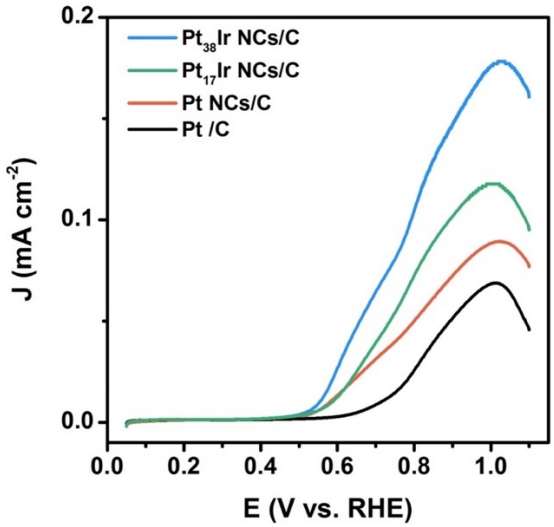

Figure 2.12 Anodic curves of electrochemical EOR for different samples collected during the *in situ* IRRAS experiment. The scan rate is 2 mV s^{-1}. The current densities are normalized to the electrochemical surface area.

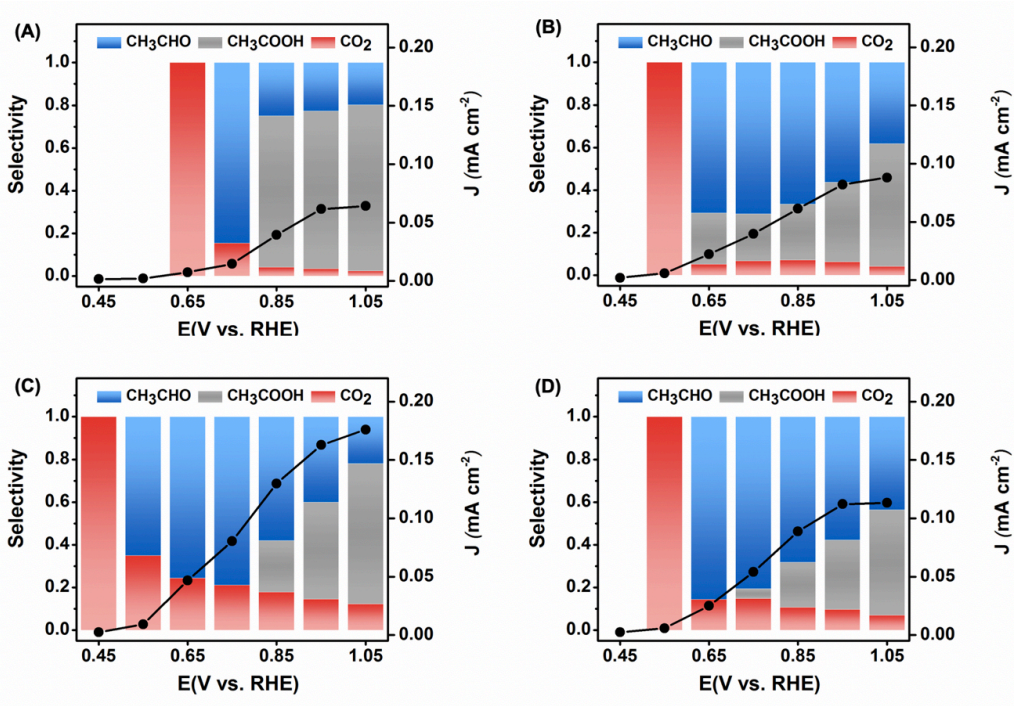

Figure 2.13 Calculated selectivity of different EOR products and overall current densities of all the electrocatalysts at different potentials: (A) commercial Pt/C, (B) Pt NCs/C, (C) $Pt_{38}Ir$ NCs/C and (D) $Pt_{17}Ir$ NCs/C. The details of the calculation method are provided in the above experiment method section.

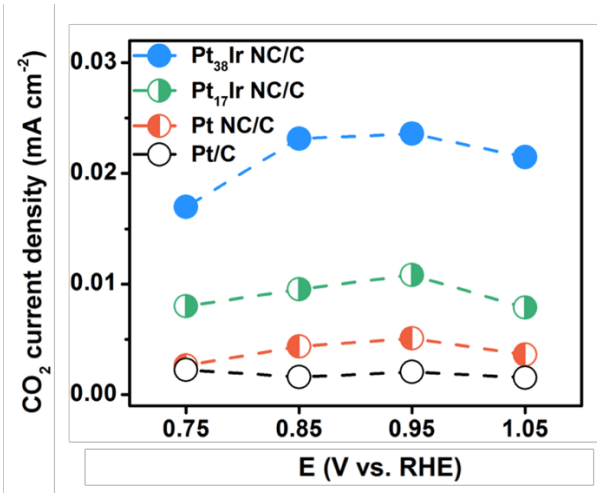

Figure 2.14 Comparison of the net current density contributed by CO_2 formation for all different electrocatalysts.

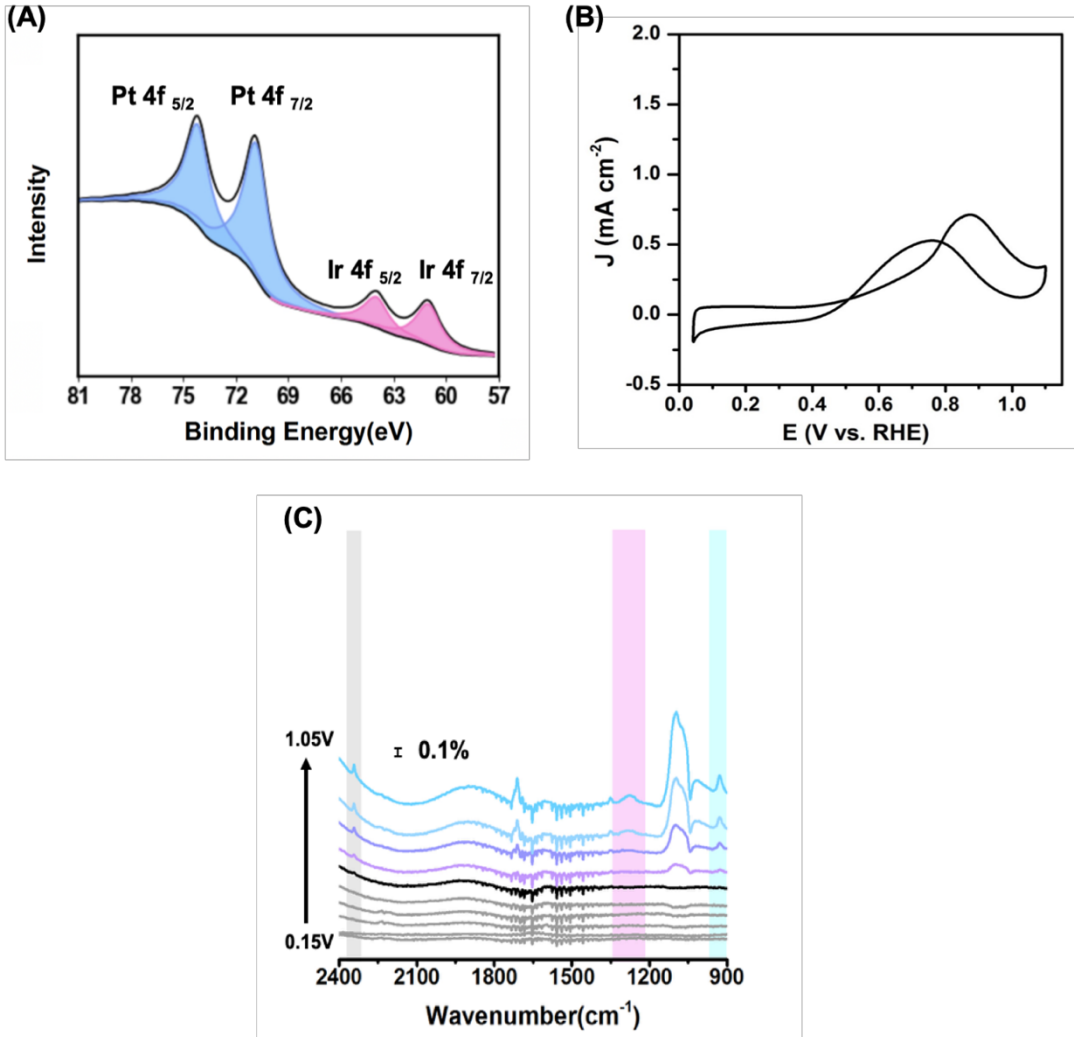

Figure 2.15 (A) XPS spectra, (B) electrochemical EOR curves and (C) in-situ IRRAS spectra of Pt12Ir/C.

DFT calculations were performed to compare the binding energies of key reaction intermediates of EOR on the Pt(100) and PtIr(100) surfaces. **Figure 2.16** show the most stable binding configurations of the reaction intermediates on PtIr(100). It is found that the binding configurations of the intermediates are very similar on Pt(100) and Ir-modified PtIr(100) surfaces, however, as shown in Table 2.4, the presence of surface Ir in PtIr(100)

enhances the binding strength of the intermediates compared to Pt(100). The DFT calculated d-band center of Ir lies higher in energy compared to Pt (d-band centers: -2.11 eV for Ir(111) and -2.25 eV for Pt(111))[65]. Thus, stronger binding of small molecules such as *O, *C and *CO is expected on Ir(111) than Pt(111). Previous DFT calculations have shown stronger binding of *O, *C and *CO on Ir(111)/(100) compared to Pt(111)/(100) [66] consistent with the predictions from the d-band theory. In the current study, DFT calculated lattice constants for fcc Pt and Ir are 3.99 Å and 3.88 Å, respectively, giving rise to a lattice mismatch (tensile strain in this case) of 2.84% (with respect to Ir). Therefore, surface Ir sites on PtIr(100) bind the ethanol electrooxidation intermediates more strongly than Pt sites because of combined effect of tensile strain and intrinsic (chemical nature) properties of Ir. A full monolayer (ML) Ir on Pt(100) thus shows the largest change in binding energies of intermediates (Table 2.4) compared to Pt(100). It is rather difficult to isolate strain, ligand and ensemble effects in bimetallic PtM catalysts that contain M atom on the surface or in the first or second subsurface layer [67-69]. Therefore, both effects are expected to contribute for the observed change in DFT calculated binding energies of the intermediates on PtIr(100) compared to Pt(100) as DFT models of PtIr(100) contain Ir on the surface. According to the Brønsted−Evans−Polanyi (BEP) relationship,[70] the enhanced binding strength of the intermediates should facilitate the C-C bond cleavage. It is expected during the reaction that the most favorable binding sites (i.e. the Ir sites) are covered by *C_xH_yO/C_xH_y species. If the *CO species formed from the C-C bond cleavage

of *C_xH_yO/C_xH_y species would adsorb on the nearby empty available Pt sites, the DFT results show that CO binding is weaker (Table 2.4) on the Pt site next to Ir, suggesting that the desorption of CO could be potentially easier on PtIr(100) compared to Pt(100). Thus, DFT calculations predict higher activity of PtIr(100) for overall EOR than Pt(100) due to facile C-C bond cleavage on the Ir sites and potentially easier CO desorption from the nearby Pt site. The DFT results suggest that the most representative bimetallic surface should contain both Ir and Pt sites, which might explain why $Pt_{38}Ir$ NCs/C (near one Ir atomic layer) is more active and selective than $Pt_{17}Ir$ NCs/C (approximately two Ir layers).

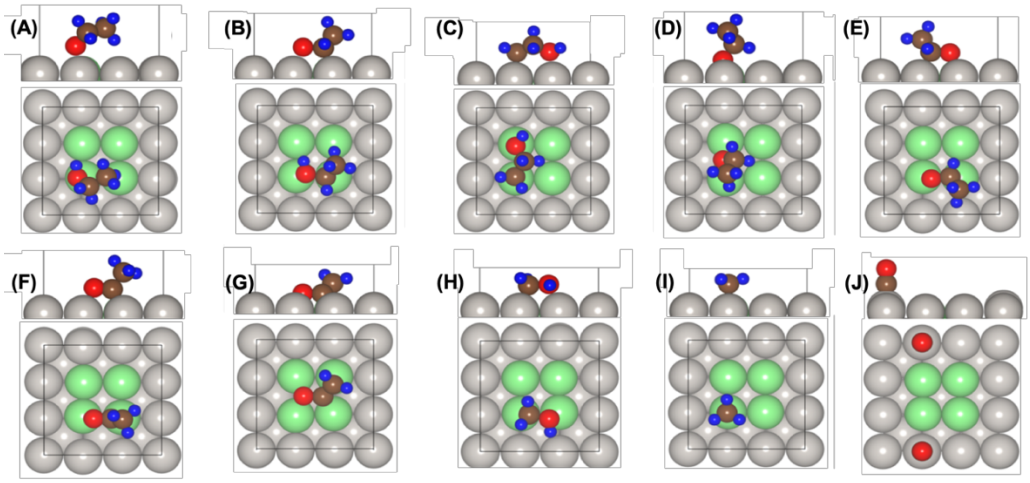

Figure 2.16 DFT optimized geometry of different EOR intermediates/products absorbed on PtIr (100) surface (Pt: gray, Ir: light green, O: red, C: brown and H: blue.)

Table 2.4 DFT calculated binding energies (BE in eV) of intermediates on Pt(100) and IrPt(100) surfaces

Adsorbates	Pt(100)	Ir_4Pt_5(100)	Ir-ML-Pt(100)
CH_3CH_2OH	-0.40	-0.67	-0.71
CH_3CHOH	-2.46	-2.52	-2.70
CH_2CH_2OH	-2.36	-2.78	-2.96
CH_3CH_2O	-2.33	-2.86	-3.10
CH_3CHO	-0.60	-1.15	-1.26
CH_3CO	-2.76	-3.22	-3.44
CH_2CO	-1.70	-2.40	-2.80
CH_2OH	-2.29	-2.64	-2.79
CH_3	-2.23	-2.43	-2.49
CO	-2.12	-2.50 (Ir), -1.92 (Pt)	-2.57

CO stripping experiments were conducted to further verify the critical role of the Ir-rich shell on the PtIr NC electrocatalysts (**Figure 2.17**). The onset potential of CO oxidation follows the same trend as that of CO_2 generation in the EOR reaction ($Pt_{38}Ir$ NCs/C < $Pt_{17}Ir$ NCs/C = Pt NCs/C < commercial Pt/C), indicating that the enhanced selectivity of EOR toward CO_2 can be due to facilitated oxidative removal of adsorbed CO. Compared with the commercial Pt/C catalyst, the main CO oxidation peak of Pt NCs/C is positively shifted by 20 mV, implying strong CO adsorption at high potential. By contrast, the main CO stripping peaks exhibit a negative shift of 10 mV for $Pt_{38}Ir$ NCs/C and 50 mV for $Pt_{17}Ir$ NCs/C compared with Pt NCs/C, indicating the beneficial role of Ir in promoting CO oxidation. This result agrees well with the DFT calculation that CO binding is weaker on the Pt site with adjunct Ir site. Considering that the onset potential of CO oxidation is much higher than that of CO_2 generation from ethanol (0.70

V versus 0.45 V), our results also suggest that CO_2 might be directly formed at lower potentials without involving CO oxidation.

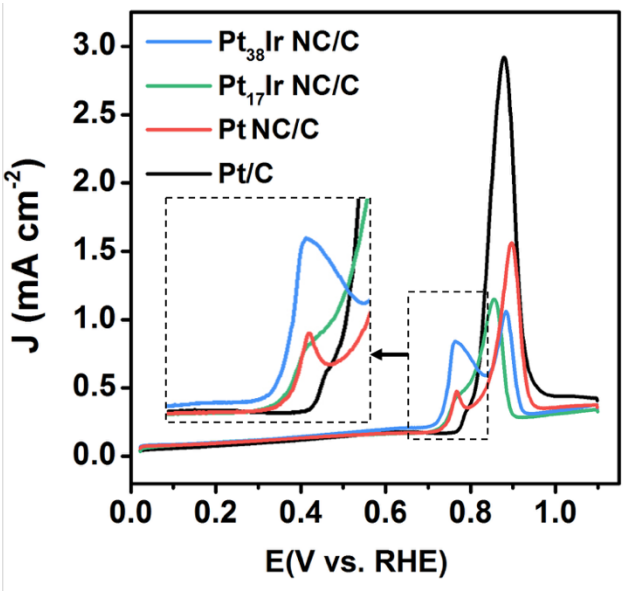

Figure 2.17 CO stripping curves of all catalysts recorded in 0.1 M $HClO_4$ at a scan rate of 50 mV s^{-1}.

Electrocatalyst stability was investigated by prolonged CA test. The EOR stability test was performed by holding the electrode potential at 0.45 V (vs. RHE) for every 10000 s followed by CV clean scans (**Figure 2.18**). The current density of the commercial Pt/C catalyst decreased by ~ 35% in the beginning of the second 10000 s. Although the Pt NCs/C showed improved stability, the current density still decreased by 33% after 30000 s. By comparison, both the $Pt_{38}Ir$ NCs/C and $Pt_{17}Ir$ NCs/C core-shell electrocatalysts exhibited much smaller current decrease (12% and 15%) after 30000 s. This result

suggests that, besides significantly improved CO_2 selectivity and overall activity, the incorporation of ultrathin Ir-rich shell (1~2 atomic layers) can also effectively improve the EOR stability of Pt-based electrocatalysts.

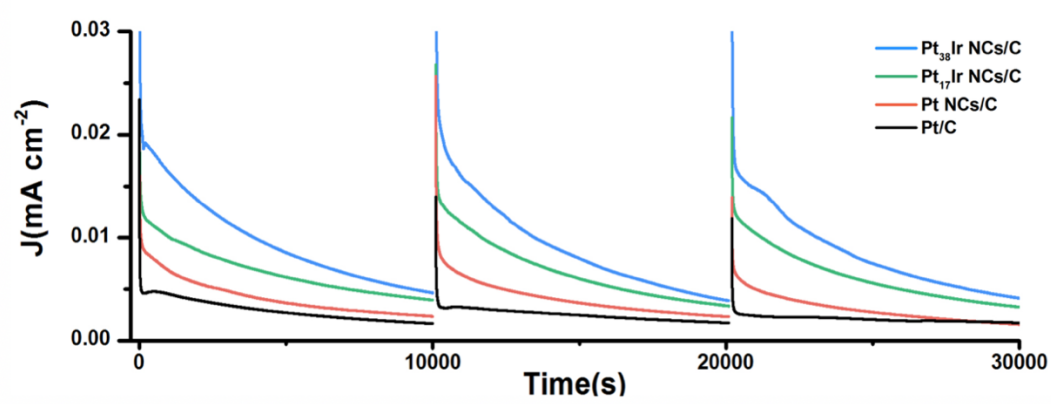

Figure 2.18 Electrochemical EOR stability test of all the electrocatalysts in an Ar-saturated 0.1 M $HClO_4$ with 0.2 M ethanol at 0.45 V (vs. RHE).

2.2.3. Conclusions

In summary, this chapter reported a facile method to synthesize PtIr alloy core-shell NCs with ultrathin Ir-rich shells as effective EOR electrocatalysts. Unlike the time-consuming ALD method, it demonstrated that colloidal synthesis can also archive precise control of active surfaces at the atomic level. With ~0.2 nm (one atomic layer) thickness of Ir-rich skin on (100)-exposed $Pt_{38}Ir$ NCs (only 2.5 wt.% of overall Ir loading), the electrocatalysts exhibit unprecedent EOR activity, high CO_2 selectivity and long-term stability, superior to commercial Pt/C, Pt NCs, $Pt_{17}Ir$ NCs, as well as the-state-of-the-art EOR catalysts reported so far. Specifically, it showed that the $Pt_{38}Ir$ NCs/C electrocatalyst

can deliver a current density up to 4.5-times higher than that of Pt/C with a lower EOR onset potential by 320 mV. In addition, it showed 14 times higher CO_2 current density at 0.85 V. In contrast, pure Pt NCs or $Pt_{17}Ir$ NCs (5.5 wt.% of overall Ir loading) catalysts offer less activity and lower CO_2 selectivity. This is also different from the previous knowledge that a higher Ir loading (50-75 wt.%) in the PtIr alloy catalyst is required to achieve higher EOR activity and CO_2 selectivity. DFT calculations suggested that the PtIr(100) surface not only favors the splitting of the C-C bond by providing strongly adsorbed binding sites of $*C_xH_yO/C_xH_y$ species, but also potentially makes the desorption of CO easier if CO is occupying the nearby Pt site, leading to an overall enhanced EOR performance. This study provides new insights on the critical the role of surface atom layers for shape-engineered EOR catalysts, and demonstrates a new strategy for the design of alloyed electrocatalysts toward high-performance DEFCs.

2.3. Single atomic Rh decorated Pt nanocubes

2.3.1. Experimental

2.3.1.1. Electrocatalysts synthesis

In a standard synthesis of Pt NCs, $Pt(acac)_2$ (0.102 mmol), OAc (2.0 mL), OAm (4.0 mL), and BE (14.0 mL) were added in a glass vial with a magnetic stirring bar. The

mixture was heated to 130 °C under an Ar atmosphere. When the temperature reached 130 °C, carbon monoxide (CO) gas was bubbled into the mixture with a flow rate of 30 mL min^{-1}, and Ar purging was stopped at the same time. The mixture was then heated to 210 °C at a heating rate of 8 °C min^{-1} under CO gas and held at 210 °C for 40 min without CO gas bubbling. The resulting suspension was cooled down to room temperature naturally, and the Pt NCs were precipitated out by sequential addition of toluene (10 mL) and ethanol (15 mL). The supernatant was discarded by centrifugation at 3,000 rpm for 5 min. The resulting Pt NCs were dispersed in toluene solution containing 40 mg of Vulcan XC-72 R carbon and kept under ultrasonic wave agitation for 30 min. The resulting Pt NCs/C catalyst was centrifuged 3 times with toluene at 3,000 rpm for 5 min, and then dried under Ar protection at room temperature.

For the preparation of Rh-decorated Pt NCs/C, as-prepared Pt NCs/C (20 mg), OAm (5 mL), and BE (5 mL) were added in a glass vial with a magnetic bar with a magnetic stirring bar. The mixture was heated to 250 °C under an Ar atmosphere. $Rh(acac)_3$ dissolved in BE (1 mL) was injected in a reaction mixture. The amount of $Rh(acac)_3$ was 1 mg (0.002 mmol) for a single atomic oxidized Rh on the Pt NCs ($Rh_{at}O$-Pt NCs) and 2 mg (0.005 mmol) for Pt NCs decorated with oxidized Rh clusters ($Rh_{cl}O$-Pt NCs). Then, reaction mixture was maintained at 250 °C for 1 hr. The resulting product was cooled down to room temperature naturally, and the Rh-decorated Pt NCs/C catalysts

were centrifuged 3 times with toluene at 3,000 rpm for 5 min, and then dried under Ar protection at room temperature.

2.3.1.2. Characterization

Transmission electron microscopy (TEM) images were obtained using a HT 7100 microscope (Hitachi, Japan) operated at an acceleration voltage of 120 kV. High-resolution TEM and EDS studies were carried out in a JEM-2100F (JEOL, Japan) and Titan G2 ChemiSTEM Cs Probe (FEI, USA) operated at an acceleration voltage of 200 kV. The metal contents in catalysts were determined using inductively coupled plasma-optical emission spectroscopy (ICP-OES, PerkinElmer, Optima 7300DV, USA) and ICP-MS (PerkinElmer, NexION 300X, USA). XRD patterns were obtained with a D2 phaser X-ray diffractometer (Bruker, USA). XPS was carried out using a spectrometer (Thermofisher Scientific, USA) with Al Kα X-ray (1486.6 eV) as the light source. All XPS spectra were aligned using the C1s peak at 284.8 eV as reference.

2.3.1.3. Electrochemical measurements

The electrocatalyst ink was prepared by dispersing 2.0 mg of electrocatalysts in mixed 2 ml of Milli-Q water and isopropanol solution (Milli-Q water: isopropanol = 4: 1) and 8 µl of Nafion (5%). 10 µl of electrocatalyst ink was used for the electrochemical test. Glassy carbon (GC), Pt flag and Ag/AgCl (3M Cl^-) were used as the working, counter,

and reference electrodes, respectively. All the potentials were calibrated to a reversible hydrogen electrode (RHE). To obtain the stable electrochemical result, 20 fast CV cycles were scanned first in Ar-saturated 0.1 M $HClO_4$ solution at 100 mV s^{-1} in the range of 0.05~1.20 V (vs. RHE). The CV curves were then recorded in the above solution with a scanning rate of 50 mV s^{-1}. The ethanol oxidation reaction (EOR) activities were measured in Ar-saturated 0.1 M $HClO_4$ and 0.2 M of C_2H_5OH solution. The EOR CV curves were obtained with a scanning rate of 50 mV s^{-1}. The CA curves were measured at 0.65 V. For CO stripping tests, CO was adsorpted on the electrocatalyst surface by holding the potential at 0.05 V for 10 min in CO-saturated 0.1 M $HClO_4$ solution. The stability test was performed by a prolong CA test at 0.55 V for every 10000s followed by the CV cleaning. 3 cycles of 10000s was examined. The CO stripping curves were obtained after purging Ar for 30 min with a scanning rate of 50 mV s^{-1}.

2.3.1.4. In-situ infrared reflection-absorption spectroscopy (IRRAS)

The IRRAS tests were performed on the Nicolet IS50 spectrometer equipped with a mercuric cadmium telluride (MCT) detector. The homemade electrochemical cell was used, including a ZnSe hemisphere window, an Au working electrode, a Ag/AgCl reference electrode and a Pt wire counter electrode.[46] The IRRAS spectra were obtained in the 0.1 M $HClO_4$ and 0.2 M of C_2H_5OH solution from 0.05 to 1.05 V. The 127

interferograms were used in the test with the 4 cm^{-1} of resolution. The obtained spectra were post processed by subtracting the first reference spectrum.

2.3.1.5. X-ray absorption fine structure (XAFS) anaylsis

The XAFS analysis was conducted on the 7-BM (QAS) beamline at National Synchrotron Light Source-II (NSLS-II) in Brookhaven National Laboratory (BNL). The obtained spectra were processed using the IFFEFFIT package[71-72]. For the extended-XAFS (EXAFS) analysis, the original EXAFS pattern (χ(k)) was weighted with k3 in order to intensify the high-k oscillation regime and was Fourier-transformed using a Hanning window. The amplitude reduction factor (S_O^2) was attained from the corresponding foil. All of the EXAFS fittings were done in the R-space.

2.3.1.6. DFT calculations

DFT[73-74] calculations were performed at GGA[75] level using the plane wave VASP code.[76-77] The core electrons were described using the projector augmented wave (PAW)[78] potentials using PW91 functionals.[79] A kinetic energy cutoff of 400 eV and 3 × 3 × 1 k-point mesh were used in all structure optimization calculations. The Pt(100) surface was modeled using a 4 layer 3 × 3 surface slab. Rh_{at}-Pt NCs in our DFT calculations were represented by Rh-atom adsorbed at the most favorable site on ML O covered Pt(100). A vacuum layer of ≈15 Å thick was added in the slab cell along the direction perpendicular

to the surface to minimize the artificial interactions between the surface and its periodic images. Atoms in the bottom two layers were fixed while all other atoms were allowed to relax during geometry optimization until the Hellmann–Feynman force on each ion was smaller than 0.02 eV/Å.

The *B.E.* of adsorbate was calculated as:

B.E.(adsorbate) = E(slab + adsorbate) - E(slab) - E(adsorbate)

where E(slab + adsorbate), E(slab), and E(adsorbate) are the total energies of the slab with adsorbate, clean slab, and adsorbate species in the gas phase, respectively.

2.3.2. Results and discussions

The $Rh_{at}O$-Pt NCs/C were prepared from a two-step solution method, with Pt NCs/C being prepared first as the substrate for further Rh decoration. During the synthesis of Pt NCs, CO gas was used directly instead of the common capping agent metal carbonyls such as $W(CO)_6$ to avoid the pollution of trace amount of metal [80]. **Figure 2.19A and B** showed as-prepared Pt NCs with an average edge length of 10.8 ± 1.0 nm and Pt NCs/C, respectively. The atomic level decoration of Rh on Pt NCs/C was achieved by adding a trace amount of Rh precursors (Rh(III) acetylacetonate, $Rh(acac)_3$) in the organic mixture containing Pt NCs/C (see the Supporting Information (SI) for details). In order to thermally decompose the six metal-to-ligand bonds in $Rh(acac)_3$, a reaction temperature of 250 °C was applied, which is 40 °C higher than that of the Pt NCs synthesis. In addition,

this high temperature condition was sufficient to break the Rh-Rh bonds, preventing the clustering of Rh atoms (Volmer−Weber mode) due to the high surface free energy and the interatomic bond energy (93 kJ mol^{-1})[81-82]. Therefore, we expected that the thermally decomposed Rh atoms favor a single atom distribution rather than cluster or particle growth on the surface of Pt NCs. By adding twice of the amount of Rh precursor in a similar procedure, the Rh atoms clustered and $Rh_{cl}O$-Pt NCs were obtained. After the Rh decoration, the cubic morphologies were maintained with average edge lengths of 10.4 ± 1.2 nm and 10.9 ± 1.3 nm for $Rh_{at}O$-Pt NCs/C and $Rh_{cl}O$-Pt NCs/C, respectively (**Figure 2.19C and D**). The same *d*-spacings of the Pt(200) plane (0.196 nm) were observed for $Rh_{at}O$-Pt NCs/C and $Rh_{cl}O$-Pt NCs/C, suggesting the non-alloy formation during the decoration process (**Figure 2.20**). The HAADF- STEM with EDS elemental mapping images of $Rh_{at}O$-Pt NCs/C and $Rh_{cl}O$-Pt NCs/C represented the weak Rh signals in the outer layer of Pt NCs (white dots region in **Figure 2.20**), suggesting that Rh was distributed on the surface of Pt NCs without the formation of Rh shell. The O signals were evenly distributed over the single cubes, revealing the presence of oxygen in both samples. To further examine the decorated structure of $Rh_{cl}O$-Pt NCs/C, STEM-EDS line scan profiles were conducted at five different locations on a single $Rh_{cl}O$-Pt NC (**Figure 2.21**). As marked by the black arrows, the Rh signals were traced or not traced at the edges of each line, indicating the clusterized Rh on Pt NC, but not the full coating of Rh shell. The chemical states of Pt and Rh were identified by XPS. Both Pt and Rh were in the oxidized

form, as indicated by the presence of Pt(II) in the deconvoluted 4*f* peaks and positively shifted Rh 3p peaks in both samples (**Figure 2.22**). The quantitative Pt-to-Rh ratios of samples were determined by inductively coupled plasma-atomic emission spectroscopy (ICP-AES), suggesting stoichiometric composition of $Rh_1Pt_{19.8}$ and $Rh_1Pt_{11.4}$ for $Rh_{at}O$-Pt NCs/C and $Rh_{cl}O$-Pt NCs/C, respectively (Table 2.5).

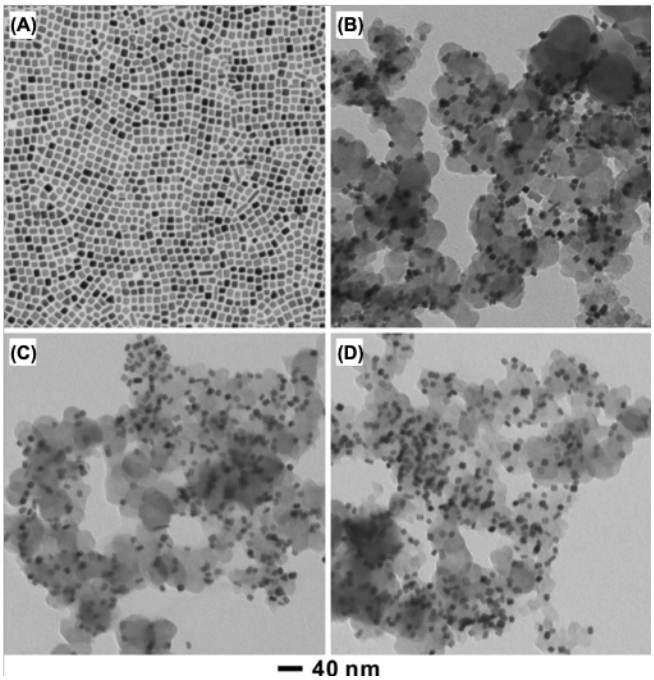

Figure 2.19 TEM images of (A) Pt NCs, (B) Pt NCs/C, (C) $Rh_{at}O$-Pt NCs/C, and (D) $Rh_{cl}O$-Pt NCs/C.

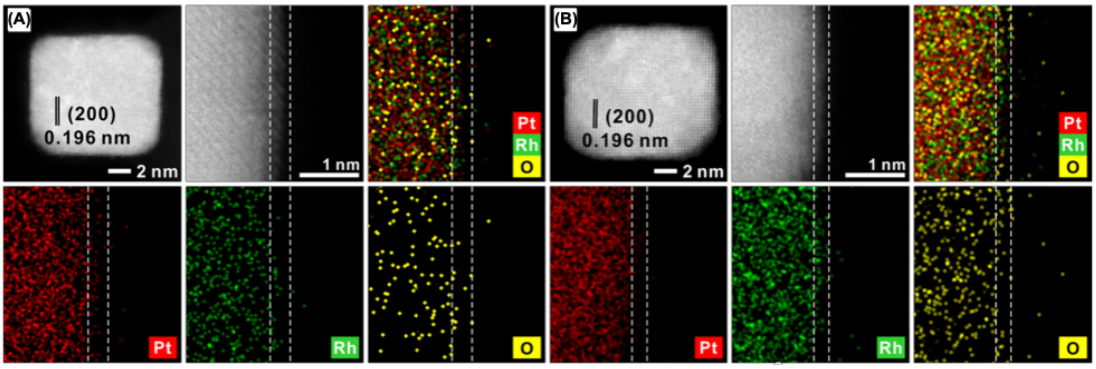

Figure 2.20 HAADF-STEM images and EDS mapping image of (A) $Rh_{at}O$-Pt NCs, and (B) $Rh_{cl}O$-Pt NCs.

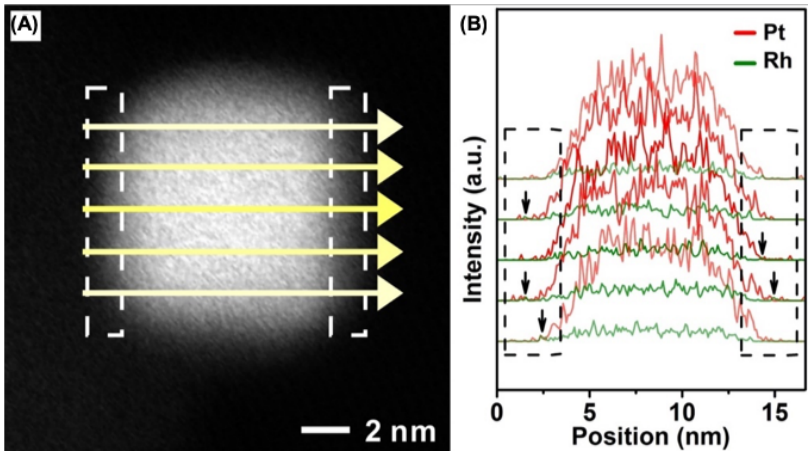

Figure 2.21(A) The HAADF-STEM image of the $Rh_{cl}O$-Pt NCs and (B) the corresponding EDS line scans along the yellow arrows. Black arrows in (B) indicates Rh signal at the Pt surface.

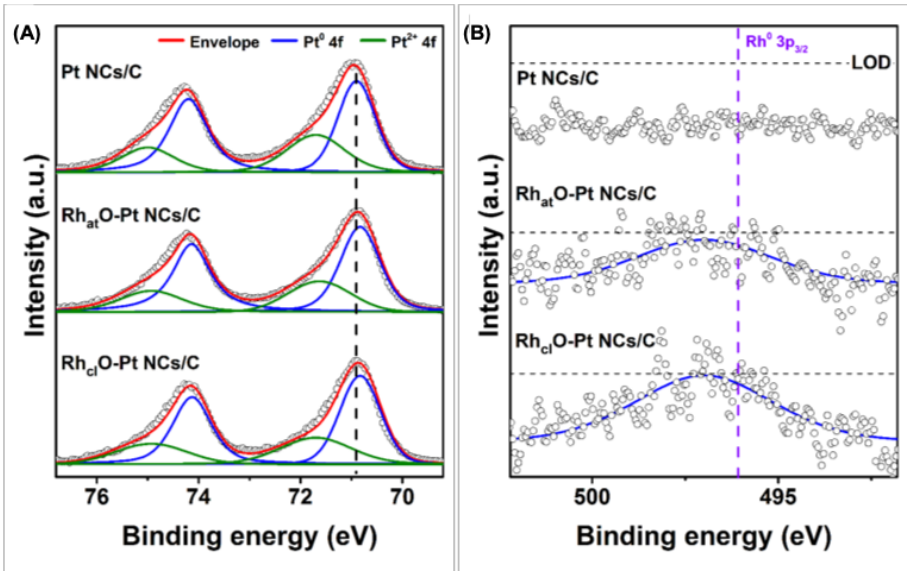

Figure 2.22 (A) Pt 4f and (B) Rh 3p XPS spectra of Pt NCs/C, $Rh_{at}O$-Pt NCs/C, and $Rh_{cl}O$-Pt NCs/C.

Table 2.5 Summary of the Rh/Pt molar ratios, electrochemical surface area from CO stripping ($ECSA_{co}$) of Pt-based catalysts

Catalyst	Rh : Pt ratio	$ECSA_{CO}$ [$m^2\ g_{Pt}^{-1}$]
Commercial Pt/C	NA*	80.2
Pt nanocubes/C	NA*	42.1
$Rh_{at}O$-Pt NCs/C	1 : 19.8	30.3
$Rh_{cl}O$-Pt NCs/C	1 : 11.4	32.9

*Not applicable

To further explore the coordination structure and the nature of Rh decoration in both samples, XAFS measurements were carried out. The X-ray absorption near edge structure (XANES) and EXAFS profiles of Pt (**Figure 2.23**, Tables 2.6.-2.10.) indicated the absence of Pt-Rh peaks (2.68 Å) in both samples[83]. Different from the XPS result, the

nearly identical XANES spectra of samples and the Pt foil revealed the metallic status of Pt in the bulk. Therefore, it could be concluded that only surface Pt was oxidized to a certain extent since XPS is a surface-sensitive technique. Unlike in the Pt L_3-edge, the XANES profiles of Rh K-edge (**Figure 2.23**) represented the Rh oxidation state of samples. EXAFS profiles at the Rh K-edge displayed distinguishable features from those of the Rh foil. The strong peak near ~1.5 Å and the absence of the Rh-Pt peak in the EXAFS profile (**Figures 2.24**) are attributed to the presence of oxidized Rh atoms, which indicate that Rh atoms are preferentially located on the aforementioned oxygen atoms on the Pt NC surfaces. In addition, there was no Rh-Rh peak for Rh_{at}-Pt NCs/C. These results confirm our synthetic approach to atomically dispersing Rh on the surface of Pt NCs. While Rh_{at}O-Pt NCs/C exclusively revealed the Rh–O–Pt bonding with its coordination number of 3.2(6) (Table 2.9), Rh_{cl}O-Pt NCs/C displayed not only Rh–O–Pt bonding but also metallic Rh–Rh bonding with their coordination numbers being 1.7(1) and 1.7(3), respectively (Table 2.10). The presence of the latter bonding could be verified by the peak near ~2.6 Å with an asterisked mark (*) in **Figure 2.23**. These Rh coordination data are in good agreement with the Rh oxidation trend obtained by XANES. Based on the XAFS observations, expected surface models were illustrated for Rh_{at}O-Pt NC and Rh_{cl}O-Pt NC (**Figure 2.25**).

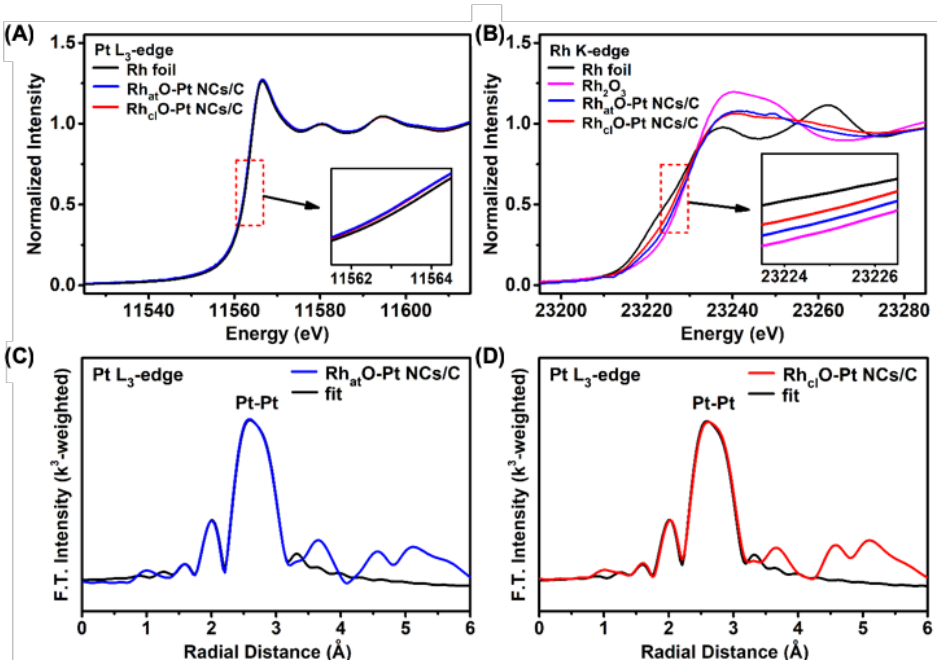

Figure 2.23 XANES spectra of the $Rh_{at}O$-Pt NCs/C and $Rh_{cl}O$-Pt NCs/C for the (A) Pt L_3-edge and (B) Rh K-edge. The k^3-weighted Pt L_3-edge EXAFS spectra of (C) $Rh_{at}O$-Pt NCs/C and (D) $Rh_{cl}O$-Pt NCs/C.

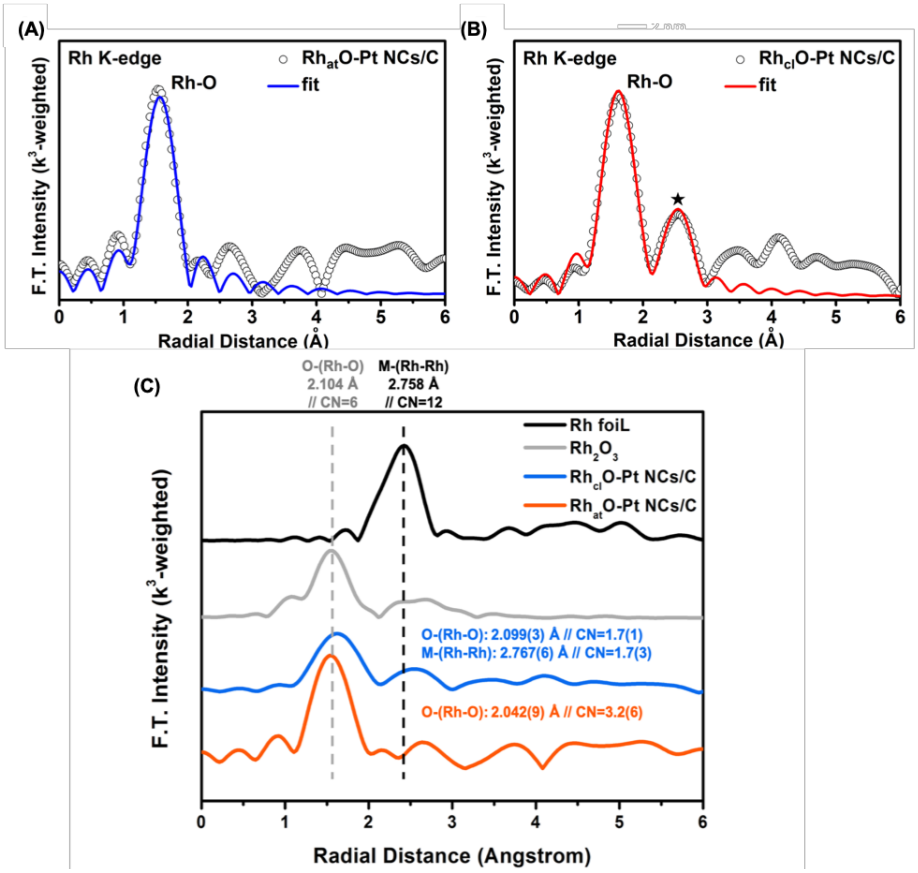

Figure 2.24 The k_3-weighted Rh K-edge EXAFS spectra of (A) $Rh_{at}O$-Pt NCs/C and (B) $Rh_{cl}O$-Pt NCs/C. (C) Comparison of Rh EXAFS spectra in Rh foil, Rh_2O_3, $Rh_{at}O$-Pt NCs/C and $Rh_{cl}O$-Pt NCs/C.

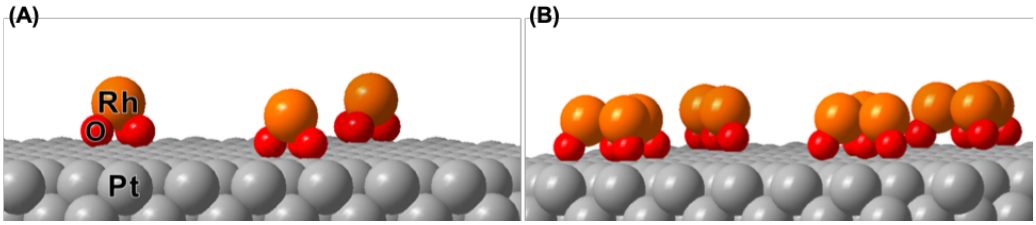

Figure 2.25 Schematic models of (A) $Rh_{at}O$ and (B) $Rh_{cl}O$ decorated Pt surface.

Table 2.6 The structure model used in the EXAFS fitting.

Model 1	
Chemical formula	Pt
Space group	Fm-3m
Lattice constant	3.923 Å
Atomic position	Pt (0,0,0)
Model 2	
Chemical formula	Rh
Space group	Fm-3m
Lattice constant	3.849 Å
Atomic position	Rh (0,0,0)
Model 3	
Chemical formula	Rh_2O_3
Space group	R-3c
Lattice constant	a=b=5.300 Å, c=14.100 Å
Atomic position	Rh (0,0,0.1506) O (0, 0.2996, 0.7500)

Table 2.7 EXAFS fitting parameters at Pt L_3-edge for $Rh_{cl}O$-Pt NCs/C.

Path	Model C.N.	Fitted C.N.	R_{fit} (Å)	E (eV)	σ^2 (Å^2)	Model
Pt-Pt	12	11.0(5)	2.763(2)	7.6(4)	0.0049(3)	Pt

Independent Points	14.5810547
Number of Variables	4
$\chi 2$	13256.5271604
Reduced $\chi 2$	1252.8549896
R factor	0.0056985
k Range for Fourier Transformation	3.000 – 12.540
R Range for EXAFS Fitting	1 – 3.463

Table 2.8 EXAFS fitting parameters at Pt L_3-edge for $Rh_{at}O$-Pt NCs/C.

Path	Model C.N.	Fitted C.N.	R_{fit} (Å)	E (eV)	σ^2 (Å^2)	Model
Pt-Pt	12	10.3(5)	2.761(2)	7.6(4)	0.0046(3)	Pt
Independent Points			13.2890625			
Number of Variables			4			
$\chi 2$			174.9960030			
Reduced $\chi 2$			18.8389305			
R factor			0.0039915			
k Range for Fourier Transformation			3.000 – 12.540			
R Range for EXAFS Fitting			1 – 3.223			

Table 2.9 EXAFS fitting parameters at Rh K-edge for $Rh_{cl}O$-Pt NCs/C.

Path	Model C.N.	Fitted C.N.	R_{fit} (Å)	E (eV)[a]	σ^2 (Å^2)	Model
Rh-O	6	1.7(1)	2.099(3)	6.36	0.0046(3)	Rh_2O_3
Rh-Rh	12	1.7(3)	2.767(6)	–8.26	0.010(2)	Rh
Independent Points			8.2968750			
Number of Variables			6			
$\chi 2$			3.6017251			
Reduced $\chi 2$			1.5680980			
R factor			0.0026199			
k Range for Fourier Transformation			2.763 – 10.000			
R Range for EXAFS Fitting			1.2 – 3.06			

[a] This value was fixed during the fit because of the limited independent variables.

Table 2.10 EXAFS fitting parameters at Rh K-edge for RhatO-Pt NCs/C.

Path	Model C.N.	Fitted C.N.	R_{fit} (Å)	E (eV)[a]	σ^2 (Å^2)	Model
Rh-O	6	3.2(6)	2.042(9)	7.02	0.003(2)	Rh_2O_3
Independent Points			5.5253906			
Number of Variables			3			
$\chi 2$			29.5956353			
Reduced $\chi 2$			11.7192379			
R factor			0.0244774			
k Range for Fourier Transformation			3.054 – 10.004			
R Range for EXAFS Fitting			1.063 – 2.357			

[a] This value was fixed during the fit because of the limited independent variables.

The CV test also exhibited different surface properties of prepared electrocatalysts (**Figure 2.26A**). The Pt(100) surface of Pt NCs/C was identified by the typical H adsorption/desorption features (0.08-0.45 V) of single crystal Pt(100) shown in its CV curves.[59] The distinct surface elemental distributions of Rh_{at}O-Pt NCs/C and Rh_{cl}O-Pt NCs/C were represented by the reduction peaks of M-O (M = Pt or Rh). The cathodic CV curve of Rh_{at}O-Pt NCs/C included the reduction of Pt-O (0.75 -1.0 V) and Rh-O (0.45 -0.65 V) peaks, confirming that both Pt and Rh were present on the surface. While for Rh_{cl}O-Pt NCs/C, the absence of an obvious reduction peak of Pt-O implied a Rh dominated surface due to the decoration of Rh clusters.

The preferentially exposed Pt(100) facets of Pt NCs/C were active toward EOR, presented by the negatively shifted onset potential of 200 mV in comparison with Pt/C (**Figure 2.26B**). However, the enhancement in terms of current densities was limited; the

current density of Pt NCs was only 1.7-fold higher than that of commercial Pt/C at 0.75 V. After Rh decoration, not only were the EOR overpotentials further reduced, but the current densities also showed significant improvement. For example, compared to Pt/C, $Rh_{at}O$-Pt NCs/C showed a more negative shift of the EOR onset and main peak potential by 350 mV and 85 mV, respectively (**Figure 2.26B**). Furthermore, the EOR current densities of $Rh_{at}O$-Pt NCs/C and $Rh_{cl}O$-Pt NCs/C showed 10.4-fold and 6.7-fold enhancement over Pt/C at 0.75 V, respectively (**Figure 2.26C**). The CA test also showed the same EOR activity trend of electrocatalysts: Pt/C < Pt NCs/C< $Rh_{cl}O$-Pt NCs/C < $Rh_{at}O$-Pt NCs/C at 0.65 V (**Figure 2.26D**). As for the decoration effect, $Rh_{at}O$ is better for EOR than $Rh_{cl}O$. To explore the reasons, Rh nanocubes/C (Rh NCs/C) and Rh NCs with decorated Pt clusters ($Pt_{cl}O$-Rh NCs/C) were prepared. Rh NCs/C performed weakly for EOR, but the EOR activity of $Pt_{cl}O$-Rh NCs/C was enhanced by 83% after the deposition of Pt clusters (**Figure 2.27**). Therefore, the EOR activity is mainly from Pt rather than Rh. Then the enhancement from the $Rh_{at}O$ and $Rh_{cl}O$ could be attributed to the Rh-O bonds, which might facilitate the formation of adsorbed OH species to remove the strongly adsorbed *CO during the EOR. Moreover, the $Rh_{at}O$ give full play to Rh-O advantages with occupying the minimum Pt active sites toward EOR. The stability of $Rh_{at}O$-Pt NCs/C was examined by a prolonged CA test at 0.55 V for every 10000s followed by the CV cleaning scans (**Figure 2.28**). After CV cleaning to remove the

poisoned intermediates, the current density of $Rh_{at}O$-Pt NCs/C could be recovered during each CA test.

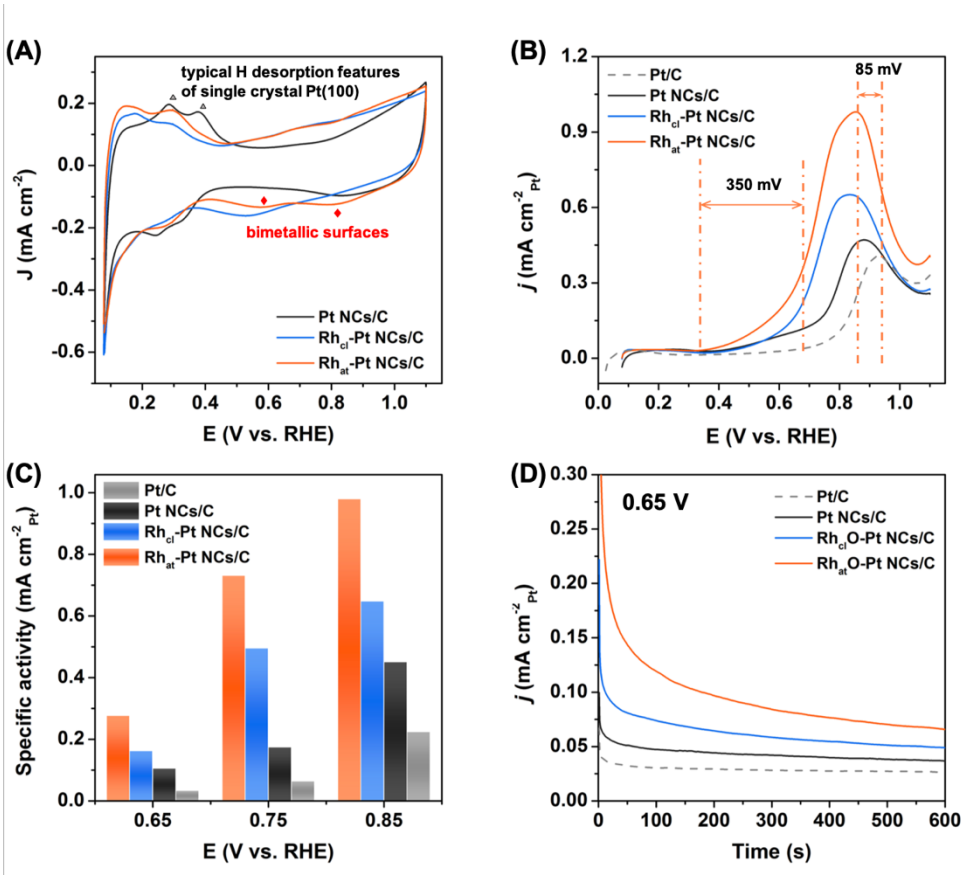

Figure 2.26 (A) CV curves of prepared electrocatalysts in Ar-saturated 0.1 M $HClO_4$ solution. (B) Anodic polarization EOR curves for electrocatalysts in Ar-saturated 0.1 M $HClO_4$ + 0.2 M ethanol solution. The scan rate is 50 mV s^{-1}. (C) Specific activity (SA) measured at certain potential of electrocatalysts. (D) The CA test of all samples at 0.65 V. The current densities are normalized to the electrochemical surface area.

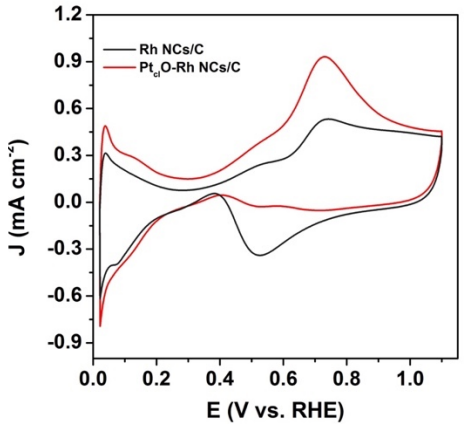

Figure 2.27 EOR curves of Rh NCs/C and $Pt_{cl}O$-Rh NCs/C in an Ar-saturated 0.1 M $HClO_4$ + 0.2 M ethanol solution. The current densities are normalized to the geometric surface area.

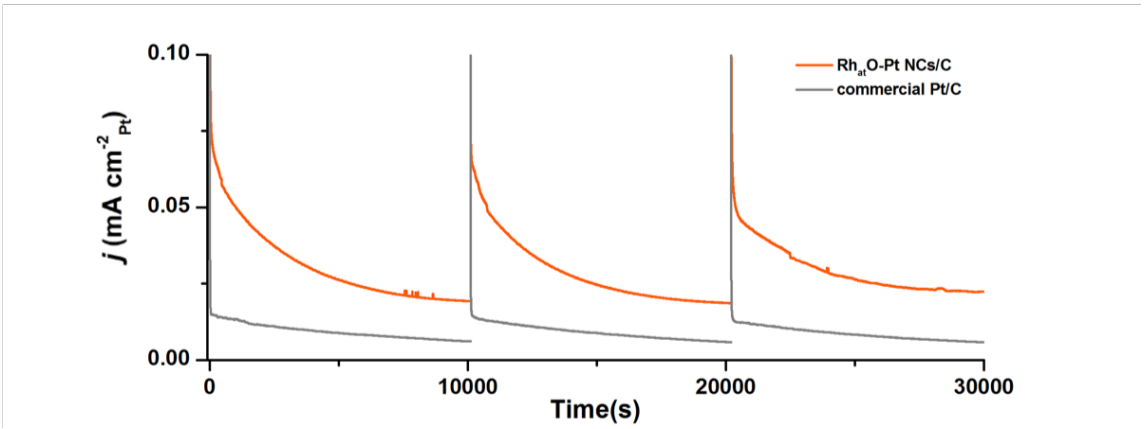

Figure 2.28 Electrochemical EOR stability test of $Rh_{at}O$-Pt NCs/C and Pt/C in an Ar-saturated 0.1 M $HClO_4$ with 0.2 M ethanol at 0.55 V (vs. RHE).

The advantage of $Rh_{at}O$ decoration is more prominent for improving the ethanol fuel utilization by complete oxidizing ethanol to CO_2. The onset potential for CO_2 formation indicates the ability of the electrocatalyst to break the C-C bond. The potential for the initial generation of CO_2 peak of electrocatalysts followed the order: $Rh_{at}O$-Pt

NCs/C (0.35 V) < $Rh_{cl}O$-Pt NCs/C (0.45 V) < Pt NCs/C (0.55 V) < commercial Pt/C (0.65 V). The CO_2 generation potential of $Rh_{at}O$-Pt NCs/C was the closest to the thermodynamic potential for the oxidation of ethanol to CO_2 (0.143 V), demonstrating its high activity to break the C-C bond. Besides, the peak located at 1705 – 1706 cm^{-1} represents the C=O stretching of C2 products (CH_3CHO and CH_3COOH). As shown in **Figure 2.29**, even at 1.05 V the IRRAS spectra of $Rh_{at}O$-Pt NCs/C still showed the negligible peak of 1705 – 1706 cm^{-1}, suggesting that only trace amount of C2 products were produced during the EOR.

The distribution of different EOR products were calculated quantitatively from 0.35 V to 1.05 V via the peak integration method developed by Weaver *et al*[63] (**Figure 2.30**). Consistent with previous reports, the main product for Pt NCs/C and Pt/C was CH_3COOH, and Pt NCs/C presented a higher CO_2 selectivity than Pt/C (17.0% vs 2.4% at 1.05 V).[34, 64] It was noted that the CO_2 selectivity of Pt NCs/C was much higher than the previous study using $W(CO)_6$ to synthesis Pt NCs, confirming the importance of a clean Pt surface without trace amount of W metal in EOR[7, 80]. The Rh decoration remarkably improved the CO_2 selectivity. The $Rh_{at}O$-Pt NCs/C catalyst exhibited 100% CO_2 selectivity from 0.35 V to 0.75 V, demonstrating its strong ability to break the C-C bond of ethanol in a wide potential range. We believe this is the first case that achieved complete oxidation of ethanol to CO_2 in such a wide potential range. The CO_2 selectivity of $Rh_{at}O$-Pt NCs/C is still very high after 0.75 V, such as 32% of CO_2 selectivity at 1.05

V. Consistent with the trend in EOR activity, the $Rh_{at}O$ decoration is better than the $Rh_{cl}O$ on Pt NCs for the C-C bond scission in ethanol.

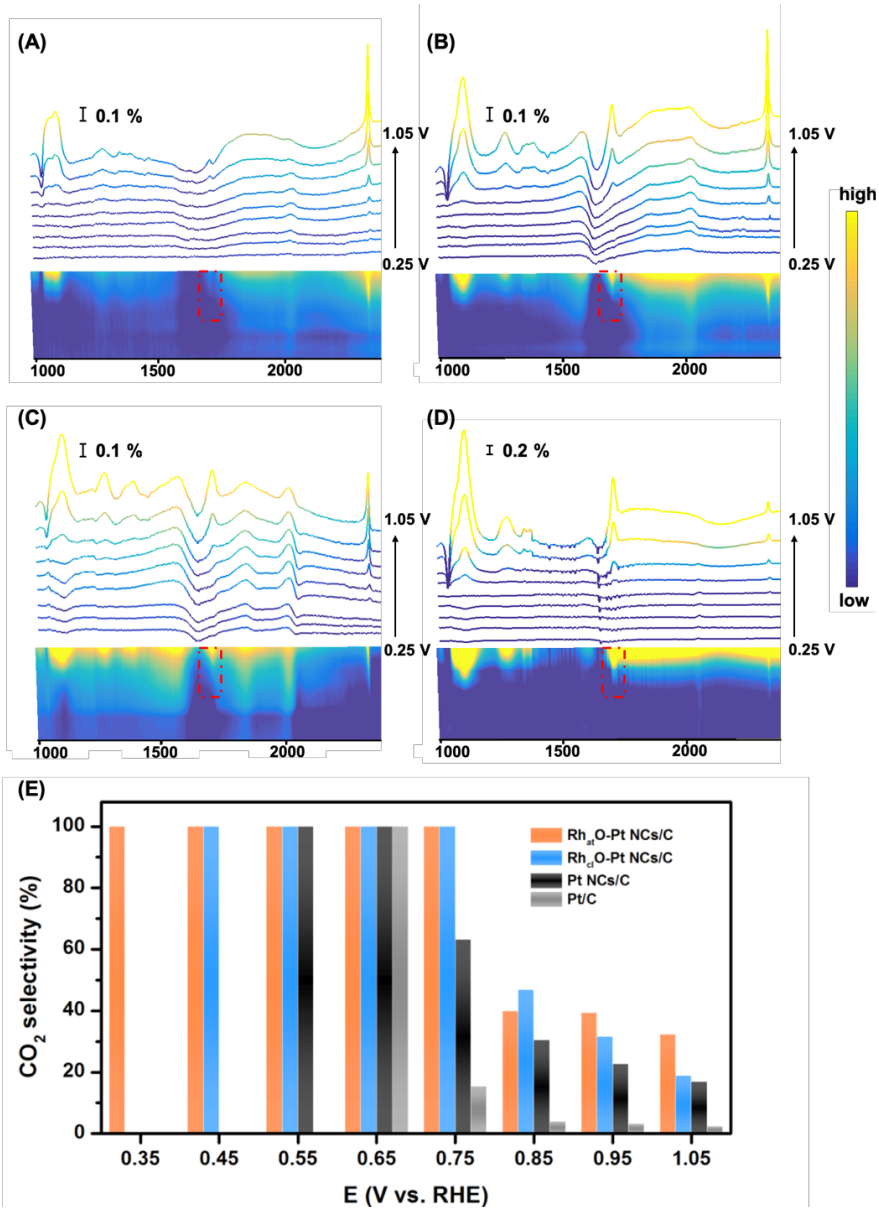

Figure 2.29 Recorded *in-situ* IRRAS spectra during CV test from 0.25 to 1.05 V on (A) Rh_{at}-Pt NCs/C, (B) Rh_{cl}-Pt NCs/C, (C) PtNCs/C, and (D) commercial Pt/C in 0.1 M $HClO_4$ + 0.2 M ethanol solution. The red dot regions highlighted the projection files of the peak at 1705 – 1706 cm^{-1}. (E) The calculated CO_2 selectivity of all samples from 0.25 V to 1.05 V.

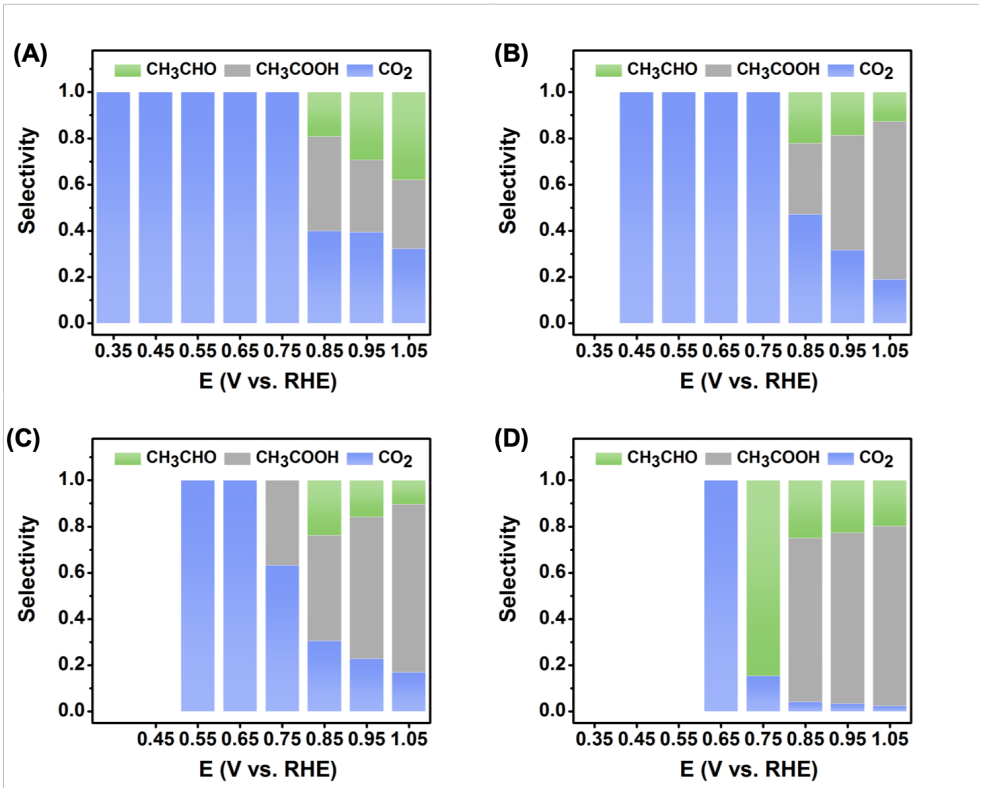

Figure 2.30 The quantitative distribution of EOR products at different potentials: (A) $Rh_{at}O$-Pt NCs/C, (B) $Rh_{cl}O$-Pt NCs/C, (C) Pt NCs/C and (D) commercial Pt/C.

Specifically, the role of Rh in breaking the C-C bond was also evidenced by the *in-situ* IRRAS spectra of Rh NCs/C and Pt_{cl}-Rh NCs/C (**Figure 2.31**). For Rh NCs/C, in spite of its low activitythe CO_2 peak was generated at the beginning of the EOR (0.15 V) without the detection of CO peak. While for Pt_{cl}-Rh NCs/C, the CO_2 peak was visible from 0.55 V and the CO peak was formed from 0.35 V. Thus, the role of Rh and Pt in EOR are clearly illustrated: Rh as the active component to break the C-C bond in ethanol directly and Pt as the active center for the EOR activity. Therefore, Rh-O-Pt can

combine the above benefits and additionally assist the formation of surface OH to remove the poisoning *CO, as confirmed in the CO stripping analysis (Figure 2.32). The oxidation of CO began in the order of $Rh_{at}O$-Pt NCs/C, $Rh_{cl}O$-Pt NCs/C, Pt NCs/C and commercial Pt/C, presenting the higher capability of $Rh_{at}O$-Pt NCs/C to remove CO. The above results suggest the unique role of the single $Rh_{at}O$ decoration on shape-controlled electrocatalyst to effectively break the C-C bond.

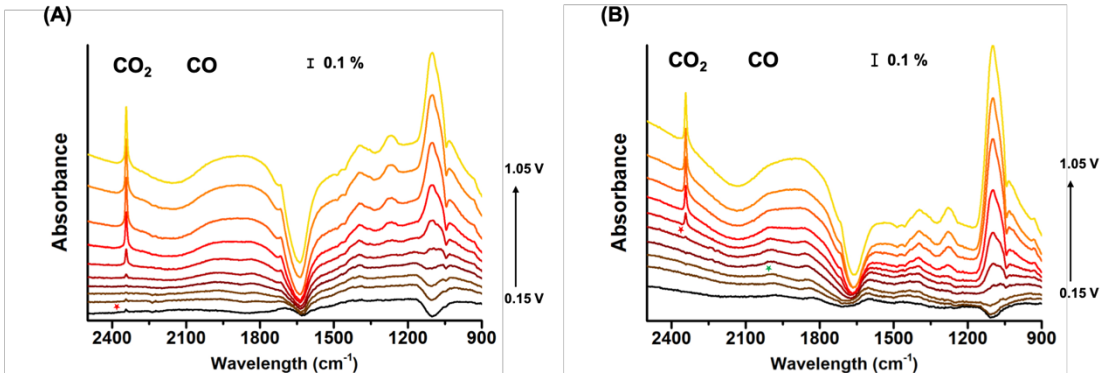

Figure 2.31 Recorded *in-situ* IRRAS spectra during CV test from 0.15 to 1.05 V on (A) Rh NCs/C, (B) $Pt_{cl}O$-Rh NCs/C in 0.1 M $HClO_4$ + 0.2 M ethanol solution. The red asterisks represent the initial CO_2 peak in both samples. The green asterisks represent the CO peak in $Pt_{cl}O$-Rh NCs/C.

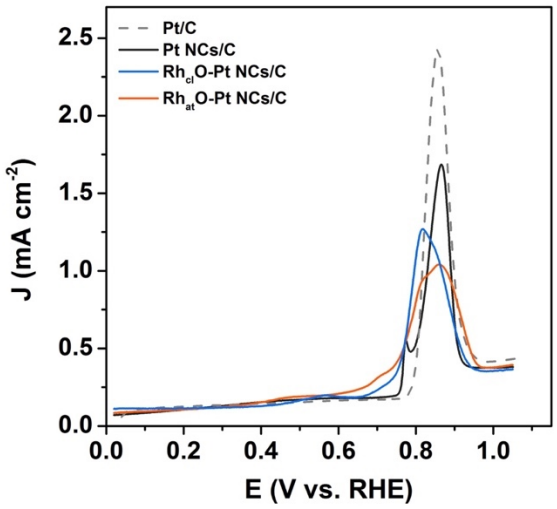

Figure 2.32 CO stripping curves of different electrocatalysts in 0.1 M $HClO_4$ at a scan rate of 50 mV s^{-1}.

DFT calculations were performed to gain further insight into the role of Rh-O-Pt sites in EOR, in particular for the removal of *CO. The DFT calculated binding energies of intermediates in their most stable configurations (**Figure 3.33 and Table 2.11**) show that $Rh_{at}O$ species on Pt(100) enhances the adsorption of CH_3CH_2OH leading to a facilitated rate of CH_3CH_2OH conversion. However, all other intermediates except CH_3CHO bind weakly on $Rh_{at}O$ single sites compared to Pt(100), leading to a higher tolerance of $Rh_{at}O$ single sites towards these species. Importantly, CO binding is found to be significantly weakened on the $Rh_{at}O$ site compared to the sites on Pt(100). Thus, consistent with the experimental observation, the DFT calculations predict that $Rh_{at}O$ sites facilitate the removal of CO formed during the reaction, enhancing the complete oxidation of ethanol.

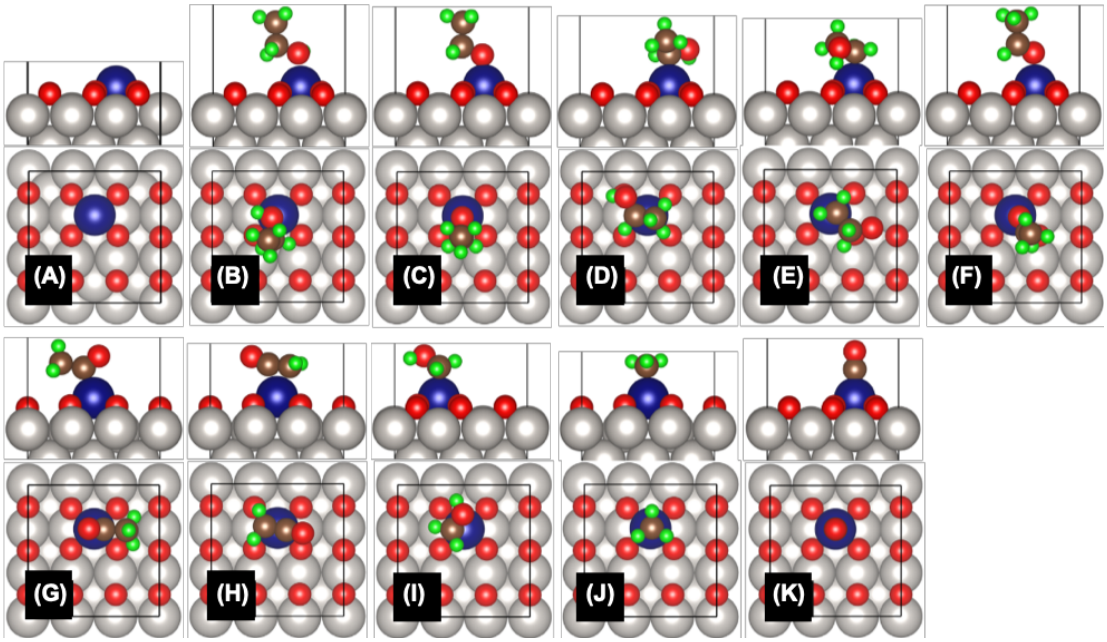

Figure 2.33 DFT optimized geometries: (A) Rh atomic sites supported on ML O covered Pt(100), (B), (C), (D), (E), (F), (G), (H), (I), (J) and (K) optimized gempetries of *CH_3CH_2OH, *CH_3CH_2O, *CH_3CHOH, *CH_2CH_2OH, *CH_3CHO, *CH_3CO, *CH_2CO, CH_2OH, *CH_3 and *CO, respectively. Pt: gray, Rh: blue, O: red, C: brown, and H: green.

Table 2.11 DFT calculated binding energies (in eV) of intermediates of ethanol electrooxidation.

Adsorbate	Pt(100)	$Rh_{at}O$-ML-Pt(100)
CH_3CH_2OH	-0.40	-0.92
CH_3CHOH	-2.46	-2.24
CH_2CH_2OH	-2.36	-2.15
CH_3CH_2O	-2.33	-2.27
CH_3CHO	-0.60	-0.94
CH_3CO	-2.76	-2.48
CH_2CO	-1.70	-1.26
CH_2OH	-2.29	-2.20

2.3.3 Conclusions

In summary, we demonstrated that the decoration of single atomic oxidized Rh on metallic Pt(100) surface notably enhanced the C-C cleavage ability to achieve completely oxidizing ethanol to CO_2. The $Rh_{at}O$-Pt NCs/C presented 11.4-fold current density of Pt/C at 0.75 V and 100% of CO_2 selectivity in a wide potential range of 0.35-0.75 V. Our studies reveal the single atomic oxidized Rh decoration could exploit the particular advantages of Pt and Rh-O: Pt as the active site to enhance EOR current density; Rh-O as the synergetic role to increase the ability to break C-C bond and assist the hydroxide adspecies formation to remove the poisoning *CO. This work fills the scientific gap of utilizing the single atom decoration on the metallic surface and promotes the understanding of single atom behavior on the metal substrate.

2.4. Acknowledgements

Chapter 2.2, in full, is a reprint of the material "Enhancing C-C Bond Scission for Efficient Ethanol Oxidation using PtIr Nanocube Electrocatalysts" as it appears in ACS Catalysis, Qiaowan Chang, Shyam Kattel, Xing Li, Zhixiu Liang, Brian M. Tackett, Steven R. Denny, Pu Zhang, Dong Su, Jingguang G. Chen, Zheng Chen, 2019, 9, 7618-7625. The dissertation author was the first author of this paper and conducted all the essential research work.

Chapter 2.3, in part is currently being prepared for submission for publication of the material. Qiaowan Chang, Youngmin Hong, Hye Jin Lee, Zhixiu Liang, Ji Hoon Lee, Ji-Eun Lim, Liang Song, Shyam Kattel, Jingguang G Chen, Zheng Chen, Sang-Il Choi. Single atomic Rh decorated Pt nanocubes promoting complete electrooxidation of ethanol. The dissertation author was the primary investigator and author of this material.

Chapter 3. Two-electron oxidation reduction reaction

Hydrogen peroxide (H_2O_2) is one of the most important chemicals[84] that is widely used in fiber and paper production, chemical synthesis, wastewater treatment, and the mining industry[85-87]. Today's anthraquinone oxidation-based industrial production of H_2O_2 needs to be improved to significantly reduce energy consumption and organic waste generation. In addition, the chemical instability of H_2O_2 poses safety issues for transportation and storage. In practice, dilute H_2O_2 solution suffices for most applications[88] (*e.g.*, < 0.1 wt. % H_2O_2 aqueous solution is used for water treatment)[89]. To enable on-demand, decentralized production of H_2O_2 using renewable electricity,[8, 88, 90-93] electrochemical H_2O_2 synthesis through a selective 2-electron ($2e^-$) oxygen reduction reaction (ORR) pathway stands out as a promising alternative route.

3.1. Introduction

3.1.1. Reaction mechanisms

Oxygen can be electrochemical reduced to H_2O_2 and H_2O via 2- and 4- electron transfer, respectively. The electrocatalyst's ability to break O-O bond determines the formed product. The O-O bond cleavage leads to the formation of *O and *OH intermediates, which further combine with H to produce H_2O. The discrepancy from the selectivity variance of electrocatalysts have not been well studied. Stephens et al.

proposed catalyst with weak binding energy of ∗O would favor the H_2O_2 production. Moreover, the activity and selectivity of metal-based catalysts are pH independence of the RHE scale. For example, Au prefers the 2-electron transfer in the acid electrolyte but 4-electron transfer in the alkaline media. Some researchers ascribed the performance difference to circumventing the *OOH formation step due to the generation of superoxide anion (O_2^-) in the base and different kinetic barriers for *OOH and * H_2O_2 dissociation.

3.1.2. Literature review of electrocatalysts

In alkaline and neutral electrolytes, defective carbon materials, such as oxidized carbon nanotubes (O-CNT) [94], B-N-doped carbon[95], Fe single-atom coordinated O-CNT[92] and reduced graphene oxide (GO)[96], have shown high activity and selectivity for the $2e^-$ ORR. For example, mildly reduced GO exhibits nearly 100% selectivity and stable activity at low overpotential (< 10 mV) in 0.1M KOH[8, 96]. It is particularly interesting to find that the selectivity of carbon materials could also be enhanced by the introduction of boron nitride (BN) islands where the active sites were attributed to the interface between hexagonal BN and graphene.[95] While these catalysts are efficient in alkaline conditions, producing H_2O_2 under acidic conditions shows technological advantage in fuel cell operation as today's proton conducting polymeric membranes are far more technologically mature than their hydroxide-conducting counterparts [88, 97]. In addition, acidic H_2O_2 solution can be directly used as an oxidant for chemical synthesis, which

contributes more than 33% to the global market share of H_2O_2 [91, 98]. Due to the weak acidic nature of the H_2O_2 molecule,[99] storing H_2O_2 in an acidic environmental can also offer a longer shelf-life compared to alkaline conditions. However, carbon-based materials require a large overpotential (~300 mV) to initiate the ORR reaction in acidic electrolytes, resulting in significant voltage loss in fuel cell operations [100-101]. For instance, the onset potential of high-selectivity mesoporous N-doped carbon was up to ~0.5 V in 0.1 M $HClO_4$, leading to a possible potential loss of 200 mV in the ORR test.[100]

Precious metals and alloys have long been investigated as electrocatalysts for $2e^-$ ORR in the acidic environment, including Au[102], Pt[103-104], Pd-Au[105-106], Pt-Hg[90], Ag-Hg[8] and Pd-Hg[8]. So far Pd-Hg core-shell nanoparticles represent the most active catalysts in the acidic environment. Benefiting from its optimal HOO* binding energy, core-shell Pd-Hg has been reported to show 5 times higher mass activity (~130 A g^{-1}) than polycrystalline Pt-Hg/C (~ 25 A g^{-1}) (0.65 V versus reversible hydrogen electrode or RHE, all the potential values are refereed to RHE unless specified) with selectivity up to 95% between 0.35 and 0.55 V[8]. However, the high toxicity of Hg might hinder its industrial application. Fe-N-C[107] and Co-N-C[108] are considered as more cost-effective catalysts, but their selectivity needs to be significantly improved.

3.2. Coordinating partially oxidized Pd with defect carbon

3.2.1. Experimental

3.2.1.1. Electrocatalysts synthesis

To prepare oxidized carbon nanotubes (O-CNTs) with different density of defects and functional groups, 250 mg of multi-walled CNTs (produced by a tons-scale fluidized chemical vapor deposition process)[109] was refluxed in 20 ml of HNO_3 (Fisher Scientific, 68 wt. %) for 2.5h, 4.5h, 6.5h or 8.5h at 140 °C. The resulting product was obtained after centrifugal separation and drying at 55 °C. A simple impregnation method was used to prepare Pd supported by OCNTs ($Pd^{\delta+}$-OCNT). Specifically, 2.5 mg of $PdCl_2$ (Alfa Aesar, 99.9%) and 50 mg of OCNT were suspended in 20 ml of 7 wt.% HNO_3 solution and heated at 65 °C with vigorous stirring until the mixture was fully dried. To anneal the $Pd^{\delta+}$-OCNT, the as-prepared sample was heated from room temperature to 100 °C at a rate of 10 °C min^{-1} and kept at 100 °C for 1h under argon (Ar) protection before ramping to 450 °C at a rate of 4 °C min^{-1}. Then it was annealed for 5 h at this temperature to obtain thermally annealed sample (H-Pd-OCNT).

3.2.1.2. Characterization

The defect formation process and distribution Pd clusters of different samples were characterized by HAADF-STEM (Hitachi HD 2700C). EDS was performed by FEI Talos F200X to obtain element distributions of Pd on each sample. The structure and

phase composition were further characterized by X-ray diffractometer (XRD, Bruker AXS) equipped with a Cu Kα radiation source (λ=1.5406 Å). The specific mass loading of the Pd atomic clusters was determined by ICP-MS (iCAP Qc, Thermo Fisher Scientific). To investigate the heteroatoms and functional groups, a commercial SPECS Ambient-pressure X-ray photoelectron spectrum (AP-XPS) chamber combined with a PHOIBOS 150 EP MCD-9 analyzer and Fourier-transform infrared spectroscopy (FTIR, Nicolet iS50) were used. The Raman spectra were acquired by a Renishaw inVia with 532 nm laser source. Nitrogen adsorption/desorption were conducted by an autosorb iQ2.

3.2.1.3. Electrochemical measurements

Electrochemical test was performed in three-electrode cells, where a graphite and Ag/AgCl (3M Cl^-) were used as the counter electrode and reference electrode, respectively. The electrocatalyst inks were prepared by dispersing samples in a Milli-Q and isopropanol solution (4:1) with 10 µl of Nafion (5%) to achieve the mass concentration of 1 mg ml^{-1} for $Pd^{\delta+}$-OCNT and H-Pd-OCNT samples, 3.5 mg ml^{-1} for O-CNT samples. 10 µl of each catalyst ink was then deposited on a pre-cleaned glassy carbon (GC) electrode (0.196 cm^{-2}). The CV curves were recorded in Ar-saturated 0.1 M $HClO_4$ electrolyte with a scanning rate of 50 mV s^{-1}. The ORR performance was examined by rotating disk electrode (RDE) and rotating ring disk electrode (RRDE) in an O_2-saturated 0.1 M $HClO_4$ solution at a scanning rate of 10 mV s^{-1} with capacity current correction (in Ar-saturated 0.1 M $HClO_4$).

The ring current was hold at 1.2 V (vs. RHE) to further oxidize the as-formed H_2O_2 and collection efficiency was calibrated to be 0.37. The stability test was performed by CA test at 0.1 V for 30000 s. The selectivity was calculated by previous report[88, 91], detailed below.

The H_2O_2 selectivity of samples based on RDE was calculated by Koutecky−Levich (*K-L*) plot in Equation (**Eq. 3.1-2**) from the polarization curves at different rotation speeds.

$$\frac{1}{j} = \frac{1}{j_{kin}} + \frac{1}{j_{diff}} = \frac{1}{j_{kin}} + \frac{1}{B \cdot \sqrt{\omega}}$$

(**Eq. 3.1**)

$$B = 0.62 \cdot n \cdot F \cdot D_{O_2}^{2/3} \cdot \nu^{-1/6} \cdot C_{o_2}$$

(**Eq. 3.2**)

where j is the current density consists of a kinetic current (j_{kin}) and a diffusion current (j_{diff}), ω is the rotation speed, n is the number of electrons transferred during the reaction, and D_{o_2} and C_{o_2} are the diffusivity and solubility of oxygen, respectively; F is the Faraday constant, and ν is the kinematic viscosity of the electrolyte. For a $4e^-$ process, B = 0.47 mA cm^{-2} $s^{1/2}$, and for a 2e- process, B = 0.23 mA cm^{-2} $s^{1/2}$.[100] For RRDE tests, the H_2O_2 selectivity was calculated by Equation 3.3.

$$H_2O_2(\%) = 200 * \frac{I_R/N}{I_D + I_R/N}$$

(**Eq. 3.3**)

where I_R and I_D are the ring current and disk current, respectively; and N is the collection efficiency.

To further confirm the selectivity of the $Pd^{\delta+}$-OCNT electrocatalyst, a H-cell with a Nafion 117 membrane was used. Electrocatalysts were loaded on Telfon-treated carbon papers (0.1 mg cm^{-2}). The concentration of generated H_2O_2 was measured by its reaction with $Ce(SO_4)_2$ ($2Ce^{4+} + H_2O_2 \rightarrow 2Ce^{3+} + 2H^+ + O_2$). The color of solution changes from yellow to colorless through the reaction. The concentration of Ce^{4+} after the reaction was measured by ultraviolet–visible spectroscopy (UV-VIS, Perkin Elmer UV-VIS-NIR Spectrometer) with 316 nm of wavelength.

3.2.1.4. XAFS measurements

XAFS measurements were conducted in the 7-BM beamline (QAS) at National Synchrotron Light Source-II (NSLS-II) at Brookhaven National Laboratory. Both transmission and fluorescent signals were detected. The typical duration for a single spectrum was 47 sec and thirty spectra were merged to get high signal-to-noise spectrum at each potential. During all of the XAFS measurements, the spectrum of reference Pd foil was simultaneously recorded, and was further used for calibrating the edge energy (E_0) of the sample under analysis.

The obtained spectra were processed using the ATHENA and ARTEMIS software in IFFEFIT package[71-72, 110]. The procedure which was described in B. Ravel et al.[71], was followed during the data process[110]. EXAFS analyses were conducted by using the ARTEMIS software. The EXAFS spectrum ($\chi(k)$) was weighted with k^2 value to intensify

the signal at high k-regime. The Hanning window was utilized for the Fourier-transform. All of the EXAFS fitting was done in the *R*-space. The goodness of fitting was evaluated based on the reliable factor (R-factor) and reduced chi-square (reduced χ^2).

3.2.1.5. DFT calculations

Atomic Simulation Environment (ASE)[111] was used to handle the simulation and the QUANTUM ESPRESSO[112] program package to perform electronic structure calculations. The electronic wavefunctions were expanded in plane waves up to a cutoff energy of 500 eV, while the electron density is represented on a grid with an energy cutoff of 5000 eV. Figure S35 displays the energy cutoff convergency plots for calculated adsorption energies and limiting potentials for an example of our model calculations (Pd_2 cluster). Core electrons were approximated using ultrasoft pseudopotentials.[113] To describe chemisorption properties on graphene structures, PBE exchange-correlation functional with dispersion correction was used.[114] Graphene structures were modeled as one layer with a vacuum of 20 Å to decouple the periodic replicas. A 5 × 5 super cell lateral size was used to model Pd_1 and Pd_2 clusters and the Brillouin zone was sampled with (4 × 4 × 1) Monkhorst-Pack k-points. For the larger clusters of Pd_3 and Pd_4 we used a 7 × 7 super cell lateral size with (2 × 2 × 1) Monkhorst-Pack k-points sampling. Figure S36 displays the k-point sampling convergency plots for the calculated adsorption

energies and limiting potentials for an example of our model calculations (Pd_3 cluster covered with 3O* and 1HO*).

3.2.2. Results and discussions

OCNTs were chose as a substrate to explore the potential active sites of defect carbons for acidic H_2O_2 synthesis, due to their superior selectivity and activity demonstrated in alkaline electrolytes. As the ORR overpotential was identified to be too high in acidic electrolytes[100-101], this chapter first focused on understanding and optimizing the effect of compositional and structural defects on their $2e^-$ ORR selectivity with the aim to create a functional support that can be used to integrate a second motif that may significantly improve the overall $2e^-$ ORR activity.

CNTs were oxidized under different time durations from 2.5 h to 8.5 h in a nitric acid solution to tune the amounts and types of defects. TEM images (**Figure 3.1**) show that the density of defect sites increased with longer oxidation time. When reacted for 6.5 h, abundant defect sites were clearly observed from the changes of the surface roughness and curvature at the OCNTs, suggesting that the bended regions of CNTs were more easily oxidized due to the higher strain than the straight tube walls[115]. After 8.5 h of oxidation, thinner OCNTs with smooth surfaces were observed, which was likely due to the complete etching of the outer-walls of OCNT, a phenomenon also reported by Su *et.al*[116]. Under all the explored oxidation conditions, tubular nanostructure and crystallinity were maintained

as suggested by both TEM and XRD (**Figure 3.2**). Such a defect formation process was also confirmed by the increased intensity ratios of their *D* and *G* bands (I_D/I_G) in the Raman spectra (**Figure 3.3**), changes of surface area (**Figure 3.4 and 3.5**) and the mass loss of the CNTs (**Figure 3.6**). Also, the strong signal from the *D′* band implied the existence of basal plane sp^2 carbon oxidization sites in the OCNT [117].

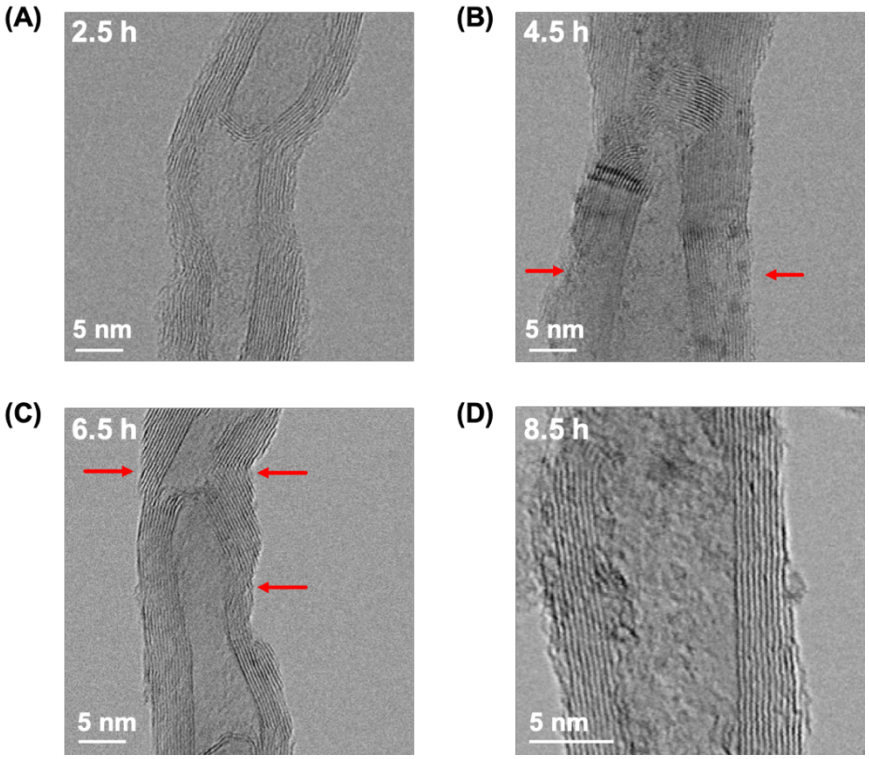

Figure 3.1 HRTEM image of obtained OCNT for different reaction time.

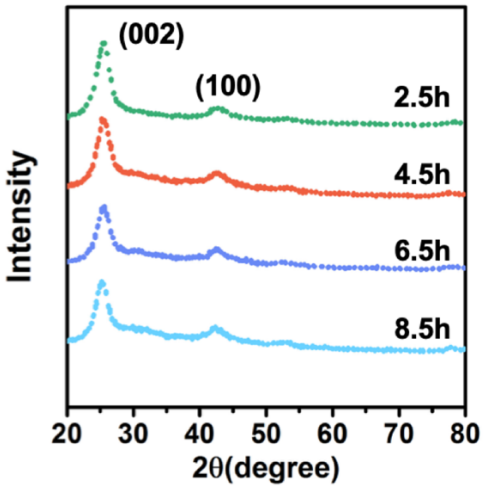

Figure 3.2 XRD patterns of obtained OCNT samples with different durations of oxidation time.

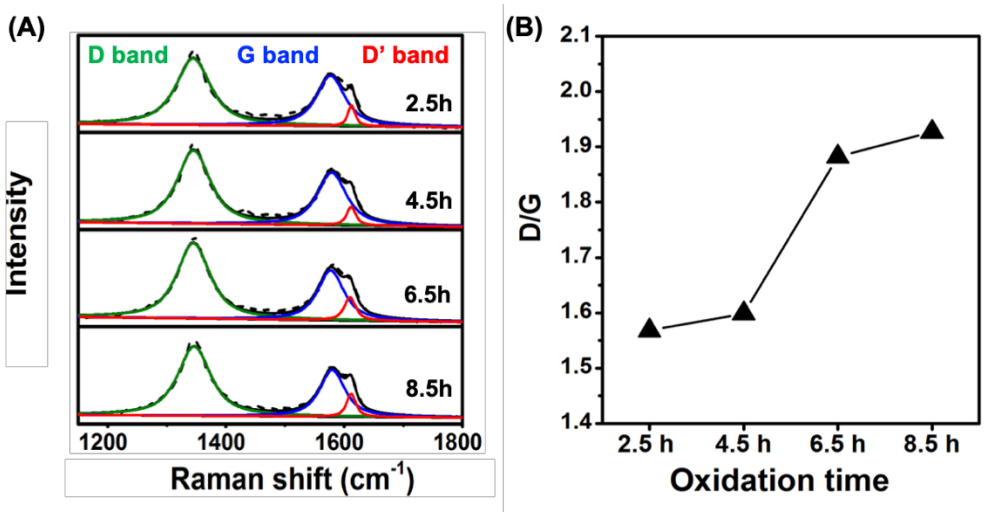

Figure 3.3 (A) Raman spectra and (B) calculated I_D/I_G ratios of different OCNT samples.

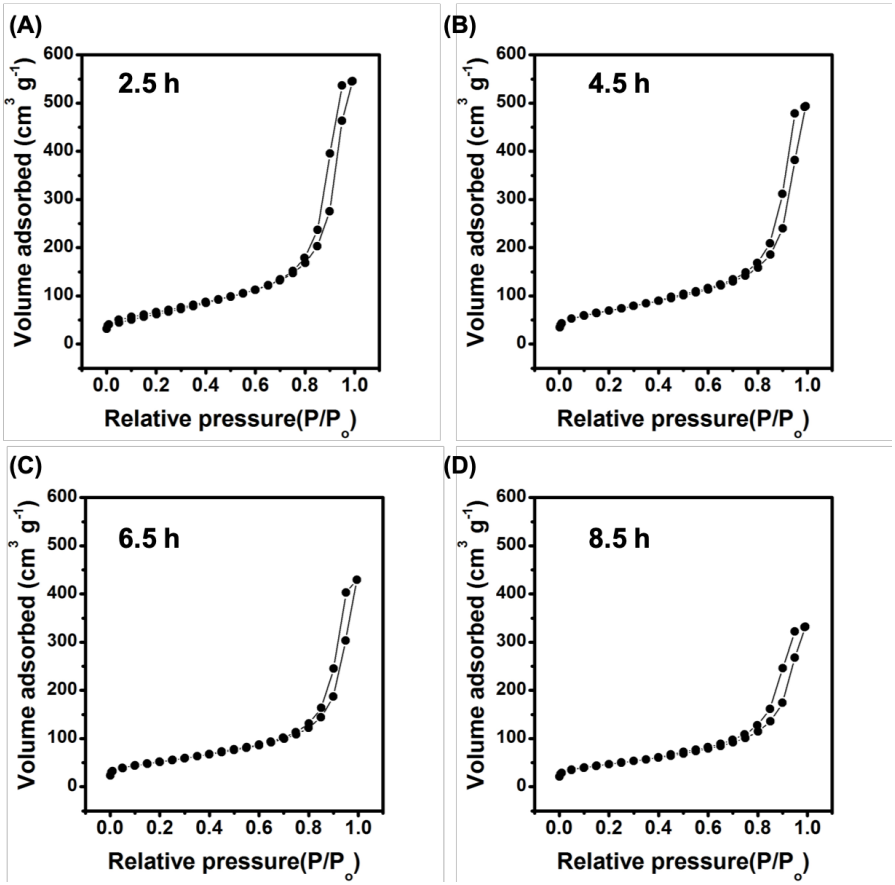

Figure 3.4 The N_2 adsorption-desorption isotherms of OCNT samples.

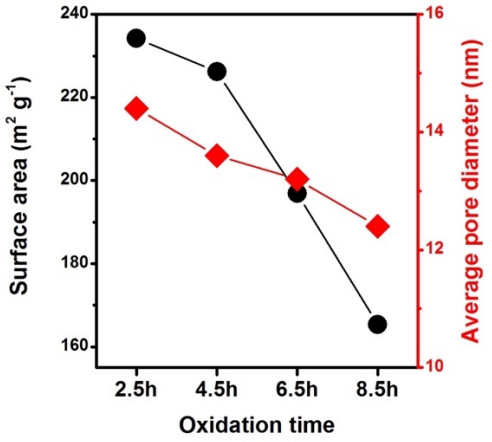

Figure 3.5 Calculated surface area and average pore diameter from N_2 adsorption-desorption isotherms of OCNT samples.

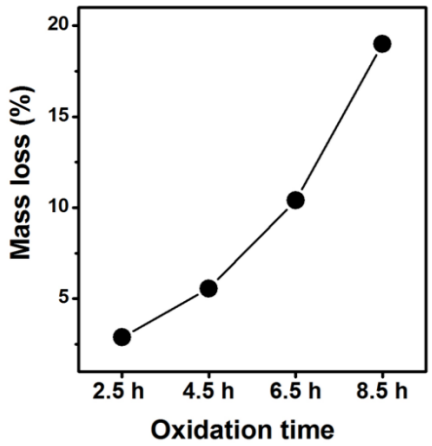

Figure 3.6 Recorded mass loss percentages during the preparation of OCNT samples.

The oxidation process also introduced defects and functional groups on the surface of OCNTs. Fourier-transform infrared spectroscopy (FTIR) measurements not only confirmed the existence of defects ($-CH_3$) in the samples, but also revealed that the functional groups were mainly C-O and C=O (**Figure 3.7**), which were further quantified by X-ray photoelectron spectroscopy (XPS, **Figure 3.8**). With increased oxidation time from 2.5 to 6.5 h, the percentages of C=C (sp^2 carbon) decreased rapidly while the C-O group as the major component of oxygen-containing functional groups increased from 20.1% to 34.6% (on the C basis). Further extending the oxidation time to 8.5 h led to negligible change of C=C groups but a decrease of C-O ratio by ~5%. At the same time, the density of the C-C (structure defects with the form of sp^3 carbon) group increased from 4.9% to 11.1% while that of the C=O groups remained at ~5% during the entire oxidation time.

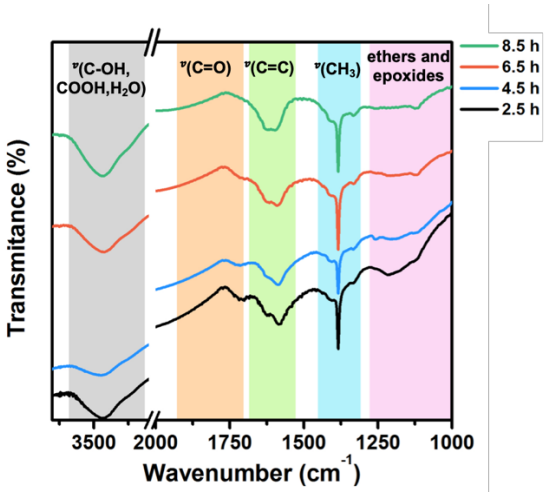

Figure 3.7 FTIR spectra of OCNTs prepared from 2.5 h to 8.5 h.

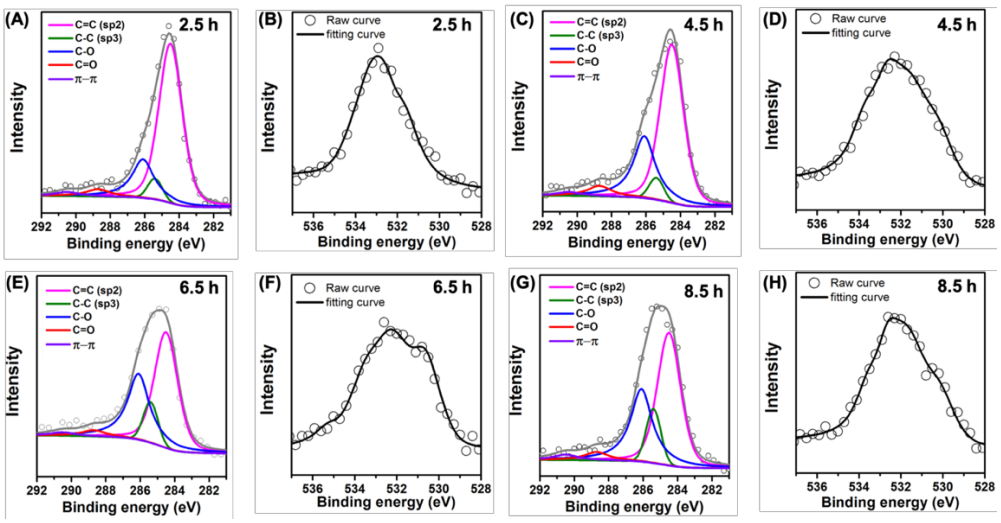

Figure 3.8 (A, E, C, G) Deconvoluted carbon 1s spectra and (B, F, D, H) obtained oxygen 1s spectra of OCNTs.

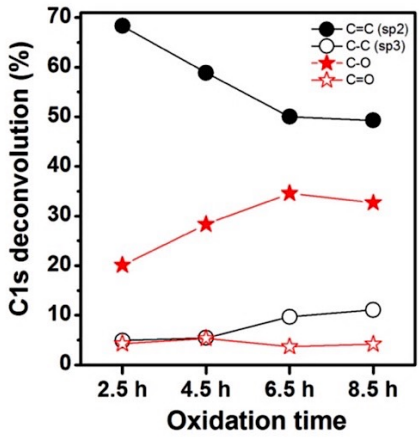

Figure 3.9 Deconvoluted carbon 1s peak result of OCNTs reacted from 2.5 h to 8.5 h.

To correlate the defect characteristics with electrochemical properties, the OCNTs were examined in 0.1M $HClO_4$ by CV, RDE and RRDE. As shown in the CV curves (**Figure 3.10A**), the pseudocapacitive current (represented by the redox peaks between 0.2 and 0.8 V) of the OCNT electrodes first increased as the oxidation time extended from 2.5 to 6.5 h and then maintained roughly the same from 6.5 to 8.5 h. The trend of capacitance changes from the redox current was similar with that of the relatively ratios of the C-O groups on the surface from the XPS results (**Figure 3.10B**), suggesting that redox peaks could be attributed to the oxidation/reduction of surface quinoidal functional group[118]. All the OCNTs presented a similar onset potential (~ 0.38 V) to initiate the $2e^-$ ORR. From both the RDE and RRDE tests, OCNTs obtained after 6.5 h oxidation presented the highest H_2O_2 selectivity among all the OCNTs, with 95% at 0.1 V through the Koutecky-Levich (K-L) calculation and 90%-92% in the range of 0.25 V to 0.35 V from the RRDE measurement (**Figure 3.11**). It was previously shown that a higher oxygen

content in OCNTs resulted in a higher selectivity for H_2O_2 in the alkaline medium[94]. In the acidic electrolyte, we found that both the defects and oxygen-containing groups played important roles in determining the $2e^-$ ORR selectivity (**Figure 3.12**). For example, when the defect ratio (calculated from deconvoluted C1s XPS peak) increased from 9.7% (6.5 h-OCNT) to 11.1% (8.5 h-OCNT) with a similar number of C-O groups, the H_2O_2 selectivity decreased from 90% to 78% at 0.25 V (**Figure 3.13**). This result indicated that the defect sites might present strong binding with OH* and O*, leading to more preferred $4e^-$ ORR competing process to produce H_2O [6, 119].

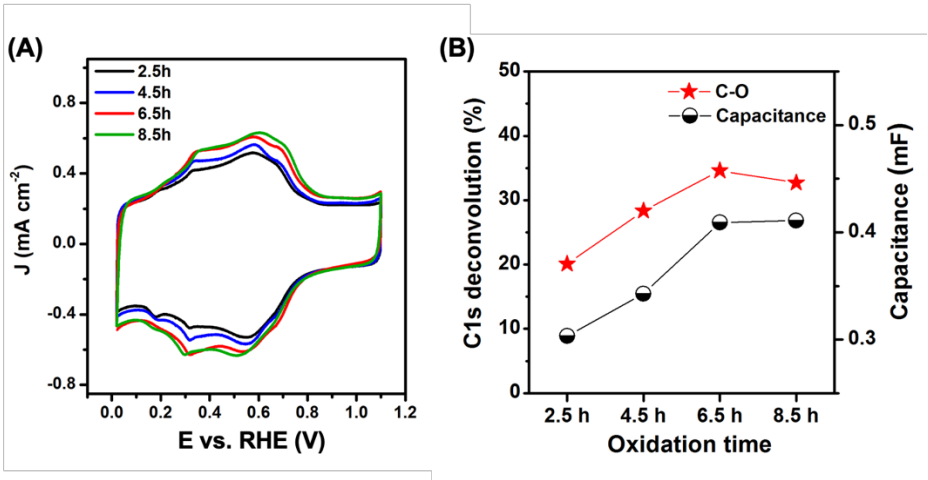

Figure 3.10 (A) Cyclic voltammogram curves of OCNT samples in Ar-saturatred 0.1 M $HClO_4$ with a scan rate of 50 mV s^{-1}. (B) Calculated relative ratios of C-O groups and the capacitance of redox peaks from CV for different OCNT samples.

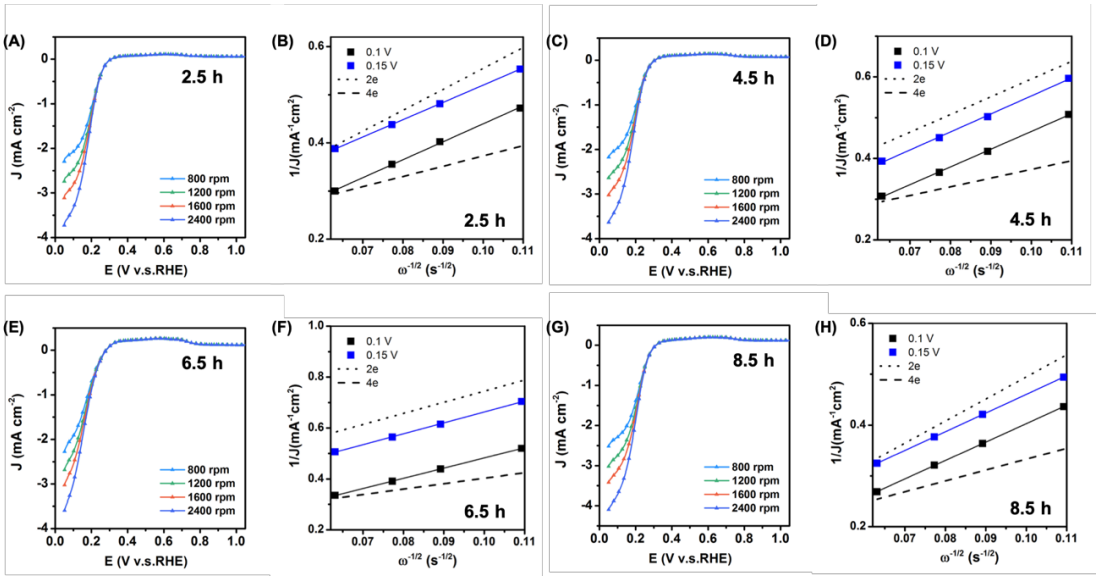

Figure 3.11 (A, C, E, G) Polarization curves at various rotation rates in oxygen-saturated 0.1 M $HClO_4$ of and (B, D, F, H) Koutecky−Levich plot for the calculation of the transfer electron numbers of OCNTs. All the currents were normalized to the geometrical area of rotating disk electrode.

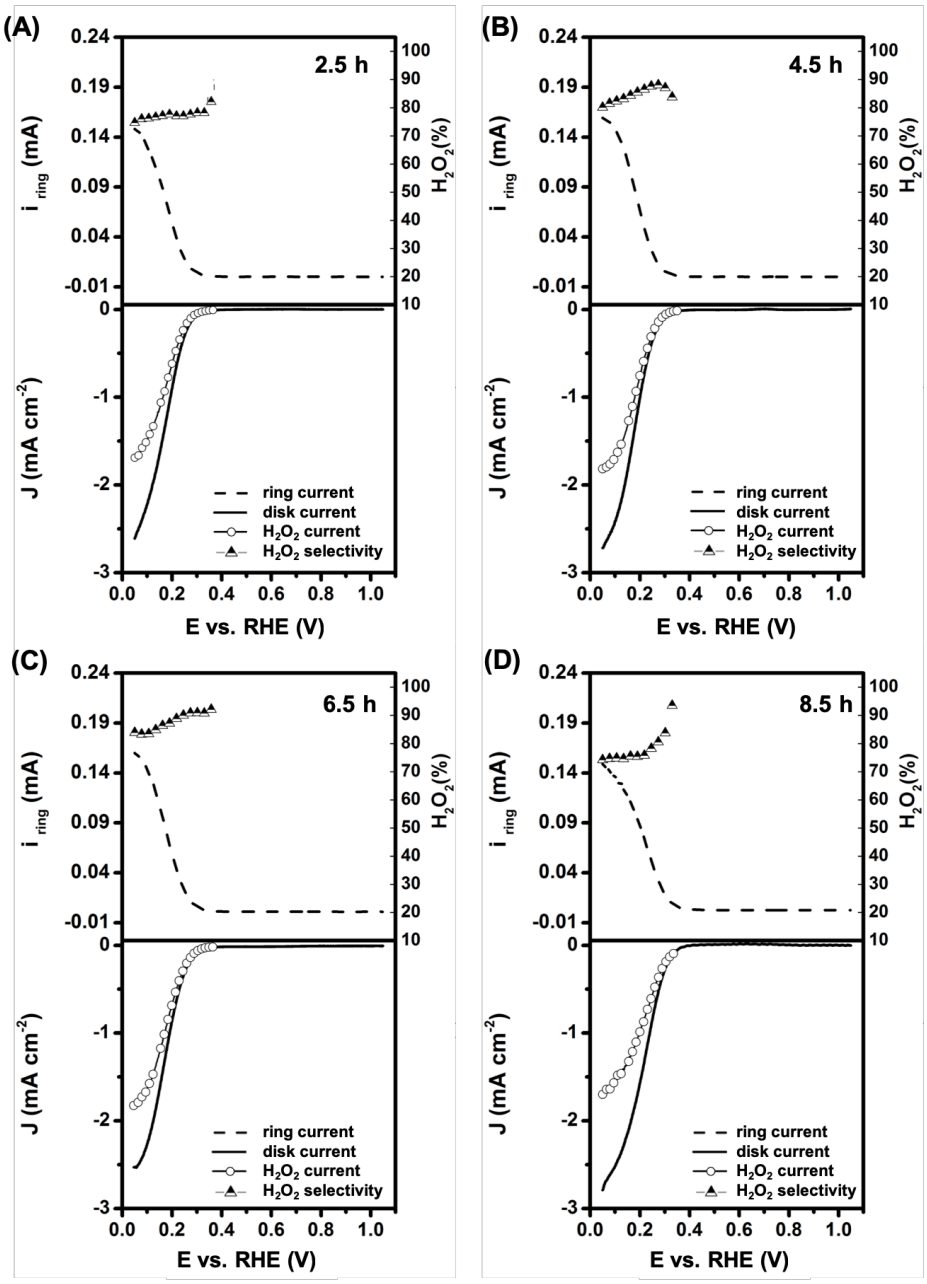

Figure 3.12 RRDE voltammograms in O_2-saturated $HClO_4$ electrolyte with a scan rate of 10 mV s^{-1} at 1600 rpm (only the anodic cycle is shown). The disc current, ring current, hydrogen peroxide current calculated from the ring current and selectivity during the reaction of OCNT samples.

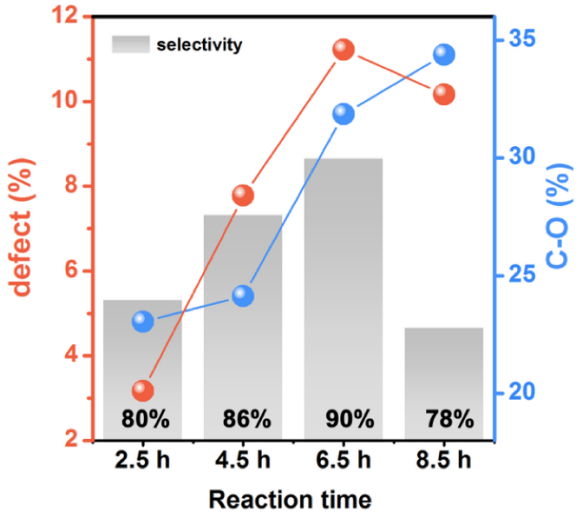

Figure 3.13 Summary of the relationship between the ratios of defects, C-O groups in OCNT samples reacted from 2.5 h to 8.5 h and its selectivity toward $2e^-$ ORR.

$Pd^{\delta+}$-OCNT electrocatalysts composed of Pd clusters (Pd_3 and Pd_4) supported on OCNTs were prepared by loading ~1.0 wt.% of Pd on OCNTs with 6.5h oxidation, which was identified to be the best substrate. After Pd deposition, Pd clusters were obtained since no crystalline Pd lattice was detected in the high-resolution TEM (HRTEM) image (**Figure 3.14A**). The Pd clusters were distributed uniformly with a narrow size range of 0.61± 0.07 nm on OCNTs (**Figure 3.14B-D**). However, with mild thermal annealing (450 ^oC for 5h) (sample named as H-Pd-OCNT), Pd nanoparticles (3~10 nm) were formed (**Figure 3.14E-F**). XRD patterns clearly show the amorphous nature of the as-deposited Pd in the $Pd^{\delta+}$-OCNT and high crystallinity of Pd in the H-Pd-OCNT sample (**Figure 3.15A**).

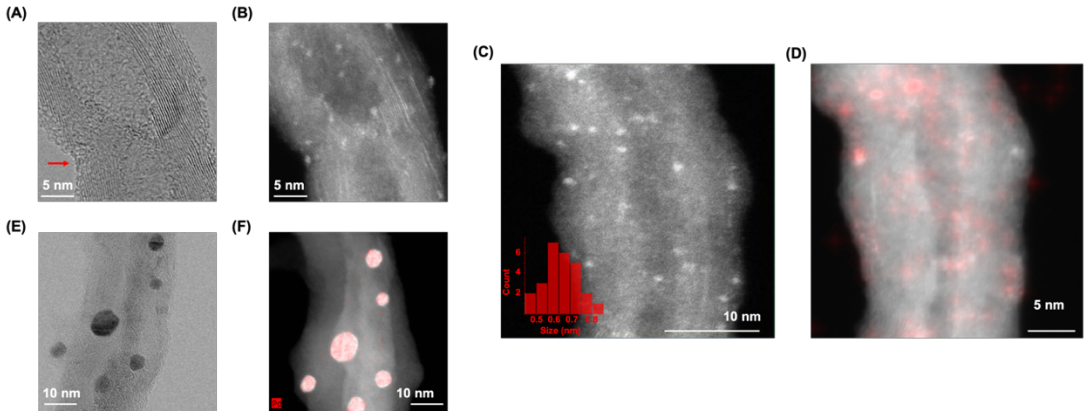

Figure 3.14 Structural characterization of $Pd^{\delta+}$-OCNT and H-Pd-OCNT electrocatalysts. (A) HRTEM, (B ,C) annular dark-field (ADF)-STEM image, and (D) EDS Pd element mapping of $Pd^{\delta+}$-OCNT presenting uniform distribution of amorphous Pd atom clusters. Inset figure shows the size distribution of the Pd clusters. (E) HRTEM and (F) EDS element mapping of H-Pd-OCNT shows the formation of aggregated crystalline Pd nanoparticles with size of 3~10 nm.

The binding environments of $Pd^{\delta+}$-OCNT and H-Pd-OCNT were further characterized using extended X-ray absorption fine structure (EXAFS, **Figure 3.15B-C**, and Table 4.1-4). The coordination number (CN) of Pd-Pd and Pd-O in $Pd^{\delta+}$-OCNT was found to be 2.5 and 2.7, respectively, suggesting that Pd was coordinated to both Pd and O in the small clusters, and the Pd clusters were partially oxidized. In contrast, the H-Pd-OCNT sample was characterized by a Pd-Pd CN of 7.9, which represented a larger metallic Pd particle (> 3nm) and was consistent with the TEM results.

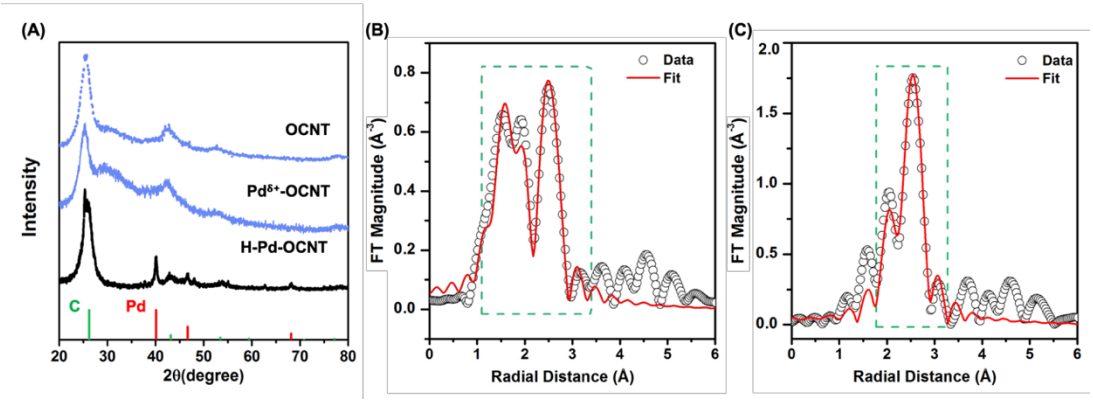

Figure 3.15 (A) Powder XRD patterns of 6.5 h OCNT, Pd$^{\delta+}$-OCNT and H-Pd-OCNT. (B) Fourier transform EXAFS analysis of Pd K-edge data for Pd$^{\delta+}$-OCNT and (C) H-Pd-OCNT.

Table 3.1 EXAFS fitting results.

Parameter	Entry		
	Pd Metal	H-Pd-OCNT	Pd$^{\delta+}$-OCNT
Independent Points	12.9267578	8.7089844	13.296875
Number of Variables	4	4	7
Reduced Chi-square	2185.0284425	523.9641474	126.9657377
R-factor	0.0042065	0.0138021	0.0270848
k-range (Å^{-1})	3.000 – 13.931	2.488 – 11.601	2.015 – 11.296
R-range (Å)	1.3 – 3.2	1.761 – 3.3	1.1 – 3.4
Number of Data Set	1	1	1
Structure Model 1			
Chemical Fomula	Pd		
Space Group	Fm-3m		
Lattice Constant	3.900 Å		
Structure Model 2			
Chemical Fomula	PdO		
Space Group	P4$_2$/mmc		
Lattice Constant	a=b=3.096 Å, c=5.442 Å		

Table 3.2 EXAFS fitting parameter of Pd metal.

Path	Coordination Number [a]	E_0 (eV)	R (Å)	σ^2 (Å^2)	Remarks
Pd-Pd	12	3.4(3)	2.733(6)	0.0055(2)	Pd

[a] Amplitude reduction factor was attained from this fitting. All the fitting was done in R-space

Table 3.3 EXAFS fitting parameter of H-Pd-OCNT.

Path	Coordination Number [a]	E_0 (eV)	R (Å)	σ^2 (Å^2)	Remarks
Pd-Pd	7.3(9)	2.4(8)	2.733(6)	0.0058(9)	Pd

[a] Amplitude reduction factor was attained from the reference Pd metal foil. All the fitting was done in R-space

Table 3.4 EXAFS fitting parameter of $Pd^{\delta+}$-OCNT.

Path	Coordination Number [a]	E_0 (eV)	R (Å)	σ^2 (Å^2)	Remarks
Pd-Pd	2.5(6)	0.29 [b]	2.743(6)	0.004(2)	Pd
Pd-O	2.7(4)	10(1)	2.11(2)	0.008(4)	PdO

[a] Amplitude reduction factor was attained from the reference Pd metal foil. All the fitting was done in R-space

[b] Fixed during the fitting.

After deposition of Pd clusters, the surface properties of different samples were further compared. The I_D/I_G ratio in the Raman spectra (**Figure 3.16A**) was 1.82 and 1.71 for $Pd^{\delta+}$-OCNT and H-Pd-OCNT, respectively, showing negligible changes of defects after Pd deposition and heat treatment as compared with the OCNT (I_D/I_G =1.88). Also, the basal plane sp^2 carbon oxidization sites still remained in both $Pd^{\delta+}$-OCNT and H-Pd-OCNT as shown by the D' band. FTIR results indicated that the types of surface

functional groups (C=O, C-O) were maintained after Pd deposition and annealing (**Figure 3.16B**). XPS results also showed similar abundancy of sp^3 carbon defects, C-O and C=O with OCNTs, further suggesting that the deposition of Pd clusters did not change the surface properties of the OCNTs (**Figure 3.17**). For H-Pd-OCNT, the ratio of sp^3 carbon defects and C-O group decreased with an increase of C=C ratio, likely due to the cleavage of less thermally stable functional groups under annealing[120]. Table 4.5Such a catalyst structure allows us to further identify the unique role of the partially oxidized Pd clusters in catalyzing the $2e^-$ ORR by isolating the effect of Pd and the defect carbon substrates.

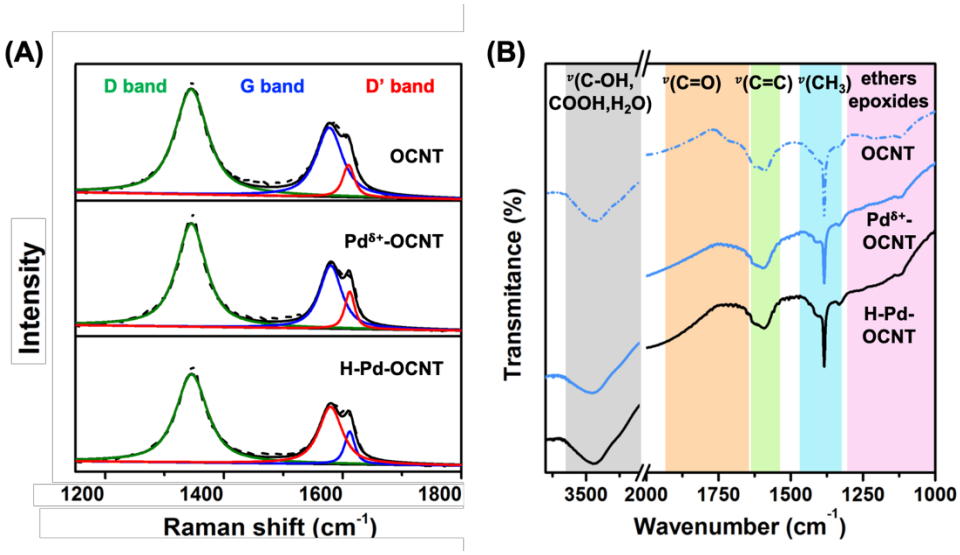

Figure 3.16 (A) Raman spectra and (B) FTIR spectra of 6.5 h OCNT, Pd$^{\delta+}$-OCNT and H-Pd-OCNT.

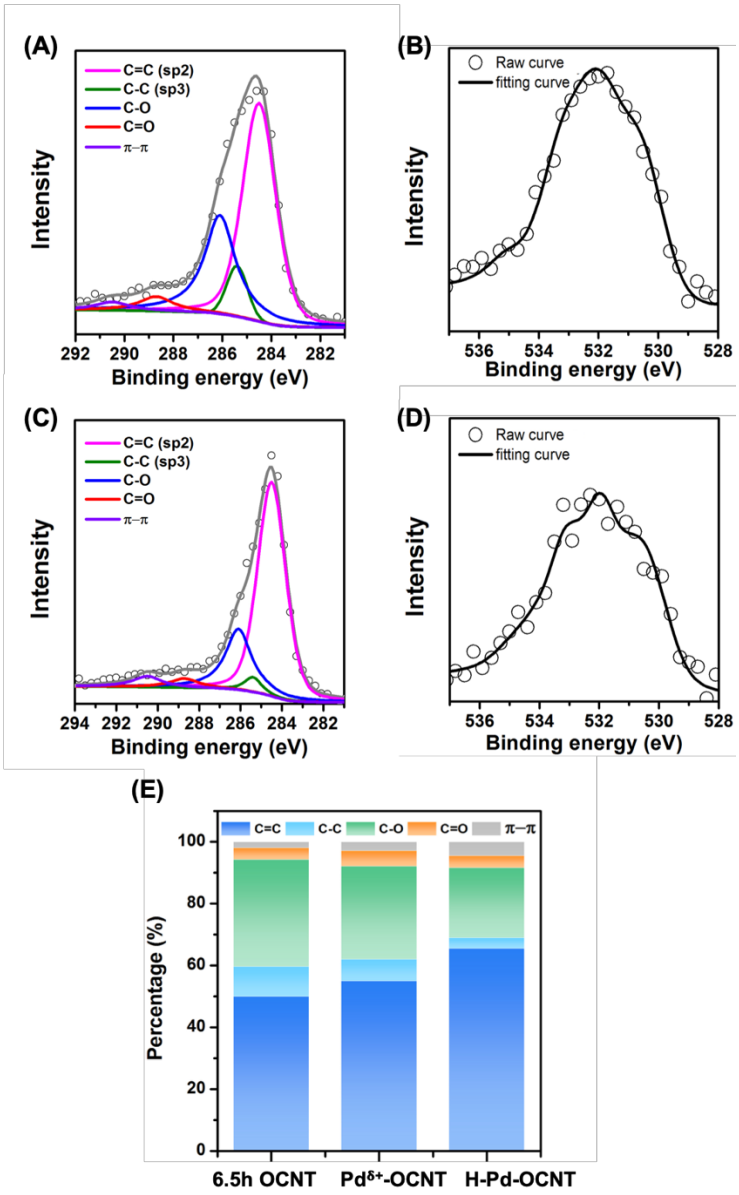

Figure 3.17 (A) Deconvoluted carbon 1s and (B) oxygen 1s spectra of $Pd^{\delta+}$-OCNT. (C) Deconvoluted carbon 1s and (D) oxygen 1s spectra of H-Pd-OCNT. (E) The distribution of carbon element in different coordination environments for 6.5 h OCNT, $Pd^{\delta+}$-OCNT and H-Pd-OCNT measured by C1s XPS.

The effect of Pd clusters on the H_2O_2 selectivity and activity was investigated by comparing $Pd^{\delta+}$-OCNT with OCNT and H-Pd-OCNT. The characteristic hydrogen

adsorption/desorption peaks of Pd in both $Pd^{\delta+}$-OCNT and H-Pd-OCNT electrocatalysts were observed in the CV curves (**Figure 3.18A**), confirming the successful loading of Pd onto the OCNT surface. The most interesting feature for the $Pd^{\delta+}$-OCNT catalyst was observed in the ORR process (**Figure 3.18B**). After the introduction of Pd clusters, both the ring and disc currents of $Pd^{\delta+}$-OCNT initiated earlier than that of OCNT, resulting in a positive shift of ORR onset potential by ~ 320 mV. The H_2O_2 current of the $Pd^{\delta+}$-OCNT electrocatalyst nearly overlapped with total reaction (disc) current, which suggested that the ORR almost exclusively proceeded toward the $2e^-$ pathway. The calculated H_2O_2 selectivity of the $Pd^{\delta+}$-OCNT catalyst was in the range of 98% to 95% in the potential range of 0.7 to 0.3 V, superior to precious metal-based electrocatalysts reported previously [8, 90, 103-104, 106]. More importantly, the kinetic mass activity of $Pd^{\delta+}$-OCNT for H_2O_2 production reached 1.946 A mg^{-1} at 0.45 V, about 1.5 times of the core-shell Pd_2Hg_5/C catalyst [8] and significantly higher than that of other electrocatalysts in acidic electrolytes (**Figure 3.18C**) [8, 90, 96, 101, 105, 121-122]. As for the H-Pd-OCNT catalyst, although it showed a similar positive shift in onset potential as $Pd^{\delta+}$-OCNT, it preferred the $4e^-$ ORR pathway to completely reduce O_2 to H_2O, showing only 18% of H_2O_2 selectivity at 0.1 V. Thus, we conclude that the partially oxidized Pd clusters are the key in enhancing activity and maintaining high selectivity for H_2O_2 production.

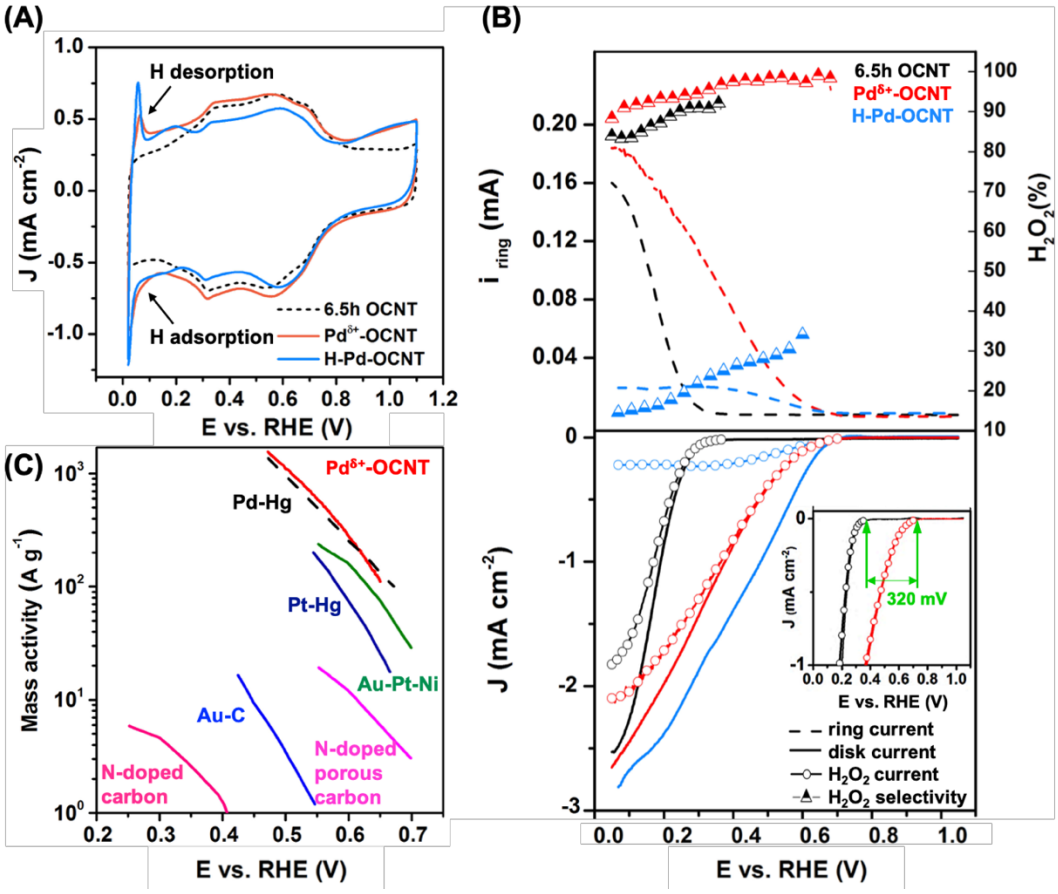

Figure 3.18 Electrochemical performance of $Pd^{\delta+}$-OCNT and H-Pd-OCNT catalysts. (A) CV curves of different electrocatalysts (B) RRDE voltammograms in O_2-saturated $HClO_4$ electrolyte with a scan rate of 10 mV s^{-1} at 1600 rpm (only the anodic cycle is shown). (C) Mass activity of the state-of-the-art electrocatalysts for H_2O_2 production in the acid electrolyte. Data were taken from previous reports. [8, 90, 96, 101, 105, 121-122]

To demonstrate their viability for continuous ORR in fuel cell operations, we deposited the $Pd^{\delta+}$-OCNT electrocatalysts on carbon paper as a working electrode and fabricated a device that could synthesize H_2O_2 directly in acidic electrolyte (**Figure 3.19**). In such a device, O_2 was reduced to yield H_2O_2 directly by combining with the protons in the acidic electrolyte without the need of molecular H_2. The amount of H_2O_2 generated in

an H-cell was obtained by a titration method. When the catalyst mass loading was controlled to 0.1 mg cm^{-2}, a steady current density of 10 mA cm^{-2} was recorded at 0.1 V (**Figure 3.20A**). The selectivity of H_2O_2 was measured to be 87%, which was close to the RRDE test at 0.1 V. Also, the yield of H_2O_2 was up to 1701 $molkg_{cat}^{-1}$ h^{-1}, 2 times higher than that of the single atomic Pt electrocatalyst reported recently.[123] The ORR stability of $Pd^{\delta+}$-OCNT was evaluated by CA test by holding the disk electrode potential at 0.1 V for more than 8 hr. Both the disc and ring currents decreased by only ~15% after the test and the H_2O_2 selectivity was still maintained at 86% (**Figure 3.20B**). It was found that the morphology and size distribution of Pd clusters on OCNTs showed negligible changes after the stability test (**Figure 3.20C and D**), which was responsible for their good electrochemical stability during the ORR.

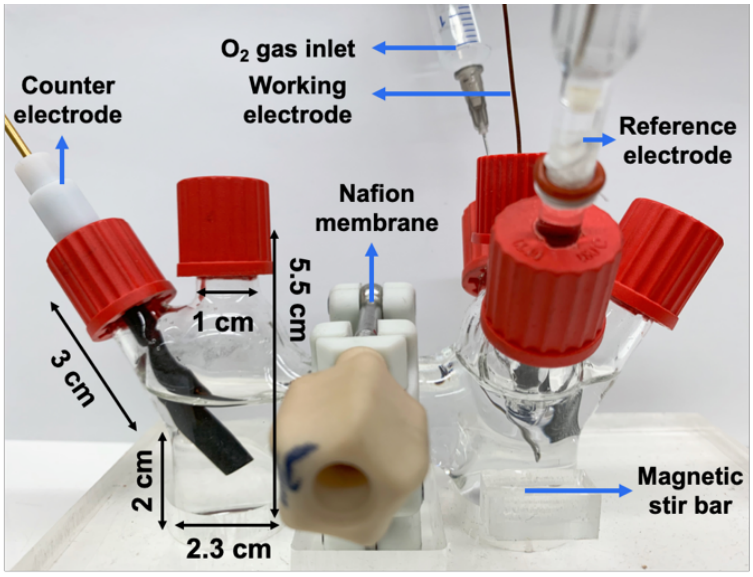

Figure 3.19 The digital photo image of the H-cell used for the H_2O_2 yield test.

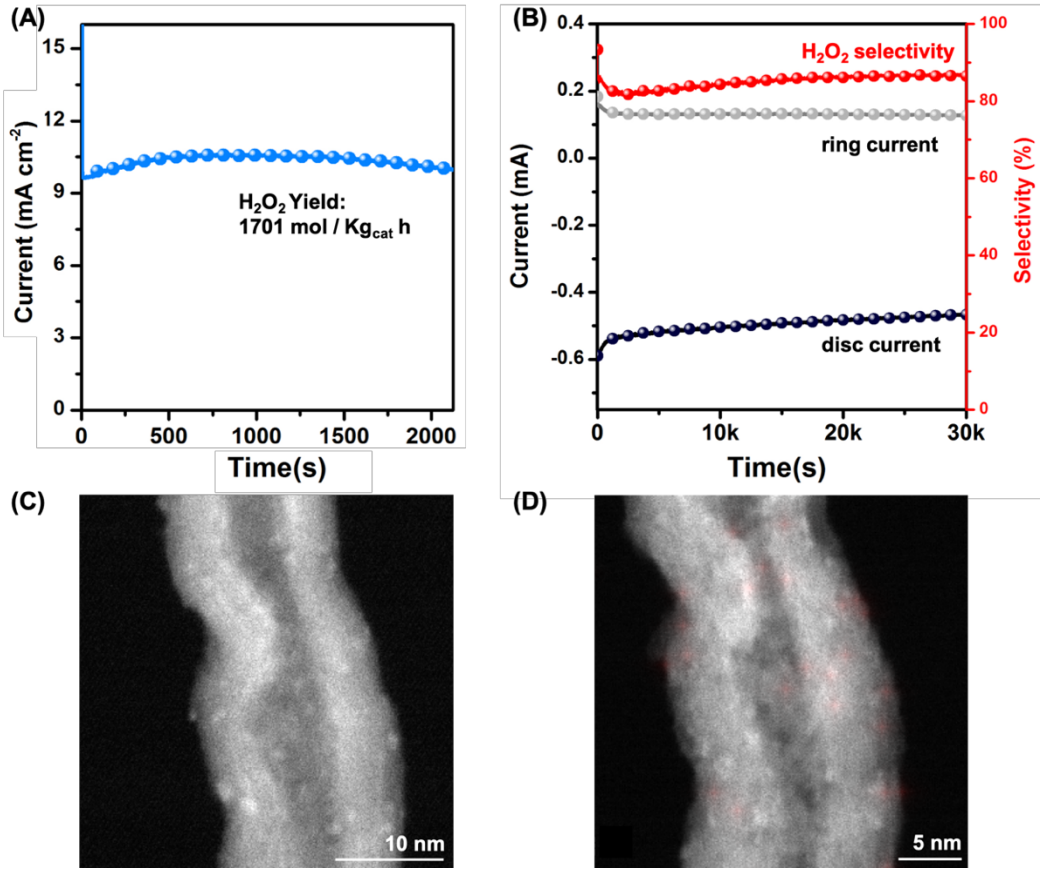

Figure 3.20 Yield and stability of H_2O_2 electrocatalysts in the acid electrolyte. (A) Chronoamperometry curve of $Pd^{\delta+}$-OCNT in the H-cell test at 0.1 V. (B) Stability test of $Pd^{\delta+}$-OCNT in a O_2-saturated 0.1 M $HClO_4$ at 0.1 V. All the experiments were performed at 25 ^oC. ADF-STEM image (C) and its corresponding EDS element mapping (D) of $Pd^{\delta+}$-OCNT after the stability test.

The enhanced $2e^-$ ORR performance of $Pd^{\delta+}$-OCNT was further investigated by DFT calculations. Since the diameter of CNT in the experiment was 10 to 20 nm, a negligible strain energy is expected hence a two-dimensional graphene sheet was used as a model structure[124]. The Pd clusters in defect CNT were first studied by modeling a variety of Pd clusters ranging from 1 to 4 Pd atoms trapped in the vacancies of the

graphene substrate (**Figure 3.21A**). For Pd_1, the possibility of a Pd atom being trapped in either single vacancy or double vacancy of graphene was considered. Larger vacancies were required to trap the Pd_2, Pd_3 and Pd_4 clusters. For Pd_2 and Pd_3 a vacancy with at least 3 missing carbon atoms was required, while for Pd_4 a vacancy with 4 missing carbon atoms was a prerequisite to form a sufficiently stable structure. The $2e^-$ ORR proceeds via $1e^-$ reduction of O_2 to HOO* and subsequent $1e^-$ reduction of HOO* to H_2O_2 where both reduction steps involve HOO* as the sole intermediate. It has been shown that the adsorption energy of HOO* was the key activity descriptor for the $2e^-$ ORR, where the maximum activity observed at an optimized binding of the HOO* intermediate.[8-9] Therefore, the HOO* adsorption energies were calculated on all the model structures. The results are summarized in **Figure 3.21B** in the form of the free energy diagram at the equilibrium potential of the $2e^-$ ORR (0.70V). An ideal catalyst should have a flat free energy diagram at this potential (0.70 V), exhibiting highest catalytic activity with zero overpotential. This plot shows that none of the examined structures are sufficiently active for $2e^-$ ORR as they all bind HOO* too strongly such that further reduction of HOO* to H_2O_2 becomes a bottleneck. Consequently, the bare Pd clusters trapped in the graphene vacancies are not likely the active sites for the $2e^-$ ORR. In fact, the strong tendency of Pd clusters toward adsorbing HOO* results in dissociating the HOO* species to form HO* and O*, indicating that metallic Pd atoms prefer $4e^-$ ORR. Next, the effect of oxidation,

both in the Pd clusters and CNT, was investigated to unravel the active sites responsible for the high 2e$^-$ ORR activity observed in the experiment.

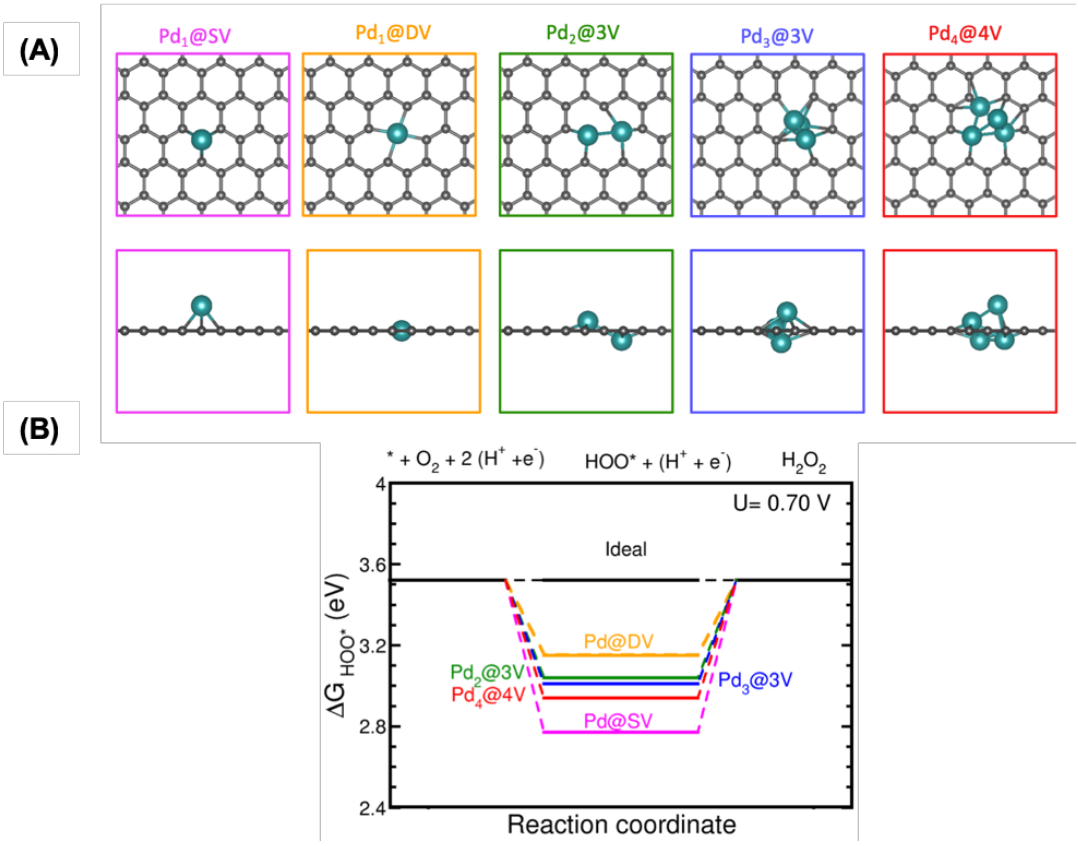

Figure 3.21. (A) Optimized DFT model structures for Pd_n clusters embedded in graphene defects. Color code; C: gray, Cyan: Pd. (B) Free energy diagram for 2e-ORR over different model structures presented in a at standard redox potential (0.70 V).

At the potential of 0.70V it is highly likely that the Pd clusters are covered with several O*, HO* species or a combination of both. To study the oxygenated species coverage effect, only Pd_3 and Pd_4 were considered, which were consistent with the experimental measurements of the Pd cluster size (0.6 nm). **Figure 3.22** display the calculated formation energy of a variety of possible O*/HO* coverages on Pd_3 cluster as

a function of applied potential. The results for the Pd_4 cluster are reported in the **Figure 3.23**. The lowest line at 0.70V displays the most stable coverage in each case. For Pd_3 and Pd_4, 3O*/HO* and 3HO* were the steady state oxygen coverage, respectively. This analysis suggests the presence of the Pd-O bonds, which is in agreement with the EXAFS results. We further took these partially oxidized Pd_n clusters and calculated the HOO* adsorption energy to model the $2e^-$ ORR and to identify trends in activity. The results are summarized in **Figure 3.24** in the free energy diagram plot indicating that the oxygen coverage on the Pd_n clusters improves the HOO* adsorption energy and brings it closer to the range with high ORR activity.

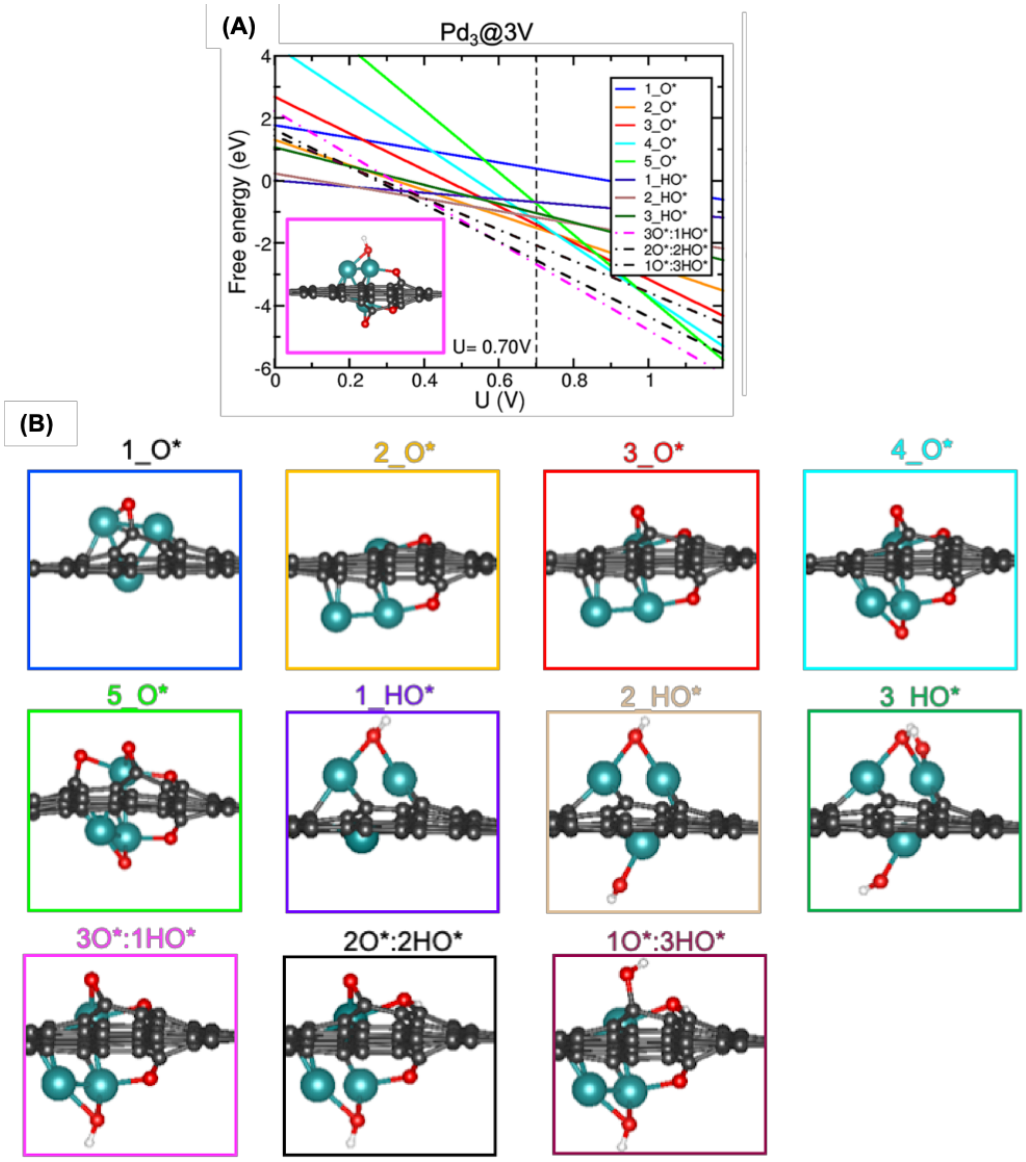

Figure 3.22 (A) Pourbiax diagram for determining the steady state coverage of the oxygenated species on Pd_3 under $2e^-$ ORR standard redox potential (0.70 V). The inset shows the side view of the most stable coverage. (B) Side views of the most stable coverages examined for different oxygenated species on Pd_3@3V. Color code; C: gray, O: red, Cyan: Pd.

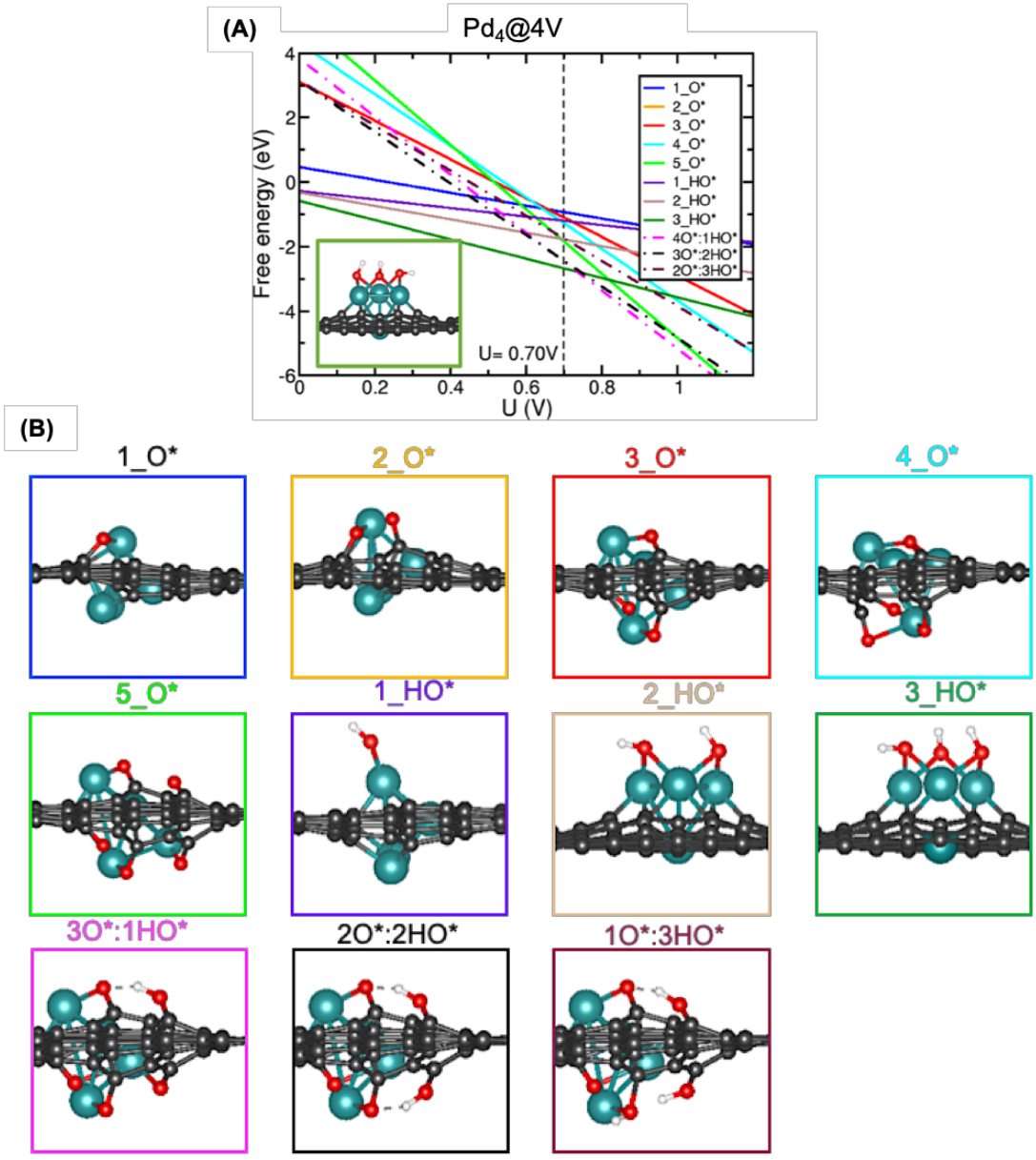

Figure 3.23 (A) Pourbiax diagram for determining the steady state coverage of the oxygenated species on Pd_4 under $2e^-$ ORR standard redox potential (0.70 V). The inset shows the side view of the most stable coverage. (B) Side views of the most stable coverages examined for different oxygenated species on Pd_4@4V. Color code; C: gray, O: red, Cyan: Pd.

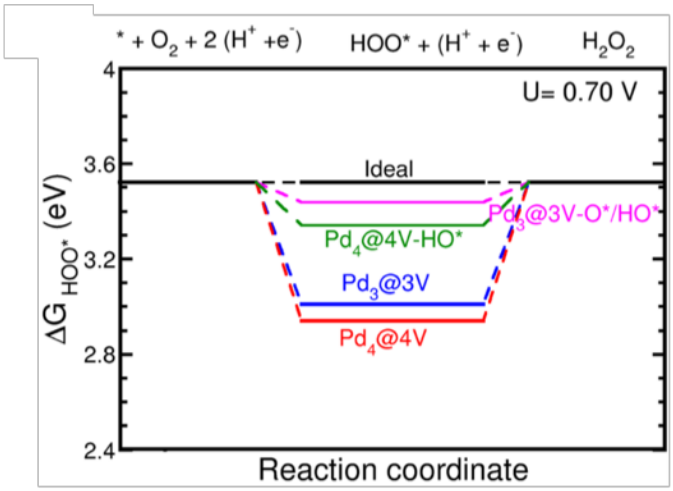

Figure 3.24 Free energy diagram for $2e^-$ ORR over the most stable structure from Pourbiax analysis at 0.70 V.

The CNT substrate was already oxidized from the experimental results, further DFT calculations were performed to examine the effect of neighboring oxygen functional groups on the HOO* adsorption energy. As an example, an oxygen-containing functional group such as epoxy was used to account for the C-O moiety. **Figure 3.25A** displays the atomic structures in the presence of two nearby epoxy groups. The results are summarized in an activity volcano plot (**Figure 3.25B**). The calculated limiting potential (U_L) is used as an indicator of activity toward the $2e^-$ ORR, which is defined as the maximum potential at which both $1e^-$ reduction of O_2 to HOO* and subsequent $1e^-$ reduction of HOO* to H_2O_2 are downhill in free energy. The maximum activity is therefore achieved at the HOO* binding energy of 4.22 eV, which corresponds to the value at the peak of volcano. The results show that the presence of a nearby functional group further improves the

activity of both Pd_3 and Pd_4 and places them at the peak of the activity volcano with zero overpotential. It also shows that the synergy between the oxygen coverage and oxygen functional group plays an important role in improving the catalytic activity of small Pd clusters anchored in OCNT. Therefore, we conclude that the high activity and selectivity observed in the experiments is a direct consequence of the synergy between partially oxidized Pd clusters and oxidized CNT substrate. These two effects together significantly improve the $2e^-$ ORR activity while maintaining high selectivity.

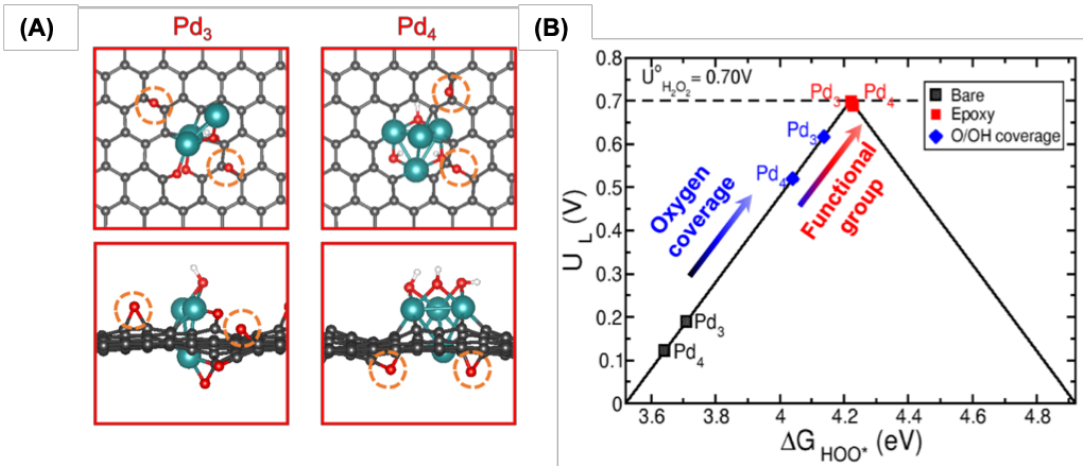

Figure 3.25 (A) Optimized DFT model structures with nearby epoxy functional groups (highlighted by orange dashed circles) on the most stable O*/HO* covered Pd_3 and Pd_4 clusters. (B) Activity volcano plot, the *y* axis is the calculated limiting potential (U_L), defined as the maximum potential at which the reaction steps become downhill in free energy. The *x* axis is the calculated free energy of HOO*. Horizontal dashed line is the standard redox potential for the $2e^-$ ORR (0.70 V).

3.2.3. Conclusions

In summary, this chapter demonstrated a class of $2e^-$ ORR electrocatalysts by the synergistic interaction between partially oxidized Pd clusters and oxygen-functionalized CNT substrate. Through a simple solution-impregnation method, Pd_3 and Pd_4 clusters can be readily deposited on OCNTs with the coordination number of Pd-Pd and Pd-O of 2.5 and 2.7, respectively, as confirmed by the EXAFS characterization. The unique $Pd^{\delta+}$-OCNT electrocatalyst showed high H_2O_2 selectivity at 95% to 98% in a wide potential range of 0.3 to 0.7 V, and a positive shift of the $2e^-$ ORR onset potential by ~ 320 mV compared to the OCNT substrate. The mass activity of $Pd^{\delta+}$-OCNT was 1.946 A mg^{-1} at 0.45 V, 1.5-fold higher than Pd_2Hg_5/C, which was the best electrocatalyst reported for H_2O_2 synthesis in acidic electrolytes. In addition, the H_2O_2 yield rate was estimated to be 1700 mol / k g_{cat}^{-1} h^{-1} in an H-cell test, and the $Pd^{\delta+}$-OCNT electrocatalyst maintained excellent stability with no decrease of the H_2O_2 selectivity above 8 h of testing, suggesting its promise for the electrochemical synthesis of H_2O_2. DFT calculations further suggest that the coordination between oxygen-modified Pd clusters and the oxygen-containing functional groups on OCNT is the key for their high selectivity and activity for $2e^-$ ORR. This work offers a unique path toward the development of highly selective ORR electrocatalysts by simply tuning the interactions between the active metal and the oxidized carbon support.

3.2.4. Acknowledgements

Chapter 3.2, in full, is a reprint of the material "Promoting H2O2 Production via 2-Electron Oxygen Reduction by Coordinating Partially Oxidized Pd with Defect Carbon" as it appears in Nature Communications, Qiaowan Chang, Pu Zhang, Amir Hassan Bagherzadeh Mostaghimi, Xueru Zhao, Steven R. Denny, Ji Hoon Lee, Hongpeng Gao, Ying Zhang, Huolin Xin, Samira Siahrostami, Jingguang G. Chen, Zheng Chen, 2020, 11, 2178-2187. The dissertation author was the first author of this paper and conducted all the essential research work.

Chapter 4. Carbon dioxide reduction reaction

Efficient CO_2 storage and utilization technologies are urgently needed to mitigate the global climate change and ocean acidification issues caused by the continuing increase of CO_2 level from the utilization of fossil fuels[125]. The electrochemical CO_2 reduction reaction (CO_2RR), combined with renewable energy sources (i.e. solar and wind), represents a promising solution[126-129].

4.1. Introduction

4.1.1. Reaction mechanisms

In CO_2RR, CO_2 can be converted into CO, hydrocarbons, or oxygenates. Since the reaction is generally performed under cathodic conditions in aqueous electrolyte, H_2 is inevitably produced as a byproduct from the competing hydrogen reduction reaction (HER). While significant efforts have been made on prohibiting HER by designing sophisticated electrocatalysts, electrodes or cell structures, low selectivity toward CO_2RR remains a critical challenge.[130-132] Instead of suppressing HER, combining the CO_2RR and HER together has been considered as a viable approach, which produces syngas (CO and H_2) with tunable CO/H_2 molar ratios that can be readily used to manufacture value-added chemicals using exiting thermochemical processes, such as the Fischer–Tropsch and methanol synthesis reactions [133-136].

4.1.2. Literature review of electrocatalysts

Palladium (Pd) has been identified as a potential candidate for the production of syngas via CO_2RR [133, 137-141]. While Pd itself is a good HER catalyst, it was considered to be unsuitable for CO production in CO_2RR due to its strong CO binding that leads to CO poisoning.[142] Sheng *et al*. revealed that Pd can be transformed into palladium hydride (PdH_1) that presents decreased *CO and *H binding energies, which in turn adjusts the CO/H_2 ratios from the CO_2RR and thus makes Pd as a potential electrocatalyst for syngas production[133]. Moreover, the CO/H_2 ratio can be further improved by using Pd-based bimetallic catalysts and/or supporting Pd on metal carbides and nitrides [135, 137, 143]. The key to tune the CO/H_2 ratio over Pd-based electrocatalyst is to control the formation of the PdH_1 phase, specifically, the hydride formation potentials during the CO_2RR. Lee *et al*. found that by alloying with first-row transition metals, the hydride formation potentials of PdM (M = Cu, Ni) were cathodically shifted, enabling the syngas production with the CO/H_2 ratios between 1 and 2 at 0.9 V (*vs*. reversible hydrogen electrode or RHE)[137]. In spite of these prior investigations, the electrocatalytic performance of PdH_x has been rarely explored with different H contents, especially in a view point of the structure–property–activity relationship. Moreover, it is not a trivial task to further enhance its CO_2RR activity and tune the CO/H_2 ratio in a range of 1-2 (desired for the thermochemical processes) in the low overpotential range (between -0.5 and -0.7 V)[137, 141].

4.2. Pre-hydridizing Pd Nanocubes

4.2.1. Experimental

4.2.1.1. Electrocatalysts synthesis

To control the size of Pd NCs, the amounts of KCl and KBr were varied. [144] The reaction mixture including 60 mg of AA, 105 mg of PVP (Mw ≈ 55,000), different amount of KCl (150 mg for 7 nm and no addition for 13 and 19 nm in nominal size), different amount of KBr (5, 300, and 600 mg for 7, 13, and 19 nm in nominal size, respectively) and 8 mL of DI water was placed in a 25 mL glass vial, which was pre-heated at 80 °C for 10 min in an oil bath under magnetic stirring. Then, 3 mL of DI water containing 57 mg of Na_2PdCl_4 was added into the pre-heated mixture. The vial was maintained at 80 °C for 3 h. The final product was collected by centrifugation at 12,000 rpm for 10 min. The resulting Pd NCs were re-dispersed in ethanol or DMF.

After centrifugation of Pd NCs, they were dispersed in 30 mL of DMF (0.67 mg_{Pd}/ mL) solution containing 30 mg of PVP. The reaction mixture was heated at 160 °C for 16 h in an oil bath under magnetic stirring. The final product was collected by centrifugation at 12,000 rpm for 10 min. The resulting $PdH_{0.40}$ NCs were re-dispersed in ethanol.[145]

Suspension of 20 mg Pd NCs or $PdH_{0.40}$ NCs and 80 mg of Vulcan XC-72 carbon black were dispersed in 15 mL of ethanol. Then the mixture was sonicated for 2 h and the product was collected by centrifugation. Each catalyst was washed five times with ethanol and dried by Argon (Ar) gas.

4.2.1.2. Characterization

TEM images were taken using a HT-7700 microscope (HITACHI, Japan) operated at 100 kV by drop casting the nanoparticle dispersions on carbon-coated copper grids and drying under ambient conditions. High-resolution TEM studies were carried out in a Titan G2 ChemiSTEM Cs Probe microscope (FEI, USA) operated at 200 kV. XRD patterns were collected with X-ray diffracter (PANalytical X'pert PRO-MPD/MRD) using a Cu-Kα radiation at 40 kV and 25 mA. TEM and XRD instruments were conducted at Korea Basic Science Institute (KBSI, Daegu Korea). XPS was measured through Scientific ESCALAB 250Xi system (ThermoFisher) with Al Kα X-ray (1486.6 eV) as the light source, which was conducted at National NanoFab Center (NNFC, Daejeon, Korea). Metal contents in nanocrystals were determined by ICP-AES (Perkin-Elmer, Optima 7300DV).

4.2.1.3. Electrochemical measurements

The air-tight H-cell was used for the electrochemical measurement. The 0.5M sodium bicarbonate ($NaHCO_3$) solution prepared from CO_2-saturated 0.25M sodium carbonate (Na_2CO_3) solution was utilized as an electrolyte. The catalyst ink was prepared by dispersing 2.5 mg of electrocatalysts in a mixture solution containing 2.0 ml of Milli-Q water, 0.5 ml of isopropanol, 10 µl of Nafion (5%) and then 100 µl of each catalyst ink was deposited on a working electrode (carbon paper: Toray carbon paper 060). The graphite paper and Ag/AgCl (3M Cl^-) were used as the counter and reference electrode, respectively. The potentials were calibrated to a reversible hydrogen electrode (RHE). During the test, the electrolyte was vigorous stirred to mitigate the mass transport limitation of dissolved CO_2. To obtain stable electrochemical CO_2 reduction data, the working electrode was first held at -0.05 V for 60 s to remove the capping agents (PVP, Br^-) of electrocatalysts and then cycled in 0.02-0.8 V for 3 times at 50 mV s^{-1}. After purging CO_2 for additional 10 min, the CA test was used to evaluate the CO_2RR performance of electrocatalysts by holding each potential (from -0.5 to -1.0 V) for a designated duration. After finishing the CA test at specified potential, 100 µL of gas in the empty head space (~ 17 ml) of cathodic compartment was injected into gas chromatography (GC, S46 Agilent, Agilent 7890B) to obtain the gaseous product distribution. The CO stripping experiment were performed to obtain the ECSA of electrocatalysts. The CO adsorption was achieved by holding the pre-cleaned electrode potential at 0.05 V for 10 min in a CO-saturated 0.1 M KOH. The excess CO was cleared

by purging Ar for 30 min. The CO stripping curves were then taken with a scanning rate of 50 mV s^{-1}. The Cu underpotential deposition (Cu UPD) was conducted in a Ar-saturated 50 mM H_2SO_4 + 50 mM $CuSO_4$ solution at 10 mV s^{-1}.

The composition of $PdH_{0.40}$ was determined by applying the following Equation 4.1 based on the relationship between the lattice parameter (α_0) and the composition ratio of H to Pd (x) within the PdH system:[146]

$$\frac{3}{\alpha_0}\frac{\Delta\alpha_0}{\Delta x} = 0.19 \pm 0.01$$

(Eq. 4.1)

The Faradaic efficiency (FE) of CO and H_2 were calculated by the below equations.[133, 137]

The amount of CO in gaseous phase ($N_{\mathrm{CO-gas}}$):

$$N_{\mathrm{CO-gas}} = \frac{C_{co} \times V_{\mathrm{gas}}}{22.4\ L\ mol^{-1}}$$

(Eq. 4.2)

The amount of CO in liquid phase ($N_{\mathrm{CO-liquid}}$):

$$N_{\mathrm{CO-liquid}} = \frac{C_{co} \times V_{\mathrm{liquid}} \times K_{CO} \times 1g\ ml^{-1}}{18\ g\ mol^{-1}}$$

(Eq. 4.3)

The FE of CO (FE_{CO}):

$$FE_{\mathrm{CO}} = \frac{(N_{CO-gas} + N_{\mathrm{CO-liquid}}) \times 2 \times 96485\ C\ mol^{-1}}{Q} \times 100$$

(Eq. 4.4)

The current density of CO (J_{CO} and $J_{\mathrm{CO-Pd}}$):

$$J_{\mathrm{CO}} = \frac{FE_{\mathrm{CO}} \times Q}{A \times t}$$

(Eq. 4.5)

$$J_{\mathrm{CO-Pd}} = \frac{FE_{\mathrm{CO}} \times Q}{A_{Pd} \times t}$$

(Eq. 4.6)

In the above equations, C_{co} is the CO concentration (%)in the empty head space obtained from GC analysis; K_{CO} is CO molar solubility in water at CO partial pressure of 1 bar and room temperature, 1.774×10^{-5}; Q is the coulomb for the reaction at each potential; A and A_{Pd} are the geometrical area and ECSA of the working electrode; t is the reaction time at each potential. The calculation for H_2 is similar with that of CO. The K_{H_2} is 1.411×10^{-5}.

4.2.1.4. XAFS measurements

A lab-made acryl kit was used for the *in-situ* XAFS measurement. The areal mass loading of the working electrode was ~5 mg cm^{-2} to achieve sufficient XAFS signal. During the measurements, CO_2 gas was continuously bubbled into the electrolyte. The hydrogen electrode (Hydroflex, E-DAQ) was used as a reference electrode. The other electrochemical conditions were the same as in the electrochemical measurements. *In-situ* XAFS measurements were conducted on the 7-BM (QAS) beamline in National

Synchrotron Light Source-II (NSLS-II) at Brookhaven National Laboratory. The XAFS signal was recorded with a fluorescence mode using a Canberra PIPS detector. The electrocatalytic performance was measured by stepwise potential sweeping from 0.6 V to -0.9 V. Each potential was held for 10 min using chronoampherometry technique during the XAFS measurement. The typical duration for a single spectrum was ~45 sec and the last ten spectra measured at each potential were merged to get high signal-to-noise spectrum. During the measurements, the reference spectrum of Pd foil was recorded at the same time, and was further used in calibrating the edge energy (E_0) of the samples under analysis.

The obtained spectra were processed using the ATHENA and ARTEMIS software in IFFEFIT package[71-72, 147]. EXAFS analyses were conducted by using the ARTEMIS software. The EXAFS spectrum ($\chi(k)$) was weighted with k^2 value to intensify the signal in the high k-regime. The Hanning window was utilized for the Fourier-transform. All of the EXAFS fittings were done in the R-space. The goodness of fitting was evaluated based on the reliable factor (*R*-factor) and reduced chi-square (reduced χ^2). The amplitude reduction factor for Pd was obtained from the reference Pd foil. For the EXAFS fitting, FCC Pd (a=3.900 Å) model was used. All of the data were co-refined using this model. A single scattering path between Pd and its first neighbor Pd was taken into consideration for all EXAFS fitting.

4.2.1.5. DFT calculations

DFT[148-149] calculations were performed using the plane wave VASP code.[76-77] The core electrons were described using the PAW with the GGA[78, 150], using PW91 functionals.[53] A plane-wave basis set with a kinetic energy cutoff of 400 eV was used in all calculations. The Brillion zone integration was performed using a 3 × 3 × 1 Monkhorst-Pack grid.[54]

The Pd(100) surface was modeled using a six-layer 3 × 3 surface slab. Similarly, the H-terminated PdH(100) and $PdH_{0.5}$(100) surfaces were modeled using six-layer 3 × 3 surface slabs using the NaCl crystal structure for bulk PdH and $PdH_{0.5}$ (with 50 % fewer H atoms compared to bulk PdH), respectively. A vacuum layer of ≈14 Å thick was added in the slab cell along the direction perpendicular to the surface to minimize the artificial interactions between the surface and its periodic images. During geometry optimization, atoms in the top three layers were allowed to relax while atoms in the bottom three layers were fixed until the Hellman–Feynman force on each ion was smaller than 0.01 eV $Å^{-1}$. The *B.E.* of adsorbate was calculated as:

$$B.E.(adsorbate) = E(slab + adsorbate) - E(slab) - E(adsorbate)$$

where E(slab + adsorbate), E(slab), and E(adsorbate) are the total energy of slab with adsorbate, clean slab, and adsorbate in the gas phase, respectively. E(H) is taken as one-half of the total energy of the H_2 molecule during the calculation of hydrogen BE.

The Gibbs free energy (G) is calculated as [151]

$$G = E + ZPE - TS$$

Here, E is the total energy obtained from DFT calculations, ZPE and S are the zero-point energy and entropy respectively, and T= 298.15 K.

The free energy diagram of CO_2RR to CO has been calculated by considering the following sequential steps:[132]

$$CO_2(g) + (H^+ + e^-) + * \rightarrow *HOCO$$

$$*HOCO + (H^+ + e^-) \rightarrow *CO + H_2O(g)$$

$$*CO \rightarrow CO(g) + *$$

In aqueous electrolytes, the HER inevitably takes place via the following sequential steps,[10] and competes with the CO_2RR:

$$H^+ + e^- + * \rightarrow *H \text{ (Volmer step)}$$

$$*H + H^+ + e^- \rightarrow H_2(g) + * \text{ (Heyrovsky step)}$$

4.2.2. Results and discussions

$PdH_{0.40}$ NCs were obtained from the hydrogenation of as-prepared Pd NCs with the assistance of N,N-dimethylformamide (DMF) and polyvinyl pyrrolidone (PVP) (see the details in supporting information)[145]. TEM images (**Figure 4.1A and B**) showed the well-controlled cubic morphology of monodispersed Pd and $PdH_{0.40}$ NCs. After the hydrogenation conversion from Pd to $PdH_{0.40}$ NCs, the original Pd cubic morphology could be retained, indicated by the similar average edge length of Pd (7.1 ± 0.8 nm) and

$PdH_{0.40}$ (7.3 ± 0.5 nm) NCs, and their high shape uniformity (> 90%) (**Figure 4.2**). The high- resolution TEM (HRTEM) images for an individual Pd and $PdH_{0.40}$ NC presented dominant Pd(200) facet exposed on both the NC surfaces (**Figure 4.3A and B**). Due to the insertion of H into the Pd lattice, the lattice spacing for the Pd(200) plane was increased from 1.94 Å (Pd NCs) to 1.99 Å ($PdH_{0.40}$ NCs) as shown in **Figure 4.3C and D**, in good agreement with the XRD results (**Figure 4.4A**). The elemental composition of $PdH_{0.40}$ NCs was determined by the linear relationship of lattice distance with hydrogen content[146] (Table 4.1). The XRD patterns showed no peak shift after storing $PdH_{0.4}$ NCs at room temperature in air even for 12 months (**Figure 4.4B**), indicating their good stability[152].

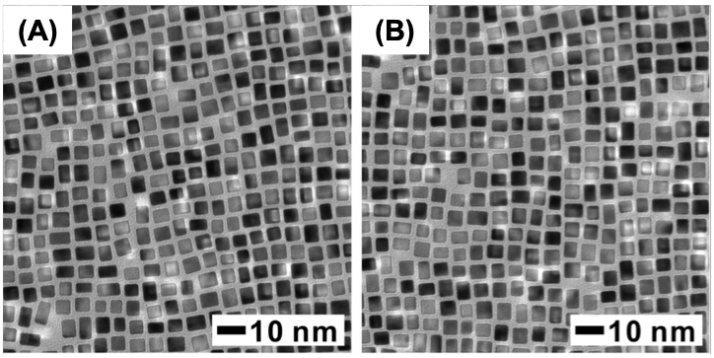

Figure 4.1 TEM images of (A) Pd and (B) $PdH_{0.40}$ NCs of 7 nm in norminal size.

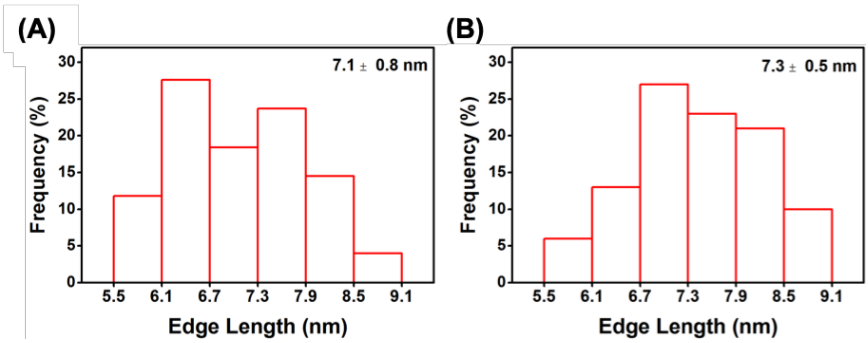

Figure 4.2 Size distributions of (A) Pd and (B) $PdH_{0.40}$ NCs of 7 nm in nominal size.

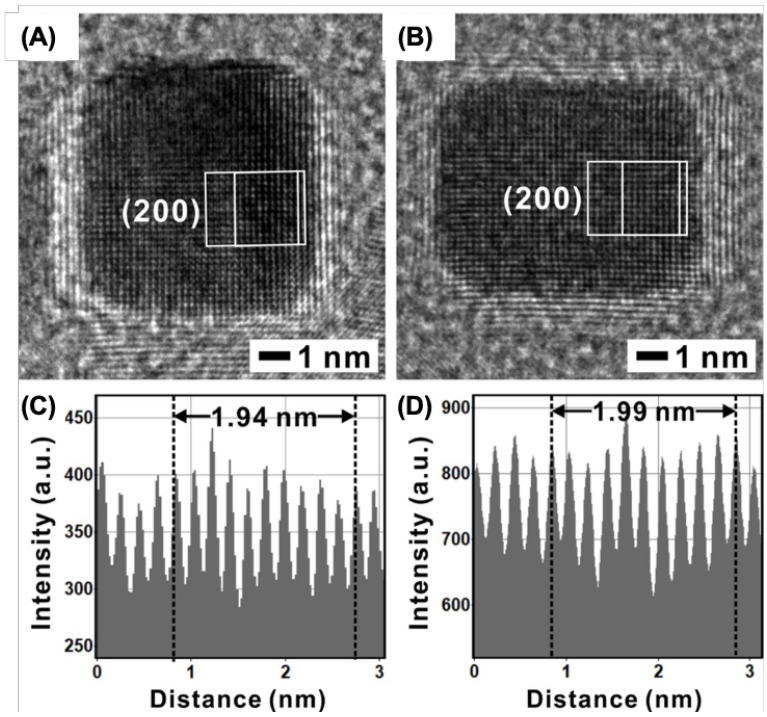

Figure 4.3 HRTEM images of (A) a Pd and (B) a $PdH_{0.40}$ NCs of 7 nm. Intensity profiles recorded from the area indicated by the rectangular box in HRTEM image for (C) a Pd and (D) a $PdH_{0.40}$ NC.

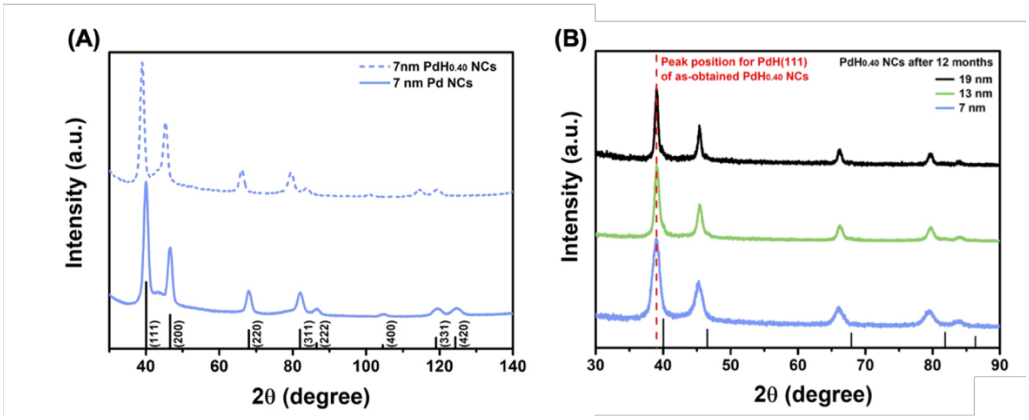

Figure 4.4 XRD patterns of 7 nm of Pd and $PdH_{0.40}$ NCs. Black vertical lines representing the Pd reference peaks (JCPDS# 46-1043).

Table 4.1 Lattice distance of 7 nm of Pd-based nanocrystals measured from XRD

sample	2θ of [137] peak (°)	Corresponding lattice distance (nm)	Approximate composition
7 nm Pd NCs	40.01	0.3905	H:Pd = 0
7 nm $PdH_{0.40}$ NCs	39.01	0.4000	H:Pd = 0.40

The electronic structures of the Pd and $PdH_{0.40}$ NCs were revealed by the core-level and valence band spectra from XPS. Compared with Pd NCs, the Pd 3d core level spectrum of $PdH_{0.40}$ NCs was shifted to a higher binding energy (**Figure 4.5A**), and its valence band spectrum presented a decreased bandwidth and emergence of two small shake-up peaks (marked as red arrows, **Figure 4.5B**). These phenomena could be attributed to the reduction of the density of state near the Fermi level of $PdH_{0.40}$ relative to the Pd counterpart, specifically, the charge transfer between fully filled Pd 4d orbital

and half-empty H 1s orbitals[153-154]. These XPS results confirmed the formation of Pd hydride associated with the charge transfer between Pd and H[145].

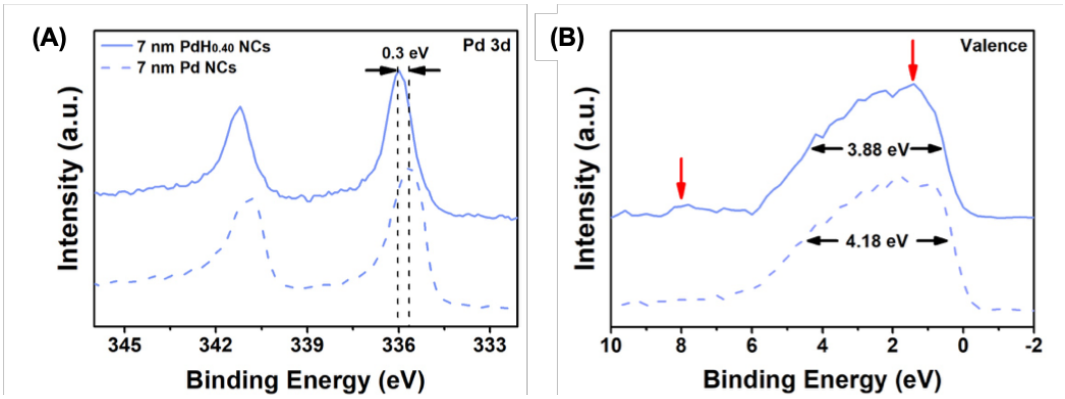

Figure 4.5 XPS spectra of (A) Pd 3d and (B) valence band structures for 7 nm Pd and $PdH_{0.40}$ NCs. Red arrows highlighting small shake-up peaks in $PdH_{0.40}$ NCs.

To perform electrochemical test, 7 nm Pd and $PdH_{0.40}$ NCs were supported on carbon black (Pd NCs/C and $PdH_{0.40}$ NCs/C). The CO_2RR activity and selectivity of 7 nm Pd and $PdH_{0.40}$ NCs/C catalysts toward gaseous products were compared by the CA test and gas chromatography (GC) quantification under the operating potential range between -0.5 and -1.0 V (**Figure 4.6**). **Figure 4.7A** showed that the total Faradaic efficiencies (FEs) of CO (FE_{CO}) and H_2 (FE_{H2}) were in the range of 88-100% for both samples, indicating that CO and H_2 were the major products. With increasing overpotential, the trends for the changes in FE_{H2} and FE_{CO} were different. From -0.6 V, both electrocatalysts presented decreased FE_{CO} and increased FE_{H2} toward higher potential, leading to reduced CO/H_2 ratios (**Figure 4.7B**). The decrease of FE_{CO} could be ascribed to the limited CO_2 solubility

during the CO_2RR, thus incurring the mass transport limitation of reactant to the electrode surface, while for FE_{H2}, the reaction kinetics of HER was not limited by the diffusion of the proton donor in the aqueous electrolyte.

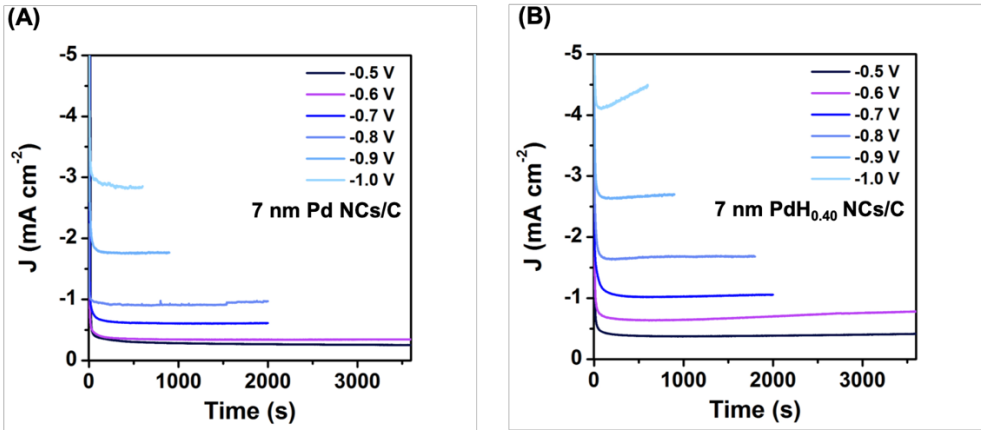

Figure 4.6 CA curves for different catalysts at given potential. (A) 7 nm Pd NCs/C, (B) 7 nm $PdH_{0.40}$ NCs/C.

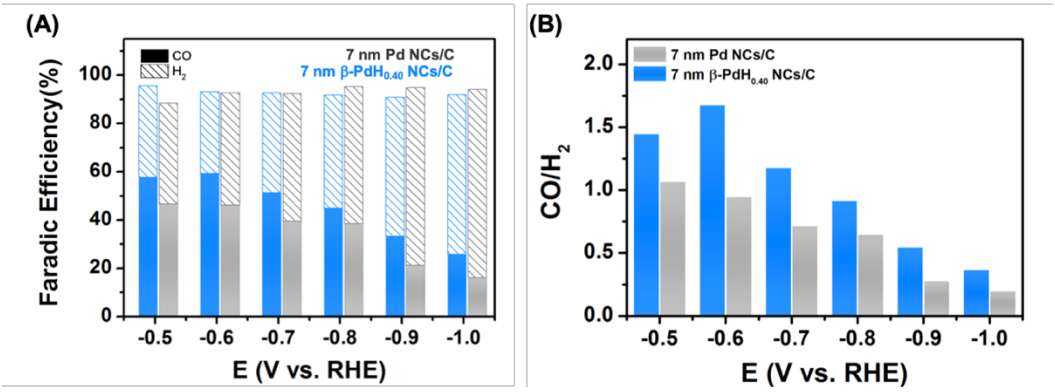

Figure 4.7 Electrocatalytic performance of 7 nm Pd and $PdH_{0.40}$ NCs/C from -0.5 to -1.0 V. (A) Faradaic efficiency of CO and H_2. (B) CO/H_2 ratio.

When comparing the CO_2RR performance between Pd and $PdH_{0.40}$ NCs/C, the advantage of the prehydridized structure ($PdH_{0.40}$ NCs/C) was manifested by the tunable CO/H_2 ratios for syngas production with a significantly enhanced partial current density of CO. For example, at -0.6 V the CO/H_2 ratio obtained over Pd NCs/C was 0.95, which was increased to 1.68 over $PdH_{0.40}$ NCs/C. To obtain the syngas production with the CO/H_2 ratio in the range of 1 to 2, the suitable potential for Pd NCs/C was allowed at -0.5 V only, while for $PdH_{0.40}$ NCs/C, the potential range was extended from -0.5 to -0.8 V, making it more favorable to the syngas production from CO_2RR. Moreover, the partial current density of CO (J_{CO}) based on geometric electrode area of $PdH_{0.40}$ NCs/C also showed considerable enhancement compared with Pd NCs/C (**Figure 4.8A**). For instance, the J_{CO} of $PdH_{0.40}$ NCs/C was 2.6 times of the Pd counterparts at -0.6 V. Considering the smaller ECSA of $PdH_{0.40}$ NCs/C due to the exposed surface *H species (Table 4.2), the J_{CO} based on ECSA of Pd ($j_{CO\text{-}Pd}$) of 7 nm $PdH_{0.40}$ was further increased by 2.2-fold compared with that of Pd NCs/C at -0.6 V, suggesting a significantly improved CO_2RR activity (**Figure 4.8B**). Both of Pd and $PdH_{0.40}$ NCs/C presented good stability at -0.7 V (**Figure 4.9**).

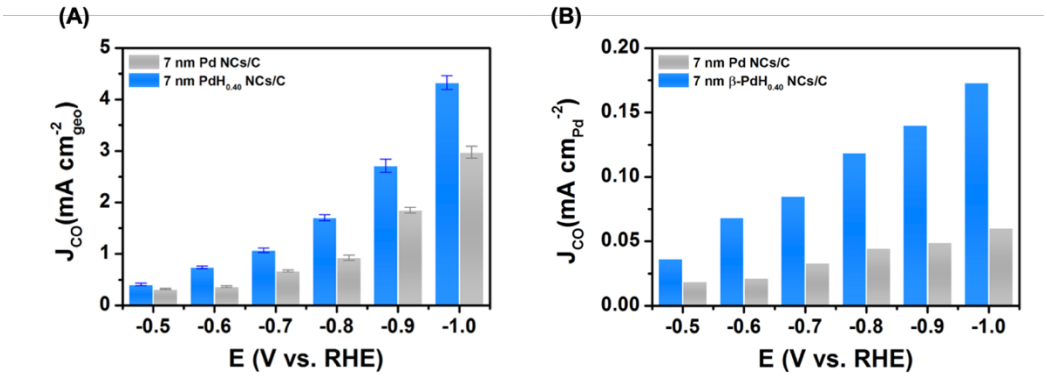

Figure 4.8 Partial current density of CO based on (A) geometric area (J_{CO}) and (B) electrochemical surface area ($j_{CO\text{-}Pd}$) of 7 nm Pd and $PdH_{0.40}$ NCs/C from -0.5 to -1.0 V in 0.5 M $NaHCO_3$ solution.

Table 4.2 ECSA of various Pd-based nanocrystals measured from Cu UPD.

Sample	ECSA ($m^2\ g^{-1}$)
7 nm Pd NCs	56.0
7 nm $PdH_{0.40}$ NCs	48.1

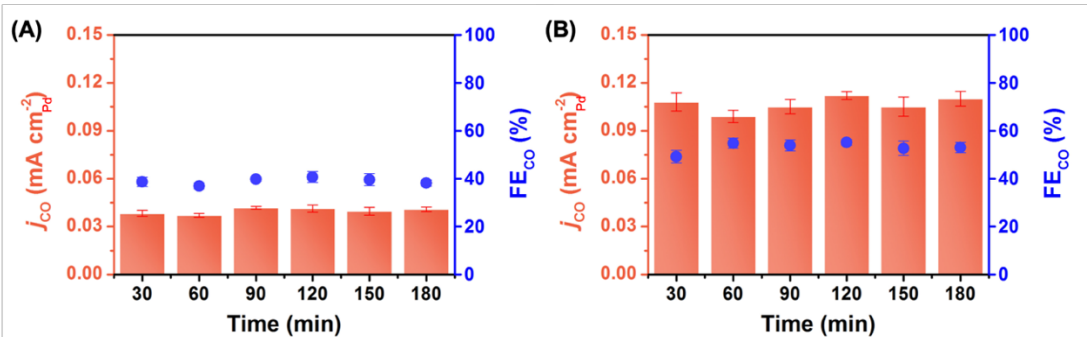

Figure 4.9 Stability result of 7 nm (A) Pd and (B) $PdH_{0.40}$ NCs/C at -0.7 V for 3 h.

It is well-established that Pd can be readily transformed to PdH_1 at the electrochemical potentials for the CO_2RR[133]. Accordingly, the active phase of both Pd and $PdH_{0.40}$ NCs/C in the CO_2RR should be PdH_1 NCs. In that case, one should expect similar

CO_2RR performance for the Pd and $PdH_{0.40}$ NCs/C electrocatalysts. However, experimental results showed significantly different CO_2RR performance, with $PdH_{0.40}$ NCs/C being far superior to Pd NCs/C.

Ex-situ XAFS analysis was first performed to compare the chemical nature of Pd and $PdH_{0.40}$ NCs/C. Compared with Pd NCs/C, $PdH_{0.40}$ NCs/C showed negative shift of XANES profile and longer Pd-Pd bond distance from EXAFS result, demonstrating the successful formation of Pd hydride (**Figure 4.10** and Table 4.3). In an attempt to monitor the change of the local chemical environment of Pd and $PdH_{0.40}$ NCs/C during the CO_2RR, *in-situ* XAFS analysis was then conducted (**Figure 4.11**) to investigate the origin of the enhanced CO_2RR performance of $PdH_{0.40}$ NCs/C. Upon decreasing the potential for the electrochemical reduction from 0.6 V to -0.9 V, both Pd and $PdH_{0.40}$ NCs/C showed the gradual shift in the XANES profiles (**Figure 4.11A and B**) toward lower energy concurrently with an increase in the Pd-Pd interatomic distance as shown in the EXAFS profiles (**Figure 4.11C and D**, Table 4.4). This can be attributed to the H uptake and consequent lattice expansion associated with the PdH_1 formation. However, the prehydridization process was found to play a role in the onset potential for the PdH_1 formation. The phase transition for Pd NCs/C took place at -0.7 V as evidenced by the shifts in both XANES and EXAFS profiles. For the $PdH_{0.40}$ NCs/C, this phase transition occurred at less cathodic potential of -0.3 V, indicating that the $PdH_{0.40}$ NCs more readily accepted the additional H compared to Pd NCs. The different H uptake manners could be

more explicitly displayed in the change of the Pd-Pd interatomic distance for both catalysts as a function of applied potential (**Figure 4.11E**), illustrating the distinct electrochemical onset potentials toward the PdH_1 formation.

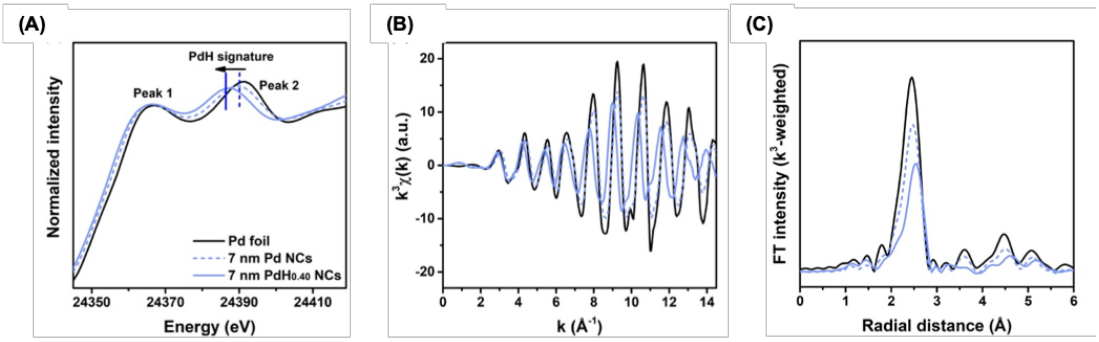

Figure 4.10 (A) XANES, (B) k^3-weighted EXAFS, and (C) Fourier transforms (FTs) of k^3-weighted EXAFS spectra for Pd and $PdH_{0.40}$ NCs at Pd K-edge.

Table 4.3 The peak position, the energy difference, and the ratio of peak intensities (I_1/I_2) for peak 1 and 2 in XANES spectra for samples.

Sample	Peak position (eV)		Peak energy differences (eV)	I_1/I_2 ratio
	peak 1	peak 2		
Pd foil	24366.9	24390.9	24.0	0.8935
Pd NCs	24366.7	24389.7	23.0	0.9143
$PdH_{0.40}$ NCs	24366.4	24387.8	21.4	0.9240

Table 4.4 EXAFS fitting results of Pd/C and Pd-NC under the *in-situ* measurement.

Parameter	Catalysts	
	Pd NCs/C	$PdH_{0.4}$ NCs/C
Independent Points	183.75	168
Number of Variables	56	56
Reduced Chi-square	27.5089688	351.6664396
R-factor	0.0077496	0.0099363
k-range	2.086 – 12.642	1.805 – 11.450
R-range	1.25 – 3.25	1.3 – 3.3
Number of Data Set	14	14

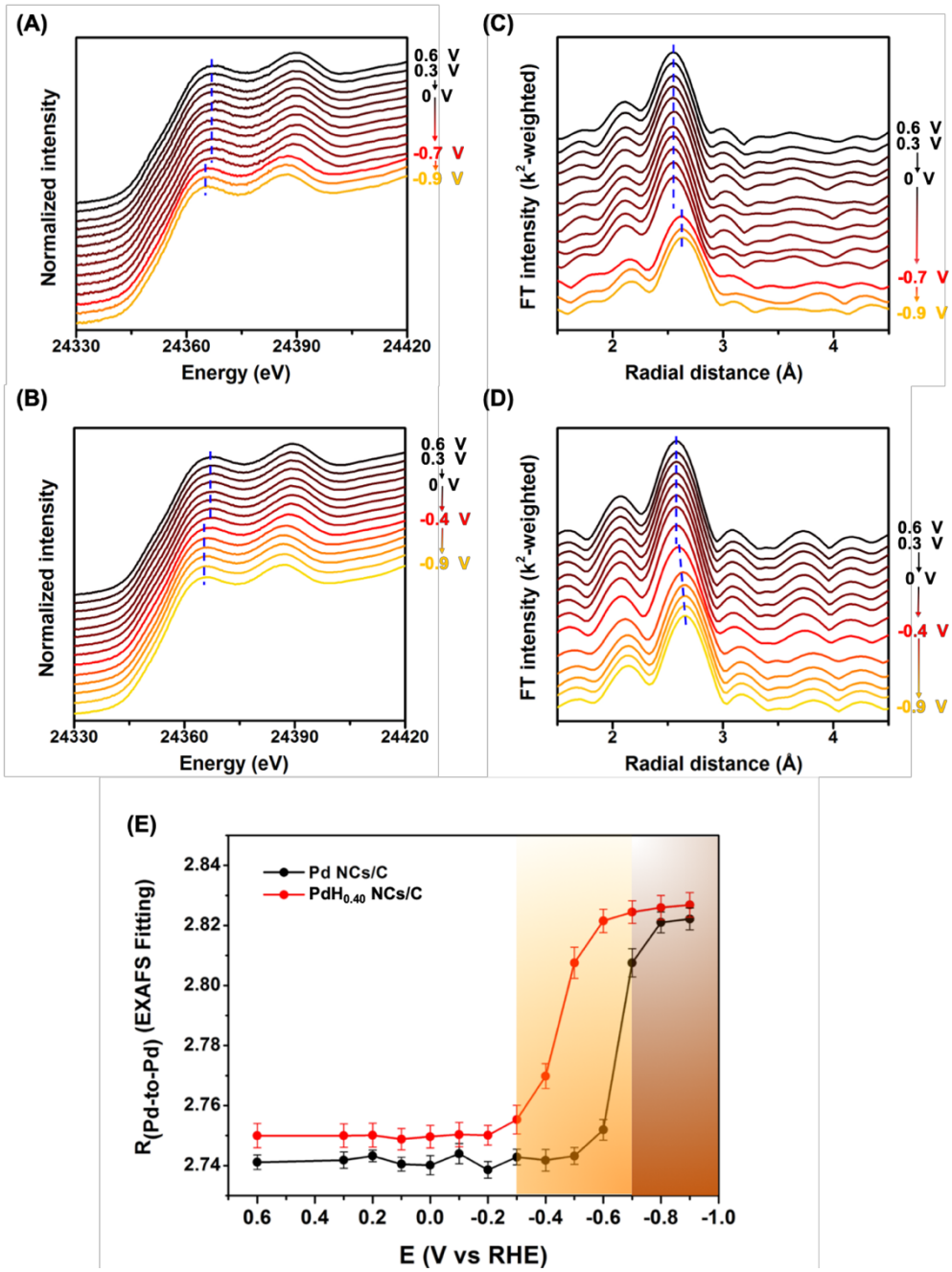

Figure 4.11 *In-situ* XAFS profiles measured at Pd K-edge. Normalized XANES profiles for (A) 7 nm Pd NCs/C and (B) $PdH_{0.40}$ NCs/C. k^2-weighted EXAFS spectra for (C) 7 nm Pd NCs/C and (D) $PdH_{0.40}$ NCs/C. (E) The interatomic distance ($R_{Pd\text{-}Pd}$) profiles for Pd and $PdH_{0.40}$ NCs/C as a function of applied potential determined from *in-situ* EXAFS analysis.

The facile transformation of $PdH_{0.40}$ to PdH_1 can be interpreted by several factors. One can speculate that the H uptake involved in the PdH formation entails an energy penalty related to (1) the mix of Pd and H orbitals, (2) the increase in the Pd-Pd distance, and (3) the resultant multiple H diffusion into the Pd lattice. Therefore, the prehydridization process should be efficient in mitigating the penalty by mixing the orbitals of Pd and H and increasing the Pd-Pd interatomic distance in advance, thus allowing the PdH formation to occur at a lower potential (reduced by 300 mV). This is further supported by the linear sweep voltammetry (LSV) curves (**Figure 4.12**). Both catalysts showed the broad redox peaks associated with the PdH formation. Compared with Pd NCs/C, the peak in $PdH_{0.40}$ NCs/C was shifted positively by ~40 mV. Furthermore, the earlier PdH_1 formation endowed $PdH_{0.40}$ with better tolerance against CO-poisoning, thus leading to a more rapid response of voltammetric current and an improved CO_2RR activity of $PdH_{0.40}$ NCs/C after -0.8 V, even though both electrocatalysts presented the same stoichiometry of PdH_1. The CO stripping experiment was conducted to investigate the CO anti-poisoning capability for both samples (**Figure 4.13**). Compared with Pd NCs/c, the main CO oxidation peak of $PdH_{0.40}$ NCs/C was negatively shifted by ~ 20 mV, implying its enhanced CO anti-poisoning effect from the hydride structure. We also evaluated the CA of the $PdH_{0.40}$ in 0.1 M KOH solution at 1.2 V for 5 min and compared the phase and composition before and after the test using XRD (**Figure 4.14**). The results

showed no peak shift during CA test, indicating PdH phase is stable under the whole CO-stripping potential.

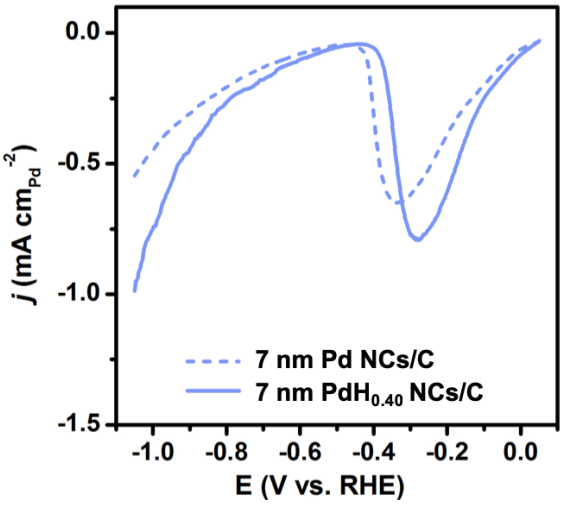

Figure 4.12 Linear sweep voltammetry (LSV) curves of 7 nm Pd and $PdH_{0.40}$ NCs/C in 0.5M $NaHCO_3$ solution with a scan rate of 10 mV s^{-1} without IR correction.

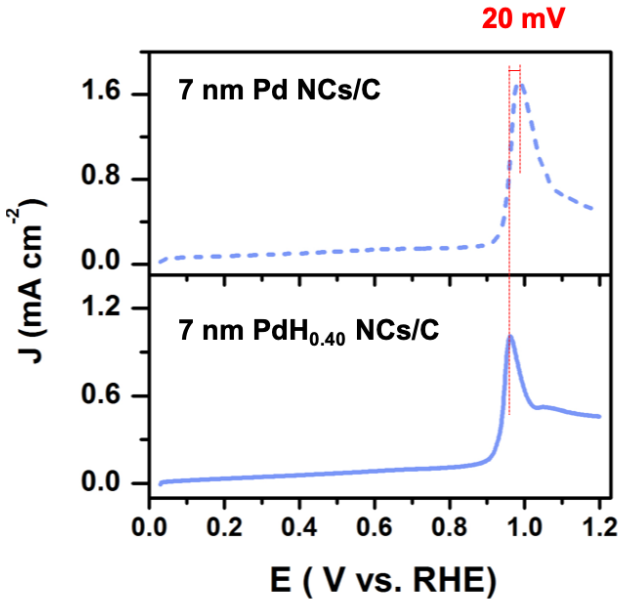

Figure 4.13 CO-stripping curves for 7 nm Pd and $PdH_{0.40}$ NCs/C in 0.1 M KOH solution with a scan rate of 50 mV s^{-1}.

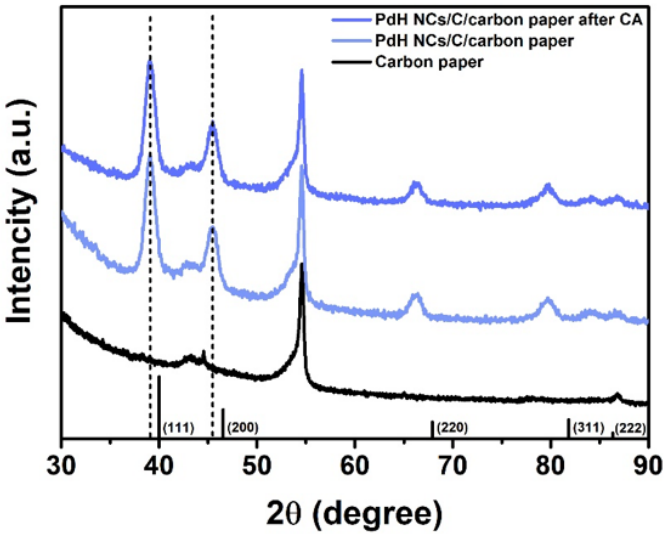

Figure 4.14 XRD patterns of 7 nm Pd and $PdH_{0.40}$ NCs/C/carbon paper before and after 5 min CA experiment at 1.2 V. Black vertical lines representing the Pd reference peaks (JCPDS# 46-1043). Dashed vertical lines representing the peak position of PdH.

It is observed that an optimal catalyst particle size exists in many catalytic reactions [132, 139]. Thus, the size effect of Pd and $PdH_{0.40}$ NCs for CO_2RR was also investigated. By adjusting the amount of KCl and KBr used for the synthesis of Pd NCs, 13 and 19 nm Pd NCs were obtained (**Figure 4.15-4.17**). These Pd NCs were also transformed to $PdH_{0.40}$ NCs under the same condition as that for 7 nm $PdH_{0.40}$ (**Figure 4.15-4.17** and Table 4.5). The beneficial role of the prehydridization process of the Pd NC catalysts in CO_2RR was still valid regardless of the particle size. When the particle size increased to 13 and 19 nm, all $PdH_{0.40}$ catalyst exhibited enhanced CO/H_2 ratios and J_{CO} compared with the corresponding Pd NCs of similar sizes (**Figure 4.18-4.19**). The phenomenon of earlier PdH_1 peak formation from $PdH_{0.40}$ shown by LSV curves was also

observed in 13 and 19 nm NCs (**Figure 4.20**). Moreover, 13 and 19 nm $PdH_{0.40}$ NCs also presented improved tolerance against CO poisoning as shown from the negatively shifted CO oxidation peak in the CO stripping experiment (**Figure 4.21**). It was noted that with increased particle size, the CO/H_2 ratios of Pd and $PdH_{0.40}$ NCs/C both decreased (**Figure 4.22**), implying a hindered CO_2RR rate for the large NCs. Due to the different ECSAs of Pd and $PdH_{0.40}$ NCs/C , the $j_{CO\text{-}Pd}$ of all samples was also compared and showed the similar trends for both Pd and $PdH_{0.40}$ NCs: 7 nm > 13 nm > 19 nm (Table 4.6).

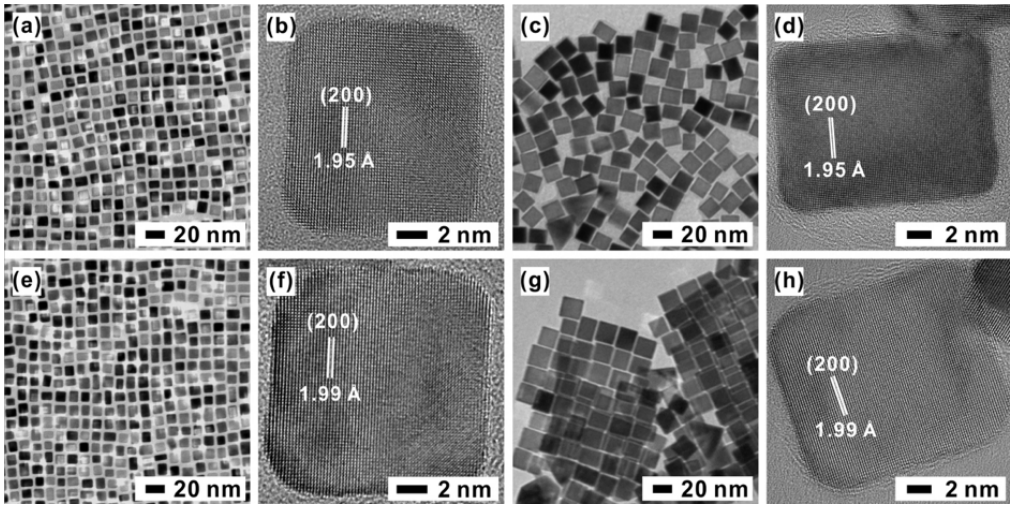

Figure 4.15 Low-resolution TEM and atomic resolution images of (A, B) 13 nm Pd NCs, (C, D) 19 nm Pd NCs, (E, F) 13 nm $PdH_{0.40}$ NCs and (G, H) 19 nm $PdH_{0.40}$ NCs.

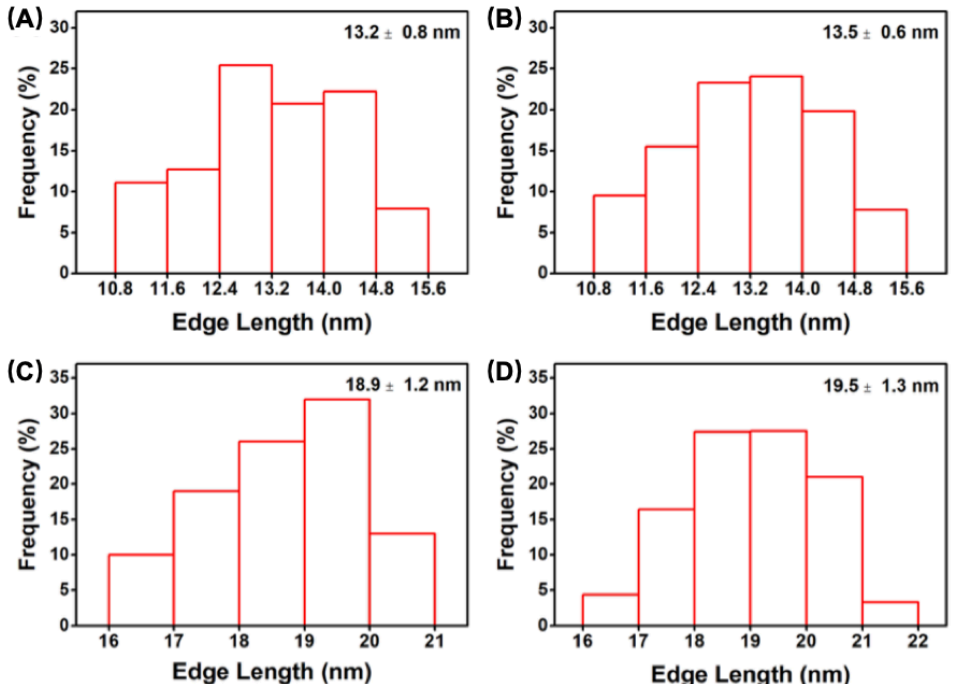

Figure 4.16 Size distributions of 13 nm (A) Pd and (B) $PdH_{0.40}$, 19 nm (C) Pd and (D) $PdH_{0.40}$ NCs.

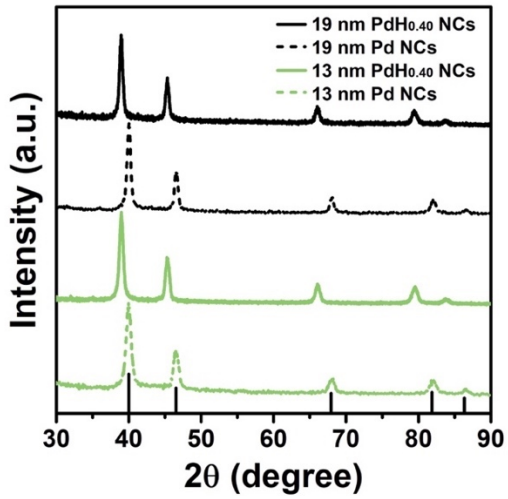

Figure 4.17 XRD patterns of Pd and $PdH_{0.40}$ NCs with the size of 13 and 19 nm. Black vertical lines representing the Pd reference peaks (JCPDS# 46-1043).

Table 4.5 Lattice distance of various Pd-based nanocrystals measured from XRD

sample	2θ of [137] peak (°)	Corresponding lattice distance (nm)	Approximate composition
7 nm Pd NCs	40.01	0.3905	H:Pd = 0
7 nm $PdH_{0.40}$ NCs	39.01	0.4000	H:Pd = 0.40
13 nm Pd NCs	40.04	0.3899	H:Pd = 0
13 nm $PdH_{0.40}$ NCs	39.01	0.3999	H:Pd = 0.40
19 nm Pd NCs	40.03	0.4901	H:Pd = 0
19 nm $PdH_{0.40}$ NCs	39.03	0.3998	H:Pd = 0.40
Pd reference	40.01	0.3903	H:Pd = 0

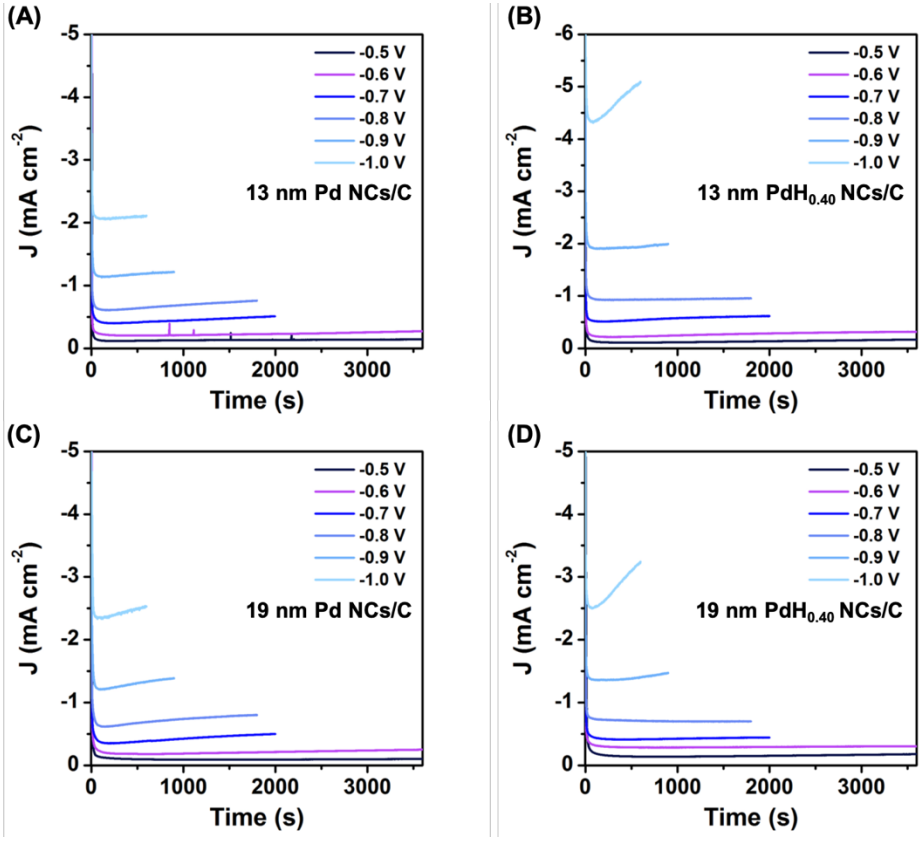

Figure 4.18 The CA curves for different catalysts at given potential. (A) 13 nm Pd NCs/C, (B) 13 nm $PdH_{0.40}$ NCs/C, (C) 19 nm Pd NCs/C, (D) 19 nm $PdH_{0.40}$ NCs/C.

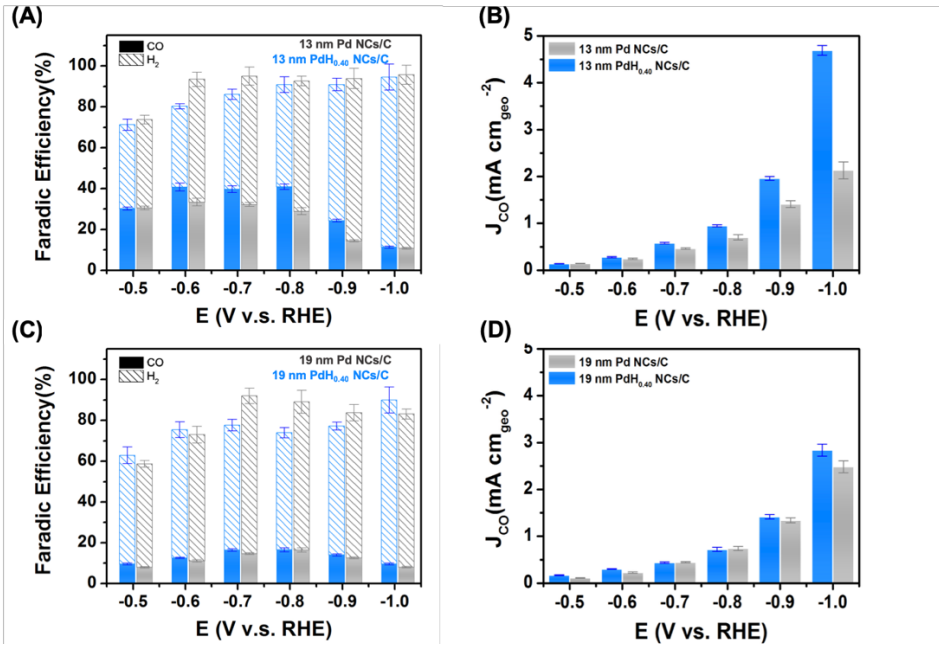

Figure 4.19 (A) Faradaic efficiency of CO and H_2 and (B) partial current density of CO based on geometric area (J_{CO}) of 13 nm Pd and $PdH_{0.40}$ NCs/C. (C) Faradaic efficiency of CO and H_2 and (D) partial current density of CO based on geometric area (J_{CO}) of 19 nm Pd and $PdH_{0.40}$ NCs/C.

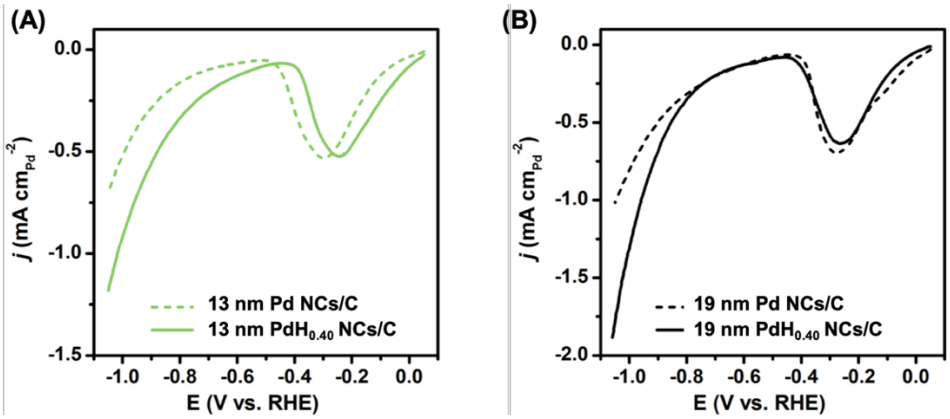

Figure 4.20 Linear sweep voltammetry (LSV) curves of (A) 13 nm and (B) 19 nm Pd and $PdH_{0.40}$ NCs/C.

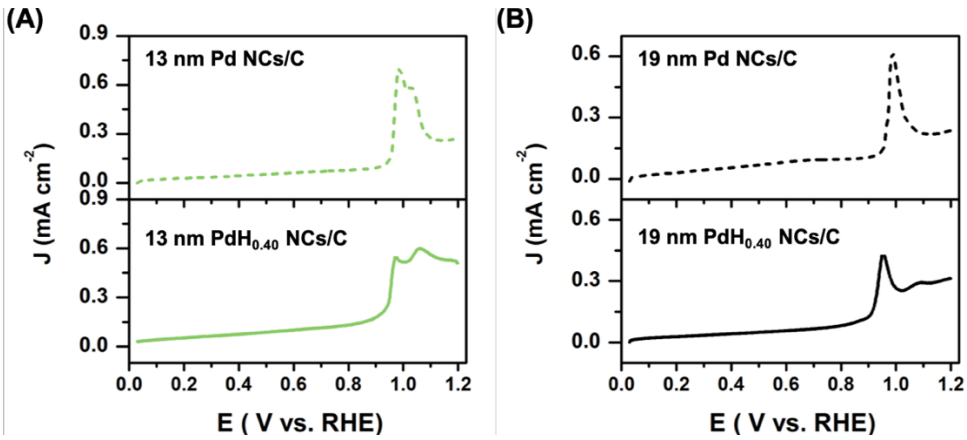

Figure 4.21 CO-stripping curves for different catalysts in 0.1 M KOH solution.

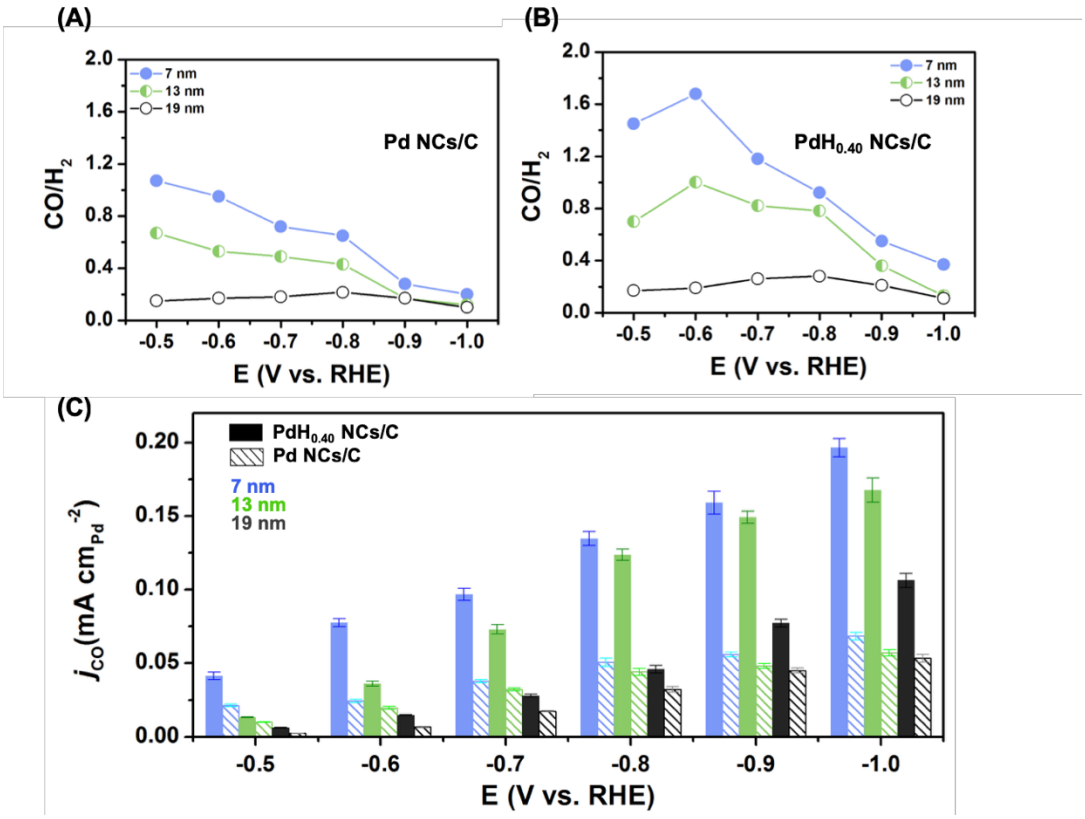

Figure 4.22 Size-dependent CO_2RR performance from -0.5 to 1.0 V. CO/H_2 ratios obtained from (A) Pd NCs (B) $PdH_{0.40}$ NCs. (C) Partial current density of CO based on ECSA ($j_{CO\text{-}Pd}$) of all the prepared electrocatalyts.

Table 4.6 ECSA of various Pd-based nanocrystals measured from Cu UPD.

Sample	ECSA (m^2 g^{-1})
7 nm Pd NCs	56.0
7 nm $PdH_{0.40}$ NCs	48.1
13 nm Pd NCs	29.4
13 nm $PdH_{0.40}$ NCs	27.6
19 nm Pd NCs	18.6
19 nm $PdH_{0.40}$ NCs	16.3

DFT calculations were performed to determine the lattice parameter of PdH_x with various H concentrations (x = 0-100%). In agreement with the experimental measurements, the DFT results (Table 4.7) predicted that the lattice parameter and Pd-Pd bond length increased with increasing H content in the PdH_x bulk structures. Additional DFT calculations were carried out to obtain the binding energies of intermediates of CO_2RR (i. e. *CO and *HOCO) and HER (i. e. *H) on Pd(100), $PdH_{0.5}$(100) and PdH_1(100) surfaces (Table 4.8). A $PdH_{0.5}$(100) surface generated using a bulk $PdH_{0.5}$ structure, computationally much simpler to model compared to the $PdH_{0.4}$ phase, was modeled to represent the surface of $PdH_{0.4}$ nanocubes.

Table 4.7 DFT calculated lattice parameters and Pd-Pd bond lengths of bulk PdH_x.

	Lattice constant (Å)	Pd-Pd bond length (Å)
Pd	3.956959563	2.80
$PdH_{0.25}$	4.014587089	2.84
$PdH_{0.50}$	4.064068025	2.87
$PdH_{0.75}$	4.104873996	2.90
PdH	4.145002821	2.93

Table 4.8 DFT calculated binding energies (in eV) of HER and CO_2RR intermediates.

Species	Pd(100)	$PdH_{0.5}$(100)	PdH(100)
*H	-0.49	-0.17	-0.10
*HOCO	-2.50	-2.03	-2.16
*CO	-1.96	-1.41	-1.29

The DFT calculated binding energies of the intermediates in their most favorable sites (shown in **Figure 4.23A-D** and listed in Table 4.8) revealed a weakened binding on PdH_x(100) compared to Pd(100). Free energy diagrams were constructed using the DFT calculated binding energies in Table 4.8. The calculated free energy diagrams (**Figure 4.23E-F**) showed a thermodynamically favorable formation of the HER and CO_2RR intermediates on Pd(100). However, the CO_2RR activity on Pd(100) should be limited by a large desorption barrier of *CO (i. e. *CO + H_2O(g)→ CO(g) +H_2O(g) + *) due to a strong binding affinity of Pd(100) for the CO intermediate. In contrast, as shown in **Figure 4.23E-F**, the weakened binding of absorbates resulted in the formation of the *H intermediate for HER and *HOCO for CO_2RR being uphill on $PdH_{0.5}$(100) and PdH(100). It was noticed that relatively small applied external potential should be sufficient to make the formation of *H and *HOCO downhill in energy. Furthermore, the weaker binding of *CO made the overall CO_2RR favorable on PdH_x(100) surfaces. Thus, in line with the experimental findings, DFT results indicated that the formation of PdH_x should enhance the CO_2RR compared to Pd.

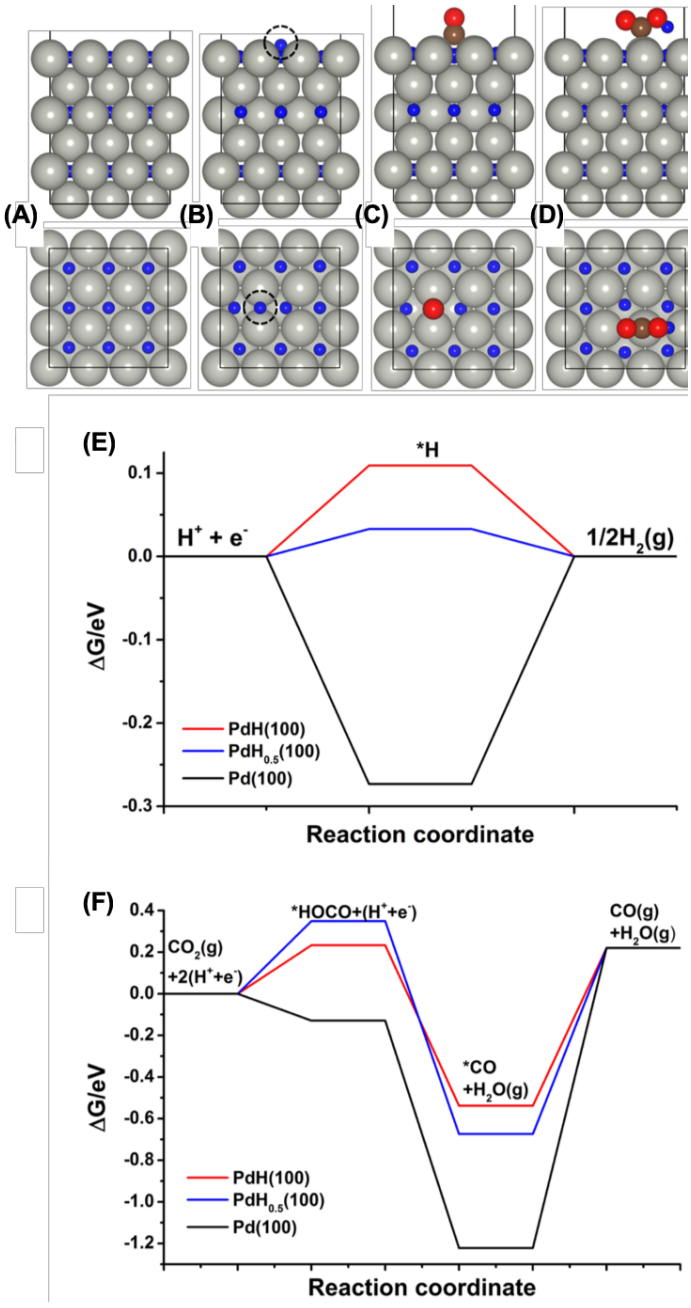

Figure 4.23 DFT optimized structures of (A) $PdH_{0.5}$(100) surface, (B) *H, (C) *CO, and (D) *HOCO adsorbed at the most favorable site on $PdH_{0.5}$(100). Black solid lines show the unit cell used in the DFT calculations and the dotted circle shows the adsorbed *H atom on $PdH_{0.5}$(100). Pd: gray, H: blue, O: red, and C: brown. DFT calculated free energy diagrams of (E) HER, and (F) CO_2RR on Pd(100), PdH(100) and $PdH_{0.5}$(100) surfaces at a potential (U) = 0 V.

4.2.3. Conclusions

In summary, combined results from electrochemical measurements, *in situ* XAFS charcterization and DFT calculations show the benefit of prehydride $PdH_{0.40}$ NC over the Pd counterpart for the syngas production from the CO_2RR. Under the CO_2RR conditions, both of the $PdH_{0.40}$ and Pd NCs would be transformed into the stoichiometric PdH_1. Nevertheless, compared with Pd NCs/C, $PdH_{0.40}$ NCs/C presented less cathodic phase transformation (to PdH_1) by 300 mV, leading to an enhanced CO_2RR performance of $PdH_{0.40}$ NCs/C. The CO/H_2 ratios and CO_2RR activity of 7 nm $PdH_{0.40}$ NCs/C were significantly improved compared with that of Pd NCs/C with the similar size at the low overpotential (i.e. -0.6 V), respectively. Also, $PdH_{0.40}$ NCs/C showed extended suitable potential range for syngas production (CO/H_2 ratios between 1 and 2) in comparison with Pd NCs/C. We also discovered that the size effect also played a key role in determining the CO_2RR performance, with smaller NC size showing higher activity. These results suggest strategies to design more active and selective electrocatalysts for CO_2RR with tunable product compositions.

4.2.4. Acknowledgements

Chapter 4.2, in full, is a reprint of the material “Boosting Activity and Selectivity of CO_2 Electroreduction by Pre-hydridizing Pd Nanocubes” as it appears in Small,

Qiaowan Chang, Jeonghyeon Kim, Ji Hoon Lee, Shyam Kattel, Jingguang G. Chen, Sang-Il Choi, Zheng Chen, 2020, 16, 2005305. The dissertation author was the first author of this paper and conducted all the essential research work.

Chapter 5. Summary and Outlook

The central thrust of this thesis is to explore advanced electrocatalysts for crucial electrochemical reactions, getting one step closer to the industrial applications related to the sustainable and green chemical engineering to solve energy crisis.

The EOR is an important reaction to transit the current fossil fuel to renewable energy for industrial upgrading from the source. We report significant enhancement of EOR activity and CO_2 selectivity by combining alloying and surface structural engineering on Pt-based electrocatalysts. First, the facet-controlled ((100) predominant) PtIr alloy core-shell NCs consisting of a Pt-rich core and an atom-thick Ir-rich shell are prepared. Besides its 4.5-times higher current density than that of Pt/C, it maintains the high CO_2 selectivity during the EOR due to the formation of Ir-rich shell. To further enhance the CO_2 selectivity, the single atomic oxidized Rh are dispersed on the Pt(100) surface of Pt NCs ($Rh_{at}O$-Pt NCs), which is capable to oxidize ethanol to CO_2 with 100% of CO_2 selectivity in a wide low potential region (0.35 – 0.75 V). Above studies suggested that PtM(100) (M=Ir, Rh) surface not only favors the splitting of the C-C bond by providing adsorbed binding sites of $*C_xH_yO/C_xH_y$ species, but also potentially makes the desorption of CO easier if CO is occupying the nearby Pt site, leading to an overall enhanced EOR performance.

H_2O_2 electrochemical synthesis through 2e- ORR is an example of energy saving and emission reduction process for chemical production. We report that direct metal-

oxygen coordination can create unique active sites that enable efficient and a more practical electrocatalyst for the $2e^-$ ORR in acidic electrolytes. Specifically, a class of catalysts containing Pd-O-C type coordination can be synthesized by depositing $Pd^{\delta+}$ clusters (3~4 atoms average) onto mildly oxidized CNTs ($Pd^{\delta+}$-OCNT), which enhance its H_2O_2 production rate. This work points the synergy between partially oxidized metal clusters and oxidized carbon substrate is the key for the electrocatalysts design.

Electrochemical CO_2RR could reutilize and convert CO_2 to syngas, achieving the end treatment of CO_2. We report a method to artificially control the intermediate state of catalyst to promote CO_2 reduction via a prehyridization process, using $PdH_{0.40}$ nanocubes supported on carbon black. The prehydridization process not only makes $PdH_{0.40}$ NCs/C readily for the *in-situ* hydride phase transformation during CO_2RR but also optimizes the hydride formation potentials. This work highlights the importance of catalyst *in-situ* transformation for the electrochemical performance.

Future work will be focused on understanding the relationship between the electrocatalyst essence and its electrochemical performance in terms of activity and selectivity. Most of previous studies demonstrates the d band center would play a key role in determining the binding energy of intermediate, thus affecting electrochemical performance. More detailed descriptors in influencing the d band center should be investigated to provide a clear guideline for the electrocatalyst screen and design.

References

1. Chu, S.; Majumdar, A., Opportunities and challenges for a sustainable energy future. *Nature* **2012,** *488* (7411), 294-303.

2. United Nations Department of Economic and Social Affairs, 2019 Revision of World Population Prospects. https://population.un.org/wpp/ **2019**.

3. International Energy Agency, World Energy Outlook 2020. https://www.iea.org/reports/world-energy-outlook-2020 **2019**.

4. Maljusch, A.; Ventosa, E.; Rincón, R. A.; Bandarenka, A. S.; Schuhmann, W., Revealing onset potentials using electrochemical microscopy to assess the catalytic activity of gas-evolving electrodes. *Electrochem. Commun.* **2014,** *38*, 142-145.

5. Voiry, D.; Chhowalla, M.; Gogotsi, Y.; Kotov, N. A.; Li, Y.; Penner, R. M.; Schaak, R. E.; Weiss, P. S., Best practices for reporting electrocatalytic performance of nanomaterials. ACS Publications: 2018.

6. Shao, M.; Chang, Q.; Dodelet, J.-P.; Chenitz, R., Recent advances in electrocatalysts for oxygen reduction reaction. *Chem. Rev.* **2016,** *116* (6), 3594-3657.

7. Chang, Q.; Kattel, S.; Li, X.; Liang, Z.; Tackett, B. M.; Denny, S. R.; Zhang, P.; Su, D.; Chen, J. G.; Chen, Z., Enhancing C–C Bond Scission for Efficient Ethanol Oxidation using PtIr Nanocube Electrocatalysts. *ACS Catalysis* **2019,** *9* (9), 7618-7625.

8. Verdaguer-Casadevall, A.; Deiana, D.; Karamad, M.; Siahrostami, S.; Malacrida, P.; Hansen, T. W.; Rossmeisl, J.; Chorkendorff, I.; Stephens, I. E., Trends in the electrochemical synthesis of H2O2: enhancing activity and selectivity by electrocatalytic site engineering. *Nano Lett.* **2014,** *14* (3), 1603-1608.

9. Badwal, S.; Giddey, S.; Kulkarni, A.; Goel, J.; Basu, S., Direct ethanol fuel cells for transport and stationary applications–A comprehensive review. *Appl. Energy* **2015,** *145*, 80-103.

10. Giddey, S.; Badwal, S.; Kulkarni, A.; Munnings, C., A comprehensive review of direct carbon fuel cell technology. *Progr. Energy Combust. Sci.* **2012,** *38* (3), 360-399.

11. Lamy, C.; Lima, A.; LeRhun, V.; Delime, F.; Coutanceau, C.; Léger, J.-M., Recent advances in the development of direct alcohol fuel cells (DAFC). *J. Power Sources* **2002,** *105* (2), 283-296.

12. Lai, S. C.; Kleijn, S. E.; Öztürk, F. T.; van Rees Vellinga, V. C.; Koning, J.; Rodriguez, P.; Koper, M. T., Effects of electrolyte pH and composition on the ethanol electro-oxidation reaction. *Catal. Today* **2010,** *154* (1-2), 92-104.

13. Sulaiman, J. E.; Zhu, S.; Xing, Z.; Chang, Q.; Shao, M., Pt–Ni octahedra as electrocatalysts for the ethanol electro-oxidation reaction. *ACS Catalysis* **2017,** *7* (8), 5134-5141.

14. Tian, N.; Zhou, Z.-Y.; Sun, S.-G.; Ding, Y.; Wang, Z. L., Synthesis of tetrahexahedral platinum nanocrystals with high-index facets and high electro-oxidation activity. *Science* **2007,** *316* (5825), 732-735.

15. Wang, Y.; Zou, S.; Cai, W.-B., Recent advances on electro-oxidation of ethanol on Pt-and Pd-based catalysts: From reaction mechanisms to catalytic materials. *Catalysts* **2015,** *5* (3), 1507-1534.

16. Zhou, K.; Li, Y., Catalysis based on nanocrystals with well‐defined facets. *Angewandte Chemie International Edition* **2012,** *51* (3), 602-613.

17. Hitmi, H.; Belgsir, E.; Léger, J.-M.; Lamy, C.; Lezna, R., A kinetic analysis of the electro-oxidation of ethanol at a platinum electrode in acid medium. *Electrochim. Acta* **1994,** *39* (3), 407-415.

18. Iwasita, T.; Pastor, E., A DEMS and FTIR spectroscopic investigation of adsorbed ethanol on polycrystalline platinum. *Electrochim. Acta* **1994,** *39* (4), 531-537.

19. Rizo, R.; Arán-Ais, R. M.; Padgett, E.; Muller, D. A.; Lázaro, M. J. s.; Solla-Gullón, J.; Feliu, J. M.; Pastor, E.; Abruña, H. D., Pt-Richcore/Sn-Richsubsurface/Ptskin Nanocubes As Highly Active and Stable Electrocatalysts for the Ethanol Oxidation Reaction. *J. Am. Chem. Soc.* **2018,** *140* (10), 3791-3797.

20. Dai, S.; Huang, T.-H.; Yan, X.; Yang, C.-Y.; Chen, T.-Y.; Wang, J.-H.; Pan, X.; Wang, K.-W., Promotion of Ternary Pt–Sn–Ag Catalysts toward Ethanol Oxidation Reaction: Revealing Electronic and Structural Effects of Additive Metals. *ACS Energy Letters* **2018,** *3* (10), 2550-2557.

21. Chen, X.; Cai, Z.; Chen, X.; Oyama, M., Green synthesis of graphene–PtPd alloy nanoparticles with high electrocatalytic performance for ethanol oxidation. *Journal of Materials Chemistry A* **2014,** *2* (2), 315-320.

22. Liu, Y.; Wei, M.; Raciti, D.; Wang, Y.; Hu, P.; Park, J. H.; Barclay, M.; Wang, C., Electro-Oxidation of Ethanol Using Pt3Sn Alloy Nanoparticles. *ACS Catalysis* **2018,** *8* (11), 10931-10937.

23. Wang, Q.; Sun, G.; Jiang, L.; Xin, Q.; Sun, S.; Jiang, Y.; Chen, S.; Jusys, Z.; Behm, R., Adsorption and oxidation of ethanol on colloid-based Pt/C, PtRu/C and Pt 3 Sn/C catalysts: In situ FTIR spectroscopy and on-line DEMS studies. *Phys. Chem. Chem. Phys.* **2007,** *9* (21), 2686-2696.

24. Lamy, C.; Rousseau, S.; Belgsir, E.; Coutanceau, C.; Léger, J.-M., Recent progress in the direct ethanol fuel cell: development of new platinum–tin electrocatalysts. *Electrochim. Acta* **2004,** *49* (22-23), 3901-3908.

25. Kavanagh, R.; Cao, X. M.; Lin, W. F.; Hardacre, C.; Hu, P., Origin of low CO2 selectivity on platinum in the direct ethanol fuel cell. *Angewandte Chemie International Edition* **2012,** *51* (7), 1572-1575.

26. Dewan, S.; Raciti, D.; Liu, Y.; Gracias, D. H.; Wang, C., Comparative Studies of Ethanol and Ethylene Glycol Oxidation on Platinum Electrocatalysts. *Top. Catal.* **2018**, 1-8.

27. Song, S.; Zhou, W.; Zhou, Z.; Jiang, L.; Sun, G.; Xin, Q.; Leontidis, V.; Kontou, S.; Tsiakaras, P., Direct ethanol PEM fuel cells: the case of platinum based anodes. *Int. J. Hydrogen Energy* **2005,** *30* (9), 995-1001.

28. James, D. D.; Moghaddam, R. B.; Chen, B.; Pickup, P. G., Ruthenium-Tin Oxide/Carbon Supported Platinum Catalysts for Electrochemical Oxidation of Ethanol in Direct Ethanol Fuel Cells. *J. Electrochem. Soc.* **2018,** *165* (3), F215-F219.

29. Wang, H.-F.; Liu, Z.-P., Comprehensive mechanism and structure-sensitivity of ethanol oxidation on platinum: new transition-state searching method for resolving the complex reaction network. *J. Am. Chem. Soc.* **2008,** *130* (33), 10996-11004.

30. Li, M.; Cullen, D. A.; Sasaki, K.; Marinkovic, N. S.; More, K.; Adzic, R. R., Ternary electrocatalysts for oxidizing ethanol to carbon dioxide: making Ir capable of splitting C–C bond. *J. Am. Chem. Soc.* **2012,** *135* (1), 132-141.

31. Liu, H.; Li, J.; Wang, L.; Tang, Y.; Xia, B. Y.; Chen, Y., Trimetallic PtRhNi alloy nanoassemblies as highly active electrocatalyst for ethanol electrooxidation. *Nano Research* **2017,** *10* (10), 3324-3332.

32. Erini, N.; Beermann, V.; Gocyla, M.; Gliech, M.; Heggen, M.; Dunin‐Borkowski, R. E.; Strasser, P., The Effect of Surface Site Ensembles on the Activity and Selectivity of Ethanol Electrooxidation by Octahedral PtNiRh Nanoparticles. *Angew. Chem.* **2017,** *129* (23), 6633-6638.

33. Han, S. H.; Liu, H. M.; Chen, P.; Jiang, J. X.; Chen, Y., Porous trimetallic PtRhCu cubic nanoboxes for ethanol electrooxidation. *Advanced Energy Materials* **2018,** *8* (24), 1801326.

34. Qu, Y.; Wang, L.; Li, C.; Gao, Y.; Sik, J. K.; Rao, J.; Yin, G., Quantitative pinhole on-line electrochemical mass spectrometry study on ethanol electro-oxidation at carbon-supported Pt and Ir-containing catalysts. *Int. J. Hydrogen Energy* **2017,** *42* (1), 228-235.

35. Freitas, R. G.; Pereira, E. C.; Christensen, P. A., The selective oxidation of ethanol to CO2 at Ptpc/Ir/Pt metallic multilayer nanostructured electrodes. *Electrochem. Commun.* **2011,** *13* (10), 1147-1150.

36. Kowal, A.; Li, M.; Shao, M.; Sasaki, K.; Vukmirovic, M.; Zhang, J. h.; Marinkovic, N.; Liu, P.; Frenkel, A.; Adzic, R., Ternary Pt/Rh/SnO 2 electrocatalysts for oxidizing ethanol to CO 2. *Nat. Mater.* **2009,** *8* (4), 325.

37. De Souza, J.; Queiroz, S.; Bergamaski, K.; Gonzalez, E.; Nart, F., Electro-oxidation of ethanol on Pt, Rh, and PtRh electrodes. A study using DEMS and in-situ FTIR techniques. *The Journal of Physical Chemistry B* **2002,** *106* (38), 9825-9830.

38. https://apps.catalysts.basf.com/apps/eibprices/mp/.

39. Delpeuch, A. B.; Maillard, F.; Chatenet, M.; Soudant, P.; Cremers, C., Ethanol oxidation reaction (EOR) investigation on Pt/C, Rh/C, and Pt-based bi-and tri-metallic electrocatalysts: a DEMS and in situ FTIR study. *Applied Catalysis B: Environmental* **2016,** *181*, 672-680.

40. Zhu, W.; Ke, J.; Wang, S.-B.; Ren, J.; Wang, H.-H.; Zhou, Z.-Y.; Si, R.; Zhang, Y.-W.; Yan, C.-H., Shaping single-crystalline trimetallic Pt–Pd–Rh nanocrystals toward high-efficiency C–C splitting of ethanol in conversion to CO2. *ACS Catalysis* **2015,** *5* (3), 1995-2008.

41. Yang, G.; Frenkel, A. I.; Su, D.; Teng, X., Enhanced electrokinetics of C− C bond splitting during ethanol oxidation by using a Pt/Rh/Sn catalyst with a partially oxidized Pt and Rh core and a SnO2 shell. *ChemCatChem* **2016,** *8* (18), 2876-2880.

42. Silva-Junior, L. C.; Maia, G.; Passos, R. R.; de Souza, E. A.; Camara, G. A.; Giz, M. J., Analysis of the selectivity of PtRh/C and PtRhSn/C to the formation of CO2 during ethanol electrooxidation. *Electrochim. Acta* **2013,** *112*, 612-619.

43. Rao, L.; Jiang, Y.-X.; Zhang, B.-W.; Cai, Y.-R.; Sun, S.-G., High activity of cubic PtRh alloys supported on graphene towards ethanol electrooxidation. *Phys. Chem. Chem. Phys.* **2014,** *16* (27), 13662-13671.

44. Higuchi, E.; Takase, T.; Chiku, M.; Inoue, H., Preparation of ternary Pt/Rh/SnO2 anode catalysts for use in direct ethanol fuel cells and their electrocatalytic activity for ethanol oxidation reaction. *J. Power Sources* **2014,** *263*, 280-287.

45. Craig, J., Practical surface analysis, volume 1—auger and x-ray photoelectron spectroscopy: D. Briggs and MP Seah (editors), Wiley, Chichester, 1990. Pages xiv+ 657.£ 85.00. Elsevier: 1991.

46. Jiang, Z.; Zhang, Q.; Liang, Z.; Chen, J. G., Pt-modified TaC as an efficient electrocatalyst for ethanol oxidation in acid and alkaline electrolytes. *Applied Catalysis B: Environmental* **2018,** *234*, 329-336.

47. Socrates, G., *Infrared and Raman characteristic group frequencies: tables and charts*. John Wiley & Sons: 2004.

48. Kinomoto, Y.; Watanabe, S.; Takahashi, M.; Ito, M., Infrared spectra of CO adsorbed on Pt (100), Pt (111), and Pt (110) electrode surfaces. *Surf. Sci.* **1991,** *242* (1-3), 538-543.

49. Corrigan, D. S.; Krauskopf, E. K.; Rice, L. M.; Wieckowski, A.; Weaver, M. J., Adsorption of acetic acid at platinum and gold electrodes: a combined infrared spectroscopic and radiotracer study. *The Journal of Physical Chemistry* **1988,** *92* (6), 1596-1601.

50. Morris, J. C., Infra‐Red and Raman Spectra of Polyatomic Molecules XIX. Acetaldehyde and Acetaldehyde‐d 4. *The Journal of Chemical Physics* **1943,** *11* (5), 230-235.

51. Hohenberg, P., P. Hohenberg and W. Kohn, Phys. Rev. 136, B864 (1964). *Phys. Rev.* **1964,** *136*, B864.

52. Kresse, G.; Furthmüller, J., Efficient iterative schemes for ab initio total-energy calculations using a plane-wave basis set. *Physical review B* **1996,** *54* (16), 11169.

53. Perdew, J. P.; Wang, Y., Accurate and simple analytic representation of the electron-gas correlation energy. *Physical review B* **1992,** *45* (23), 13244.

54. Monkhorst, H. J.; Pack, J. D., Special points for Brillouin-zone integrations. *Physical review B* **1976,** *13* (12), 5188.

55. Heilmann, P.; Heinz, K.; Müller, K., The superstructures of the clean Pt (100) and Ir (100) surfaces. *Surf. Sci.* **1979,** *83* (2), 487-497.

56. Kotz, J. C.; Treichel, P. M.; Townsend, J., *Chemistry and chemical reactivity*. Cengage Learning: 2012.

57. Robson, J., Modelling the overlap of nucleation, growth and coarsening during precipitation. *Acta Mater.* **2004,** *52* (15), 4669-4676.

58. Liu, X., Heterogeneous nucleation or homogeneous nucleation? *The Journal of Chemical Physics* **2000,** *112* (22), 9949-9955.

59. Markovic, N.; Gasteiger, H.; Ross, P. N., Kinetics of oxygen reduction on Pt (hkl) electrodes: implications for the crystallite size effect with supported Pt electrocatalysts. *J. Electrochem. Soc.* **1997,** *144* (5), 1591-1597.

60. Sheng, W.; Zhuang, Z.; Gao, M.; Zheng, J.; Chen, J. G.; Yan, Y., Correlating hydrogen oxidation and evolution activity on platinum at different pH with measured hydrogen binding energy. *Nat. Commun.* **2015,** *6*, 5848.

61. Neergat, M.; Gunasekar, V.; Singh, R., Oxygen Reduction Reaction and Peroxide Generation on Ir, Rh, and their Selenides–A Comparison with Pt and RuSe. *J. Electrochem. Soc.* **2011,** *158* (9), B1060-B1066.

62. Durst, J.; Siebel, A.; Simon, C.; Hasche, F.; Herranz, J.; Gasteiger, H., New insights into the electrochemical hydrogen oxidation and evolution reaction mechanism. *Energy & Environmental Science* **2014,** *7* (7), 2255-2260.

63. Leung, L.-W. H.; Chang, S.-C.; Weaver, M. J., Real-time FTIR spectroscopy as an electrochemical mechanistic probe: electrooxidation of ethanol and related species on well-defined Pt (111) surfaces. *Journal of electroanalytical chemistry and interfacial electrochemistry* **1989,** *266* (2), 317-336.

64. Colmati, F.; Tremiliosi-Filho, G.; Gonzalez, E. R.; Berná, A.; Herrero, E.; Feliu, J. M., Surface structure effects on the electrochemical oxidation of ethanol on platinum single crystal electrodes. *Faraday Discuss.* **2009,** *140*, 379-397.

65. Hammer, B.; Nørskov, J. K., Theoretical surface science and catalysis—calculations and concepts. In *Adv. Catal.*, Elsevier: 2000; Vol. 45, pp 71-129.

66. Herron, J. A.; Scaranto, J.; Ferrin, P.; Li, S.; Mavrikakis, M., Trends in formic acid decomposition on model transition metal surfaces: A density functional theory study. *Acs Catalysis* **2014,** *4* (12), 4434-4445.

67. Kitchin, J. R.; Nørskov, J. K.; Barteau, M. A.; Chen, J., Role of strain and ligand effects in the modification of the electronic and chemical properties of bimetallic surfaces. *Phys. Rev. Lett.* **2004,** *93* (15), 156801.

68. Luo, M.; Guo, S., Strain-controlled electrocatalysis on multimetallic nanomaterials. *Nature Reviews Materials* **2017,** *2* (11), 17059.

69. Heider, E.; Jacob, T.; Kibler, L., Platinum overlayers on PtxRu1− x (111) electrodes: Tailoring the ORR activity by lateral strain and ligand effects. *J. Electroanal. Chem.* **2018,** *819*, 289-295.

70. Bligaard, T.; Nørskov, J. K.; Dahl, S.; Matthiesen, J.; Christensen, C. H.; Sehested, J., The Brønsted–Evans–Polanyi relation and the volcano curve in heterogeneous catalysis. *J. Catal.* **2004,** *224* (1), 206-217.

71. Ravel, B.; Newville, M., ATHENA, ARTEMIS, HEPHAESTUS: data analysis for X-ray absorption spectroscopy using IFEFFIT. *Journal of synchrotron radiation* **2005,** *12* (4), 537-541.

72. Rehr, J. J.; Albers, R. C., Theoretical approaches to x-ray absorption fine structure. *Reviews of modern physics* **2000,** *72* (3), 621.

73. Hohenberg, P.; Kohn, W., Density functional theory (DFT). *Phys. Rev* **1964,** *136*, B864.

74. Kohn, W.; Sham, L., Self-Consistent Equations Including Exchange and Correlation Effects Phys. Rev. 140, 1133. *EKLER EK A* **1965,** *1*.

75. Perdew, J. P.; Burke, K.; Ernzerhof, M., Perdew, burke, and ernzerhof reply. *Phys. Rev. Lett.* **1998,** *80* (4), 891.

76. Kresse, G.; Furthmüller, J., Efficiency of ab-initio total energy calculations for metals and semiconductors using a plane-wave basis set. *Computational materials science* **1996,** *6* (1), 15-50.

77. Kresse, G.; Hafner, J., Ab initio molecular dynamics for open-shell transition metals. *Physical Review B* **1993,** *48* (17), 13115.

78. Blöchl, P. E., Projector augmented-wave method. *Physical review B* **1994,** *50* (24), 17953.

79. Perdew, J. P.; Wang, Y., Pair-distribution function and its coupling-constant average for the spin-polarized electron gas. *Physical Review B* **1992,** *46* (20), 12947.

80. Chang, Q.; Xu, Y.; Duan, Z.; Xiao, F.; Fu, F.; Hong, Y.; Kim, J.; Choi, S.-I.; Su, D.; Shao, M., Structural Evolution of Sub-10 nm Octahedral Platinum–Nickel Bimetallic Nanocrystals. *Nano Lett.* **2017,** *17* (6), 3926-3931.

81. Xie, S.; Choi, S.-I.; Lu, N.; Roling, L. T.; Herron, J. A.; Zhang, L.; Park, J.; Wang, J.; Kim, M. J.; Xie, Z., Atomic layer-by-layer deposition of Pt on Pd nanocubes for catalysts with enhanced activity and durability toward oxygen reduction. *Nano Lett.* **2014,** *14* (6), 3570-3576.

82. Wade, K., Metal-metal and metal-carbon bond energy terms for the rhodium carbonyl clusters Rh4 (CO) 12 and Rh6 (CO) 16. *Inorganic and Nuclear Chemistry Letters* **1978,** *14* (2-3), 71-74.

83. Hersbach, T. J.; Kortlever, R.; Lehtimäki, M.; Krtil, P.; Koper, M. T., Local structure and composition of PtRh nanoparticles produced through cathodic corrosion. *Phys. Chem. Chem. Phys.* **2017,** *19* (16), 10301-10308.

84. Myers, R. L., *The 100 most important chemical compounds: a reference guide*. ABC-CLIO: 2007.

85. Brillas, E.; Sirés, I.; Oturan, M. A., Electro-Fenton process and related electrochemical technologies based on Fenton's reaction chemistry. *Chem. Rev.* **2009,** *109* (12), 6570-6631.

86. Teles, J.; Hermans, I.; Franz, G.; Sheldon, R., Oxidation. Ullmann's Encyclopedia of Industrial Chemistry. Wiley-VCH, Weinheim: 2015.

87. Fukuzumi, S.; Yamada, Y.; Karlin, K. D., Hydrogen peroxide as a sustainable energy carrier: electrocatalytic production of hydrogen peroxide and the fuel cell. *Electrochim. Acta* **2012,** *82*, 493-511.

88. Yang, S.; Verdaguer-Casadevall, A.; Arnarson, L.; Silvioli, L.; Čolić, V.; Frydendal, R.; Rossmeisl, J.; Chorkendorff, I.; Stephens, I. E., Toward the decentralized

electrochemical production of H2O2: a focus on the catalysis. *ACS Catalysis* **2018,** *8* (5), 4064-4081.

89. Young, M. N.; Links, M. J.; Popat, S. C.; Rittmann, B. E.; Torres, C. I., Tailoring microbial electrochemical cells for production of hydrogen peroxide at high concentrations and efficiencies. *ChemSusChem* **2016,** *9* (23), 3345-3352.

90. Siahrostami, S.; Verdaguer-Casadevall, A.; Karamad, M.; Deiana, D.; Malacrida, P.; Wickman, B.; Escudero-Escribano, M.; Paoli, E. A.; Frydendal, R.; Hansen, T. W., Enabling direct H 2 O 2 production through rational electrocatalyst design. *Nat. Mater.* **2013,** *12* (12), 1137.

91. Jiang, Y.; Ni, P.; Chen, C.; Lu, Y.; Yang, P.; Kong, B.; Fisher, A.; Wang, X., Selective Electrochemical H2O2 Production through Two‐Electron Oxygen Electrochemistry. *Advanced Energy Materials* **2018,** *8* (31), 1801909.

92. Jiang, K.; Back, S.; Akey, A. J.; Xia, C.; Hu, Y.; Liang, W.; Schaak, D.; Stavitski, E.; Nørskov, J. K.; Siahrostami, S., Highly selective oxygen reduction to hydrogen peroxide on transition metal single atom coordination. *Nat. Commun.* **2019,** *10* (1), 1-11.

93. Xia, C.; Xia, Y.; Zhu, P.; Fan, L.; Wang, H., Direct electrosynthesis of pure aqueous H2O2 solutions up to 20% by weight using a solid electrolyte. *Science* **2019,** *366* (6462), 226-231.

94. Lu, Z.; Chen, G.; Siahrostami, S.; Chen, Z.; Liu, K.; Xie, J.; Liao, L.; Wu, T.; Lin, D.; Liu, Y., High-efficiency oxygen reduction to hydrogen peroxide catalysed by oxidized carbon materials. *Nature Catalysis* **2018,** *1* (2), 156.

95. Chen, S.; Chen, Z.; Siahrostami, S.; Higgins, D.; Nordlund, D.; Sokaras, D.; Kim, T. R.; Liu, Y.; Yan, X.; Nilsson, E., Designing boron nitride islands in carbon materials for efficient electrochemical synthesis of hydrogen peroxide. *J. Am. Chem. Soc.* **2018,** *140* (25), 7851-7859.

96. Kim, H. W.; Ross, M. B.; Kornienko, N.; Zhang, L.; Guo, J.; Yang, P.; McCloskey, B. D., Efficient hydrogen peroxide generation using reduced graphene oxide-based oxygen reduction electrocatalysts. *Nature Catalysis* **2018,** *1* (4), 282.

97. Varcoe, J. R.; Atanassov, P.; Dekel, D. R.; Herring, A. M.; Hickner, M. A.; Kohl, P. A.; Kucernak, A. R.; Mustain, W. E.; Nijmeijer, K.; Scott, K., Anion-exchange membranes in electrochemical energy systems. *Energy & environmental science* **2014,** *7* (10), 3135-3191.

98. https://www.gminsights.com/industry-analysis/hydrogen-peroxide-market.

99. Gibian, M. J.; Elliott, D. L.; Hardy, W. R., Reaction of a sulfonyl-chymotrypsin with hydrogen peroxide. Generation of a hydroperoxy enzyme. *J. Am. Chem. Soc.* **1969,** *91* (26), 7528-7530.

100. Fellinger, T.-P.; Hasché, F. d. r.; Strasser, P.; Antonietti, M., Mesoporous nitrogen-doped carbon for the electrocatalytic synthesis of hydrogen peroxide. *J. Am. Chem. Soc.* **2012,** *134* (9), 4072-4075.

101. Park, J.; Nabae, Y.; Hayakawa, T.; Kakimoto, M.-a., Highly selective two-electron oxygen reduction catalyzed by mesoporous nitrogen-doped carbon. *ACS Catalysis* **2014,** *4* (10), 3749-3754.

102. Jirkovský, J. S.; Halasa, M.; Schiffrin, D. J., Kinetics of electrocatalytic reduction of oxygen and hydrogen peroxide on dispersed gold nanoparticles. *Phys. Chem. Chem. Phys.* **2010,** *12* (28), 8042-8053.

103. Choi, C. H.; Kwon, H. C.; Yook, S.; Shin, H.; Kim, H.; Choi, M., Hydrogen peroxide synthesis via enhanced two-electron oxygen reduction pathway on carbon-coated Pt surface. *The Journal of Physical Chemistry C* **2014,** *118* (51), 30063-30070.

104. Yang, S.; Kim, J.; Tak, Y. J.; Soon, A.; Lee, H., Single‐atom catalyst of platinum supported on titanium nitride for selective electrochemical reactions. *Angewandte Chemie International Edition* **2016,** *55* (6), 2058-2062.

105. Jirkovský, J. S.; Panas, I.; Ahlberg, E.; Halasa, M.; Romani, S.; Schiffrin, D. J., Single atom hot-spots at Au–Pd nanoalloys for electrocatalytic H2O2 production. *J. Am. Chem. Soc.* **2011,** *133* (48), 19432-19441.

106. Pizzutilo, E.; Kasian, O.; Choi, C. H.; Cherevko, S.; Hutchings, G. J.; Mayrhofer, K. J.; Freakley, S. J., Electrocatalytic synthesis of hydrogen peroxide on Au-Pd nanoparticles: From fundamentals to continuous production. *Chem. Phys. Lett.* **2017,** *683*, 436-442.

107. Choi, C. H.; Lim, H.-K.; Chung, M. W.; Chon, G.; Sahraie, N. R.; Altin, A.; Sougrati, M.-T.; Stievano, L.; Oh, H. S.; Park, E. S., The Achilles' heel of iron-based catalysts during oxygen reduction in an acidic medium. *Energy & Environmental Science* **2018,** *11* (11), 3176-3182.

108. Suk, M.; Chung, M. W.; Han, M. H.; Oh, H.-S.; Choi, C. H., Selective H2O2 production on surface-oxidized metal-nitrogen-carbon electrocatalysts. *Catal. Today* **2019**.

109. Wei, F.; Zhang, Q.; Qian, W.-Z.; Yu, H.; Wang, Y.; Luo, G.-H.; Xu, G.-H.; Wang, D.-Z., The mass production of carbon nanotubes using a nano-agglomerate fluidized bed reactor: A multiscale space–time analysis. *Powder Technol.* **2008,** *183* (1), 10-20.

110. Kelly, S.; Hesterberg, D.; Ravel, B., Analysis of soils and minerals using X-ray absorption spectroscopy. *Methods of soil analysis. Part 5. Mineralogical methods* **2008,** *5*, 387-464.

111. Bahn, S. R.; Jacobsen, K. W., An object-oriented scripting interface to a legacy electronic structure code. *Computing in Science & Engineering* **2002,** *4* (3), 56-66.

112. Giannozzi, P.; Baroni, S.; Bonini, N.; Calandra, M.; Car, R.; Cavazzoni, C.; Ceresoli, D.; Chiarotti, G. L.; Cococcioni, M.; Dabo, I., QUANTUM ESPRESSO: a modular and open-source software project for quantum simulations of materials. *J. Phys.: Condens. Matter* **2009,** *21* (39), 395502.

113. Adllan, A. A.; Dal Corso, A., Ultrasoft pseudopotentials and projector augmented-wave data sets: application to diatomic molecules. *J. Phys.: Condens. Matter* **2011,** *23* (42), 425501.

114. Grimme, S.; Antony, J.; Ehrlich, S.; Krieg, H., A consistent and accurate ab initio parametrization of density functional dispersion correction (DFT-D) for the 94 elements H-Pu. *The Journal of chemical physics* **2010,** *132* (15), 154104.

115. Osswald, S.; Havel, M.; Gogotsi, Y., Monitoring oxidation of multiwalled carbon nanotubes by Raman spectroscopy. *Journal of Raman Spectroscopy: An International Journal for Original Work in all Aspects of Raman Spectroscopy, Including Higher Order Processes, and also Brillouin and Rayleigh Scattering* **2007,** *38* (6), 728-736.

116. Frank, B.; Rinaldi, A.; Blume, R.; Schlögl, R.; Su, D. S., Oxidation stability of multiwalled carbon nanotubes for catalytic applications. *Chem. Mater.* **2010,** *22* (15), 4462-4470.

117. Vijayarangamuthu, K.; Ahn, S.; Seo, H.; Yoon, S. H.; Park, C. M.; Jeon, K. J., Graphene: Temporospatial Control of Graphene Wettability (Adv. Mater. 4/2016). *Adv. Mater.* **2016,** *28* (4), 594-594.

118. Kim, Y.-T.; Ito, Y.; Tadai, K.; Mitani, T.; Kim, U.-S.; Kim, H.-S.; Cho, B.-W., Drastic change of electric double layer capacitance by surface functionalization of carbon nanotubes. *Appl. Phys. Lett.* **2005,** *87* (23), 234106.

119.Jiang, H.; Gu, J.; Zheng, X.; Liu, M.; Qiu, X.; Wang, L.; Li, W.; Chen, Z.; Ji, X.; Li, J., Defect-rich and ultrathin N doped carbon nanosheets as advanced trifunctional metal-free electrocatalysts for the ORR, OER and HER. *Energy & Environmental Science* **2019,** *12* (1), 322-333.

120. Dresselhaus, M. S.; Jorio, A.; Hofmann, M.; Dresselhaus, G.; Saito, R., Perspectives on carbon nanotubes and graphene Raman spectroscopy. *Nano Lett.* **2010,** *10* (3), 751-758.

121. Zheng, Z.; Ng, Y. H.; Wang, D. W.; Amal, R., Epitaxial growth of Au–Pt–Ni nanorods for direct high selectivity H2O2 production. *Adv. Mater.* **2016,** *28* (45), 9949-9955.

122. Lee, Y.-H.; Li, F.; Chang, K.-H.; Hu, C.-C.; Ohsaka, T., Novel synthesis of N-doped porous carbons from collagen for electrocatalytic production of H2O2. *Applied Catalysis B: Environmental* **2012,** *126*, 208-214.

123. Shen, R.; Chen, W.; Peng, Q.; Lu, S.; Zheng, L.; Cao, X.; Wang, Y.; Zhu, W.; Zhang, J.; Zhuang, Z., High-Concentration Single Atomic Pt Sites on Hollow CuSx for Selective O2 Reduction to H2O2 in Acid Solution. *Chem* **2019**.

124. Siahrostami, S.; Li, G.-L.; Nørskov, J. K.; Studt, F., Trends in Adsorption Energies of the Oxygenated Species on Single Platinum Atom Embedded in Carbon Nanotubes. *Catal. Lett.* **2017,** *147* (11), 2689-2696.

125. Meinshausen, M.; Meinshausen, N.; Hare, W.; Raper, S. C.; Frieler, K.; Knutti, R.; Frame, D. J.; Allen, M. R., Greenhouse-gas emission targets for limiting global warming to 2 C. *Nature* **2009,** *458* (7242), 1158-1162.

126. Long, C.; Li, X.; Guo, J.; Shi, Y.; Liu, S.; Tang, Z., Electrochemical reduction of CO2 over heterogeneous catalysts in aqueous solution: recent progress and perspectives. *Small Methods* **2019,** *3* (3), 1800369.

127. Gattrell, M.; Gupta, N.; Co, A., A review of the aqueous electrochemical reduction of CO2 to hydrocarbons at copper. *J. Electroanal. Chem.* **2006,** *594* (1), 1-19.

128. Hori, Y. i., Electrochemical CO 2 reduction on metal electrodes. In *Modern aspects of electrochemistry*, Springer: 2008; pp 89-189.

129. Tackett, B. M.; Gomez, E.; Chen, J. G., Net reduction of CO 2 via its thermocatalytic and electrocatalytic transformation reactions in standard and hybrid processes. *Nature Catalysis* **2019,** *2* (5), 381-386.

130. Pan, Y.; Lin, R.; Chen, Y.; Liu, S.; Zhu, W.; Cao, X.; Chen, W.; Wu, K.; Cheong, W.-C.; Wang, Y., Design of single-atom Co–N5 catalytic site: a robust electrocatalyst for CO2 reduction with nearly 100% CO selectivity and remarkable stability. *J. Am. Chem. Soc.* **2018,** *140* (12), 4218-4221.

131. Liu, S.; Tao, H.; Zeng, L.; Liu, Q.; Xu, Z.; Liu, Q.; Luo, J.-L., Shape-dependent electrocatalytic reduction of CO2 to CO on triangular silver nanoplates. *J. Am. Chem. Soc.* **2017,** *139* (6), 2160-2163.

132. Zhu, W.; Michalsky, R.; Metin, O. n.; Lv, H.; Guo, S.; Wright, C. J.; Sun, X.; Peterson, A. A.; Sun, S., Monodisperse Au nanoparticles for selective electrocatalytic reduction of CO2 to CO. *J. Am. Chem. Soc.* **2013,** *135* (45), 16833-16836.

133. Sheng, W.; Kattel, S.; Yao, S.; Yan, B.; Liang, Z.; Hawxhurst, C. J.; Wu, Q.; Chen, J. G., Electrochemical reduction of CO 2 to synthesis gas with controlled CO/H 2 ratios. *Energy & Environmental Science* **2017,** *10* (5), 1180-1185.

134. Lu, Q.; Rosen, J.; Zhou, Y.; Hutchings, G. S.; Kimmel, Y. C.; Chen, J. G.; Jiao, F., A selective and efficient electrocatalyst for carbon dioxide reduction. *Nat. Commun.* **2014,** *5* (1), 1-6.

135. Wang, J.; Kattel, S.; Hawxhurst, C. J.; Lee, J. H.; Tackett, B. M.; Chang, K.; Rui, N.; Liu, C. J.; Chen, J. G., Enhancing Activity and Reducing Cost for Electrochemical Reduction of CO2 by Supporting Palladium on Metal Carbides. *Angewandte Chemie International Edition* **2019,** *58* (19), 6271-6275.

136. Wender, I., Reactions of synthesis gas. *Fuel Process. Technol.* **1996,** *48* (3), 189-297.

137. Lee, J. H.; Kattel, S.; Jiang, Z.; Xie, Z.; Yao, S.; Tackett, B. M.; Xu, W.; Marinkovic, N. S.; Chen, J. G., Tuning the activity and selectivity of electroreduction of CO 2 to synthesis gas using bimetallic catalysts. *Nat. Commun.* **2019,** *10* (1), 1-8.

138. Hori, Y.; Wakebe, H.; Tsukamoto, T.; Koga, O., Electrocatalytic process of CO selectivity in electrochemical reduction of CO2 at metal electrodes in aqueous media. *Electrochim. Acta* **1994,** *39* (11-12), 1833-1839.

139. Gao, D.; Zhou, H.; Wang, J.; Miao, S.; Yang, F.; Wang, G.; Wang, J.; Bao, X., Size-dependent electrocatalytic reduction of CO2 over Pd nanoparticles. *J. Am. Chem. Soc.* **2015,** *137* (13), 4288-4291.

140. Zhu, W.; Kattel, S.; Jiao, F.; Chen, J. G., Shape‐controlled CO2 electrochemical reduction on nanosized Pd hydride cubes and octahedra. *Advanced Energy Materials* **2019,** *9* (9), 1802840.

141. Huang, H.; Jia, H.; Liu, Z.; Gao, P.; Zhao, J.; Luo, Z.; Yang, J.; Zeng, J., Understanding of strain effects in the electrochemical reduction of CO2: using Pd nanostructures as an ideal platform. *Angewandte Chemie International Edition* **2017,** *56* (13), 3594-3598.

142. Nørskov, J. K.; Abild-Pedersen, F.; Studt, F.; Bligaard, T., Density functional theory in surface chemistry and catalysis. *Proceedings of the National Academy of Sciences* **2011,** *108* (3), 937-943.

143. Liu, Y.; Tian, D.; Biswas, A. N.; Xie, Z.; Hwang, S.; Lee, J. H.; Meng, H.; Chen, J. G., Transition Metal Nitrides as Novel Catalyst Supports for Tuning CO/H2 Syngas Production from Electrochemical CO2 Reduction. *Angew. Chem.* **2020**.

144. Liu, M.; Zheng, Y.; Zhang, L.; Guo, L.; Xia, Y., Transformation of Pd nanocubes into octahedra with controlled sizes by maneuvering the rates of etching and regrowth. *J. Am. Chem. Soc.* **2013,** *135* (32), 11752-11755.

145. Kabiraz, M. K.; Kim, J.; Lee, W.-J.; Ruqia, B.; Kim, H. C.; Lee, S.-U.; Kim, J.-R.; Paek, S.-M.; Hong, J. W.; Choi, S.-I., Ligand Effect of Shape-Controlled β-Palladium Hydride Nanocrystals on Liquid-Fuel Oxidation Reactions. *Chem. Mater.* **2019,** *31* (15), 5663-5673.

146. Eastman, J.; Thompson, L.; Kestel, B., Narrowing of the palladium-hydrogen miscibility gap in nanocrystalline palladium. *Physical Review B* **1993,** *48* (1), 84.

147. Kelly, S.; Hesterberg, D.; Ravel, B., Analysis of soils and minerals using X‐ray absorption spectroscopy. *Methods of Soil Analysis Part 5—Mineralogical Methods* **2008,** *5*, 387-463.

148. Hohenberg, P.; Kohn, W., Inhomogeneous electron gas. *Physical review* **1964,** *136* (3B), B864.

149. Kohn, W.; Sham, L. J., Self-consistent equations including exchange and correlation effects. *Physical review* **1965,** *140* (4A), A1133.

150. Kresse, G.; Joubert, D., From ultrasoft pseudopotentials to the projector augmented-wave method. *Physical review b* **1999,** *59* (3), 1758.

151. Nørskov, J. K.; Rossmeisl, J.; Logadottir, A.; Lindqvist, L.; Kitchin, J. R.; Bligaard, T.; Jonsson, H., Origin of the overpotential for oxygen reduction at a fuel-cell cathode. *The Journal of Physical Chemistry B* **2004,** *108* (46), 17886-17892.

152. Zhao, Z.; Huang, X.; Li, M.; Wang, G.; Lee, C.; Zhu, E.; Duan, X.; Huang, Y., Synthesis of stable shape-controlled catalytically active β-palladium hydride. *J. Am. Chem. Soc.* **2015,** *137* (50), 15672-15675.

153. Bennett, P.; Fuggle, J., Electronic structure and surface kinetics of palladium hydride studied with x-ray photoelectron spectroscopy and electron-energy-loss spectroscopy. *Physical Review B* **1982,** *26* (11), 6030.

154. Chan, C. T.; Louie, S. G., Self-consistent pseudopotential calculation of the electronic structure of PdH and Pd 4 H. *Physical Review B* **1983,** *27* (6), 3325.